THRUST VECTOR CONTROL BY SECONDARY INJECTION

A THESIS SUBMITTED TO
THE GRADUATE SCHOOL OF NATURAL AND APPLIED SCIENCES
OF
MIDDLE EAST TECHNICAL UNIVERSITY

BY

ERİNÇ ERDEM

IN PARTIAL FULFILLMENT OF THE REQUIREMENTS
FOR
THE DEGREE OF MASTER OF SCIENCE
IN
MECHANICAL ENGINEERING

SEPTEMBER 2006

Approval of the Graduate School of Natural and Applied Sciences

Prof. Dr. Canan ÖZGEN
Director

I certify that this thesis satisfies all the requirements as a thesis for the degree of Master of Science.

Prof. Dr. S. Kemal İDER
Head of Department

This is to certify that we have read this thesis and that in our opinion it is fully adequate in scope and quality, as a thesis for the degree of Master of Science.

Dr. H. Tuğrul TINAZTEPE	Prof. Dr. Kahraman ALBAYRAK
Co-Supervisor	Supervisor

Examining Committee Members:

Prof. Dr. M. Haluk AKSEL (METU, ME)
Assoc. Prof. Dr. Tahsin ÇETİNKAYA (METU, ME)
Prof. Dr. Kahraman ALBAYRAK (METU, ME)
Asst. Prof. Dr. Cüneyt SERT (METU, ME)
Dr. H. Tuğrul TINAZTEPE (ROKETSAN)

I hereby declare that all information in this document has been obtained and presented in accordance with academic rules and ethical conduct. I also declare that, as required by these rules and conduct, I have fully cited and referenced all material and results that are not original to this work.

Name, Last name: Erinç Erdem

Signature :

ABSTRACT

THRUST VECTOR CONTROL BY SECONDARY INJECTION

ERDEM, Erinç

M.Sc., Department of Mechanical Engineering

Supervisor: Prof. Dr. Kahraman ALBAYRAK

Co-Supervisor: Dr. H. Tuğrul TINAZTEPE

September 2006, 103 pages

A parametric study on Secondary Injection Thrust Vector Control (SITVC) has been accomplished numerically with the help of a commercial Computational Fluid Dynamics (CFD) code called FLUENT®. This study consists of two parts; the first part includes the simulation of three dimensional flowfield inside a test case nozzle for the selection of parameters associated with both computational grid and the CFD solver such as mesh size, turbulence model accompanied with two different wall treatment approaches, and solver type. This part revealed that simulation of internal flowfield by a segregated solver with Realizable k-ε (Rke) turbulence model accompanied by enhanced wall treatment approach is accurate enough to resolve this kind of complex three dimensional fluid flow problems. In the second part a typical rocket nozzle with conical diverging section is picked for the parametric study on injection mass flow rate, injection location and injection angle. A test matrix is constructed; several numerical simulations are run to yield the

assessment of performance of SITVC system. The results stated that for a nozzle with a small divergence angle, downstream injections with distances of 2.5-3.5 throat diameters from the nozzle throat lead to higher efficiencies over a certain range of total pressure ratios, i.e., mass flow rate ratios, upstream injections should be aligned more to the nozzle axis, i.e., higher injection angles, to prevent reflection of shock waves from the opposite wall and thus low efficiencies. Injection locations that are too much downstream may result reversed flows on nozzle exit.

Keywords: Rocket nozzles, thrust vector control, commercial CFD packages, FLUENT

ÖZ

İKİNCİL AKIŞ İLE İTKİ VEKTÖR KONTROLÜ

ERDEM, Erinç
Yüksek Lisans, Makine Mühendisliği Bölümü
Tez Yöneticisi: Prof. Dr. Kahraman ALBAYRAK
Ortak Tez Yöneticisi: Dr. H. Tuğrul TINAZTEPE

Eylül 2006, 103 sayfa

İkincil Akış ile İtki Vektör Kontrolü (İAİVK) üzerine parametrik bir çalışma sayısal olarak bir ticari Hesaplamalı Akışkanlar Dinamiği (HAD) çözücüsü olan FLUENT® programıyla gerçekleştirilmiştir. Bu çalışma iki kısımdan oluşmaktadır. İlk kısım bir test lülesi içindeki üç boyutlu akış alanının benzetişimini içermektedir; böylelikle hem ticari çözücü doğrulanmış hem de daha önemli olarak sayısal çözüm ağı ve çözücü ile bağlantılı olan çözüm ağı büyüklüğü, türbülans modelleri (iki farklı duvar yaklaşımıyla beraber) ve çözücü tipi gibi parametreler test edilmiştir. Bu kısmın sonunda, parçalı çözücüyle beraber Realizable k-ε (Rke) türbülans modeli (yoğunlaştırılmış duvar yaklaşımını içererek) yeterince hassas bir şekilde bu tip üç boyutlu karmaşık akış problemlerini çözmek için uygun olduğu değerlendirilmiştir. İkinci kısımda ise konik ıraksama kısmına sahip tipik bir roket lülesinde püskürtme debisi, püskürtme yeri üzerine sabit püskürtme açısıyla parametrik çalışma yapılmıştır. Test matrisi oluşturulmuş ve birçok benzetişim yapılarak İAİVK sisteminin performansı değerlendirilmiştir. Sonuçlar küçük ıraksama açısına sahip lüleler için uzak püskürtmelerin (lüle boğazından 2.5-3.5 lüle çapı uzaklıktaki püskürtme yerleri için) belli bir püskürtme debisi aralığında daha verimli olduğunu, boğaza yakın yerlerden yapılan püskürtmelerin, ise şok dalgalarının karşı duvara çarpıp düşük verimliliğe sebep olmasını engellemek için lüle eksenine doğru daha fazla yöneltilmelerinin gerekliliğini (daha yüksek püskürtme açıları) göstermiştir. Çok gerideki püskürtmeler lüle düzleminde ters akışlara yol açıp verim kaybına yol açabilir.

Anahtar Kelimeler: Roket lüleleri, itki vektör kontrolü, ticari HAD programları, FLUENT.

To Fatma & Hilmi ERDEM

ACKNOWLEDGMENTS

I would like to express my deepest thanks and gratitude to Prof. Dr. Kahraman ALBAYRAK for his supervision, encouragement, understanding and constant guidance.

Also I would like to express my gratitude to Dr. H. Tuğrul TINAZTEPE for initializing and supporting this thesis.

I would like to thank to Mr. Emre ÖZTÜRK for his assistance on using the FLUENT® CFD flow solver.

I would like to express my sincere appreciation to Uğur ARKUN, Başar SEÇKİN and Dr. Atılgan TOKER for their crucial advises during the preparation of this thesis.

My gratitude is endless for my family, without their presence this thesis would not have been possible.

TABLE OF CONTENTS

LIST OF TABLES

LIST OF FIGURES

LIST OF SYMBOLS

a	=	Speed of sound
A	=	Cross sectional area
ATA	=	Axial thrust augmentation
c	=	Cell center notation, constant
C_f	=	Skin friction coefficient
D	=	Diameter
E	=	Total energy
F	=	Force
H	=	Total enthalpy, net flux (convective plus viscous flux)
g	=	Gravitational field
I	=	Identity tensor
Isp	=	Specific impulse
K	=	Specific impulse ratio
k	=	Turbulent kinetic energy
L	=	Length
m	=	Mass flow rate
M	=	Mach number, moment, molecular weight (with w subscript)
n	=	Unit normal vector from the surface
q	=	Heat flux
P	=	Pressure
r	=	Radius
R	=	Gas constant, 287 J/kg.K for air
Re	=	Reynolds number
Rx	=	x component of the resultant force acting on the system
Ry	=	y component of the resultant force acting on the system

s	=	Displacement
S	=	Source term, area
T	=	Time
T	=	Temperature
TI	=	Turbulence intensity
TR	=	Thrust ratio
u,v,w	=	Primary velocity components in Cartesian coordinates
U_τ	=	Friction velocity
V	=	Velocity (with vector sign), volume
x,y,z	=	Primary Cartesian coordinates
y^+	=	Non dimensional distance from the wall

Greek Symbols

α	=	Injection angle with respect to the coordinate system
γ	=	Ratio of the specific heats, 1.4 for air
Γ	=	Diffusion coefficient
δ	=	Partial derivative, Kronecker delta
Δ	=	Differential
ε	=	Turbulence dissipation rate
θ	=	Deflection angle
λ	=	Bulk viscosity coefficient
μ	=	Dynamic viscosity
ν	=	Kinematic viscosity
Φ	=	Conserved quantity, scalar quantity
ρ	=	Density
σ	=	Normal stress
τ	=	Shear stress
υ	=	Turbulent “eddy” viscosity
ω	=	Turbulence specific dissipation rate

Subscripts

b	=	Body
f	=	Face
G	=	Source terms
h	=	Hydraulic
i	=	Cell index, tensor index, injection
inj	=	Injection condition
j	=	Face index, tensor index
p	=	Primary flow
s	=	Secondary jet or side
t	=	Turbulent
x	=	Distance
0	=	Reference state

Superscripts

n	=	Time Step
′	=	Fluctuating component
‾	=	Time averaged component

CHAPTER 1

INTRODUCTION

In addition to providing a propulsive force to a flying vehicle or a rocket, a rocket propulsion system can also provide certain control mechanisms to change vehicle's attitude and trajectory via thrust vector control (TVC) systems. By controlling the direction of the thrust vector pitching, yawing and rolling moments as shown in Fig.1-1 can be achieved on the flying body.

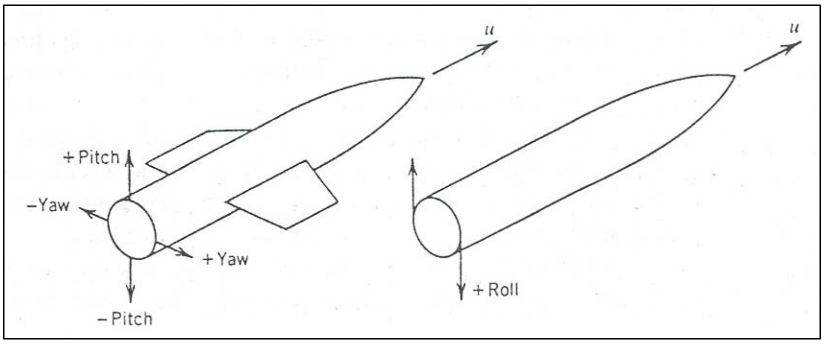

Figure 1-1 Pitching, yawing and rolling moments around the flying body

Pitching moments raise or lower the nose of the body, yawing moments turn the nozzle sideways and rolling moments tend to rotate the vehicle on its main axis. In general the thrust vector passes through center of gravity (c.g.) of the vehicle and the line of action of this vector is main axis of the body, thus pitching and yawing moments can be generated by only deflecting the thrust vector as seen from Fig.1-2, whereas rolling moment basically requires at least two vectors with an offset [1]. The moment compatible with this figure is expressed as follows in Eq. 1-1.

$$M = F \cdot \sin \theta \cdot L \qquad (1)$$

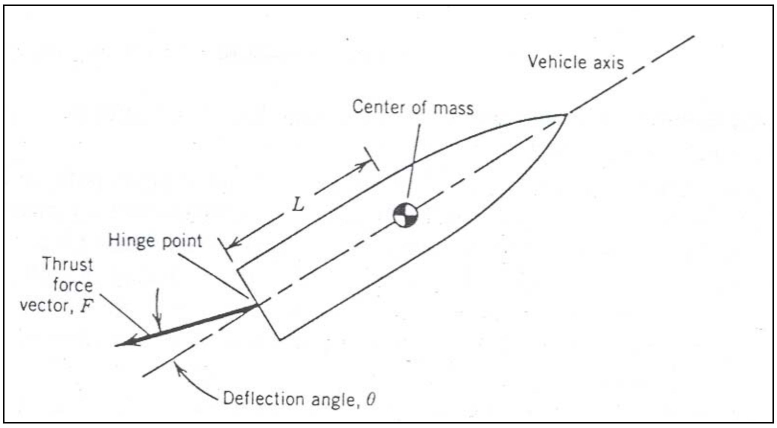

Figure 1-2 Thrust vector control schematic

1.1. TVC Systems in General

There are many successful ways to deflect the thrust vector of the flying vehicle such as using gimbaled nozzles, flexible nozzle joints, jet vanes/tabs, jetavators, secondary injectants, and etc. as shown in Fig.1-3 . These mechanisms can be classified into four main groups [2].

- Mechanical deflection of the nozzle or thrust chamber (gimbal or hinge schemes and movable nozzles).
- Positioning of heat-resistant movable bodies into the exhaust jet, and providing external aerodynamic forces on the bodies resulting the deflection of exhaust gas flow (jet vanes/tabs and jetavators).
- Injection of a secondary fluid into the divergent section of the nozzle, causing an asymmetrical distortion of the exhaust gas flow (secondary injection liquid or gas).
- Separate thrust producing devices that are not part of the main flow through the nozzle (auxiliary thrust chambers).

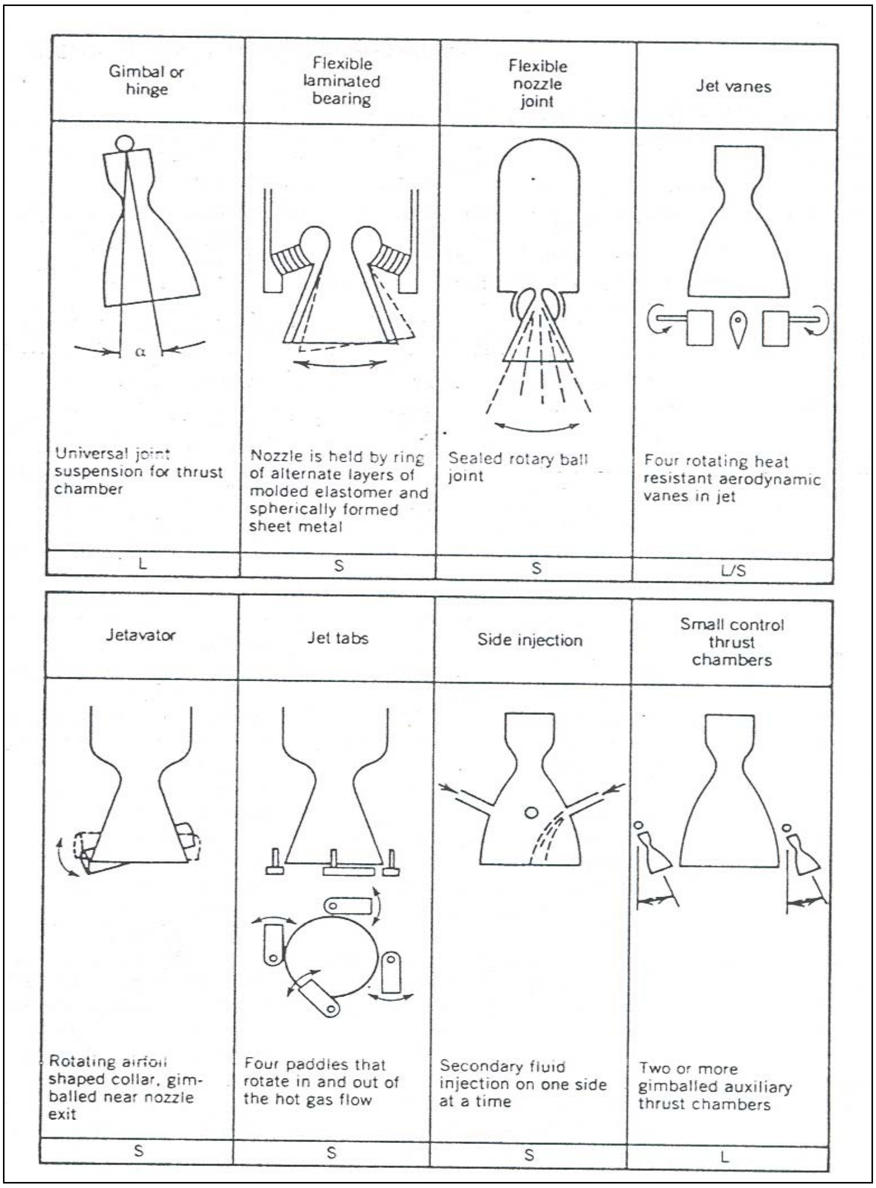

Figure 1-3 TVC techniques [2]

The assessment of these techniques in terms of performance, weight, ease to handle and manipulate, complexity, and compactness together with technological provability is denoted in Table 1-1.

Table 1-1 Advantages and disadvantages of various TVC systems [2]

Type	L/S[a]	Advantages	Disadvantages
Gimbal or hinge	L	Simple, proven technology; low torques, low power; ±12° duration limited only by propellant supply; very small thrust loss	Requires flexible piping; high inertia; large actuators for high slew rate
Movable nozzle (flexible bearing)	S	Proven technology; no sliding, moving seals; predictable actuation power; up to ±12°	High actuation forces; high torque at low temperatures; variable actuation force
Movable nozzle (rotary ball with gas seal)	S	Proven technology; no thrust loss if entire nozzle is moved; ±20° possible	Sliding, moving hot gas spherical seal; highly variable actuation power; limited duration; needs continuous load to maintain seal
Jet vanes	L/S	Proven technology; low actuation power; high slew rate; roll control with single nozzle; ±9°	Thrust loss of 0.5 to 3%; erosion of jet vanes; limited duration; extends missile length
Jet tabs	S	Proven technology; high slew rate; low actuation power; compact package	Erosion of tabs; thrust loss, but only when tab is in the jet; limited duration
Jetavator	S	Proven on Polaris missile; low actuation power; can be lightweight	Erosion and thrust loss; induces vehicle base hot gas recirculation; limited duration
Liquid-side injection	S/L	Proven technology; specific impulse of injectant nearly offsets weight penalty; high slew rate; easy to adapt to various motors; can check out before flight; components are reusable; duration limited by liquid supply; ±6°	Toxic liquids are needed for high performance; often difficult packaging for tanks and feed system; sometimes requires excessive maintenance; potential spills and toxic fumes with some propellants; limited to low vector angle applications
Hot-gas-side injection	S/L	Lightweight; low actuation power; high slew rate; low volume/compact; low performance loss	Multiple hot sliding contacts and seals in hot gas valve; hot piping expansion; limited duration; requires special hot gas valves; technology is not yet proven
Hinged auxiliary thrust chambers for high thrust engine	L	Proven technology; feed from main turbopump; low performance loss; compact; low actuation power; no hot moving surfaces; unlimited duration	Additional components and complexity; moments applied to vehicle are small; not used for 15 years in USA
Turbine exhaust gas swivel for large engine	L	Swivel joint is at low pressure; low performance loss; lightweight; proven technology	Limited side forces; moderately hot swivel joint; used for roll control only

[a] L, used with liquid propellant engines; S, used with solid propellant motors.

1.2. SITVC System

Among different techniques to generate deflection of thrust vector of a rocket system, Secondary Injection Thrust Vector Control (SITVC, a shock producing

TVC technique) has been used in various systems successfully since 1960's and is accomplished by injecting a secondary fluid inside the supersonic flow from the diverging part of the converging-diverging nozzles. On contrary to mechanically operating TVC systems, such as gimbaled nozzles, jet vanes/tabs, etc., which require actuators to deflect mechanical parts, SITVC does not require any moving parts and regulated by the fluid injection, which reduces axial thrust force losses while changing the direction of the vector [2]. The secondary fluid injected, creates an unsteady complex three-dimensional flow field inside the nozzle. This complex flow field includes not only a strong bow-shock creating asymmetry and a weak separation shock due to boundary layer separation upstream of the injection location but also a Mach disc and reattachment region accompanied by recompression downstream of the injection location [3-5] as shown in Fig.1-4.

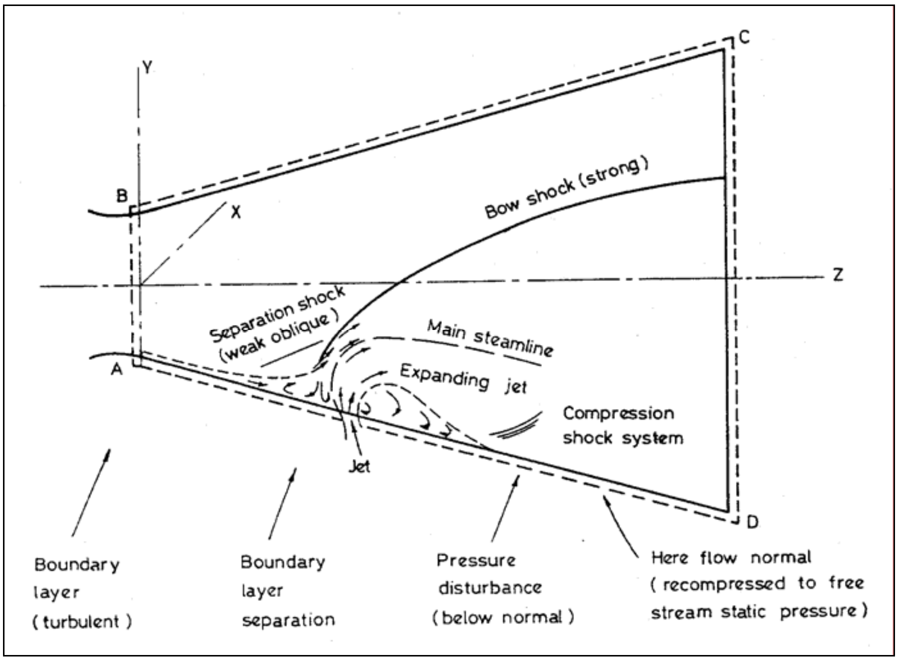

Figure 1-4 Complex flow structure associated with SITVC [3]

The causes of the deflection or more appropriately the side force to create deflection over the body are primarily the downstream asymmetrical pressure distribution on nozzle wall due to this strong bow shock and secondarily the normal component of the momentum of the secondary injectant [6]. This is because of the fact that the injected fluid acts as an obstruction in the supersonic flow creating strong bow shock, and consequently 80-90% of the side force is due to the downstream asymmetrical pressure distribution (or pressure rise) depicted in Fig. 1-5 on the nozzle wall whereas the momentum of the injected fluid is responsible for the rest [6]. Another aspect of SITVC is that the moment arm of the resultant force is bigger than the mechanical TVC techniques enabling to have lesser side forces since the ratio of the side force to the axial force allowed by this technique is limited [1-8].

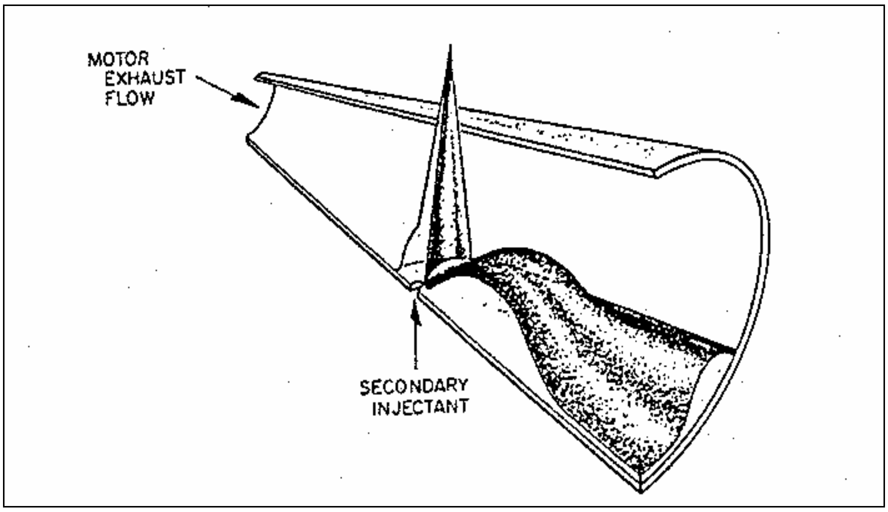

Figure 1-5 Pressure rise associated with SITVC [5]

The injected secondary fluid can be gas (HGITVC, hot gas injection TVC) or liquid (LITVC, liquid injection TVC) depending upon their performance as shown in Fig. 1-6, furthermore its choice is dependent on the injectant constitutions, mission and complications encountered when assembling to main propulsion system as depicted in Table 1-1. Secondary fluid can be supplied from a separate gas generator or can be an inert gas stored separately or tapped from the main motor as bleed [1]. Typical chamber bleed configurations for SITVC applications are shown in Fig. 1-7. Moreover a literate survey on global SITVC applications is shown in Appendix A using Ref. [9].

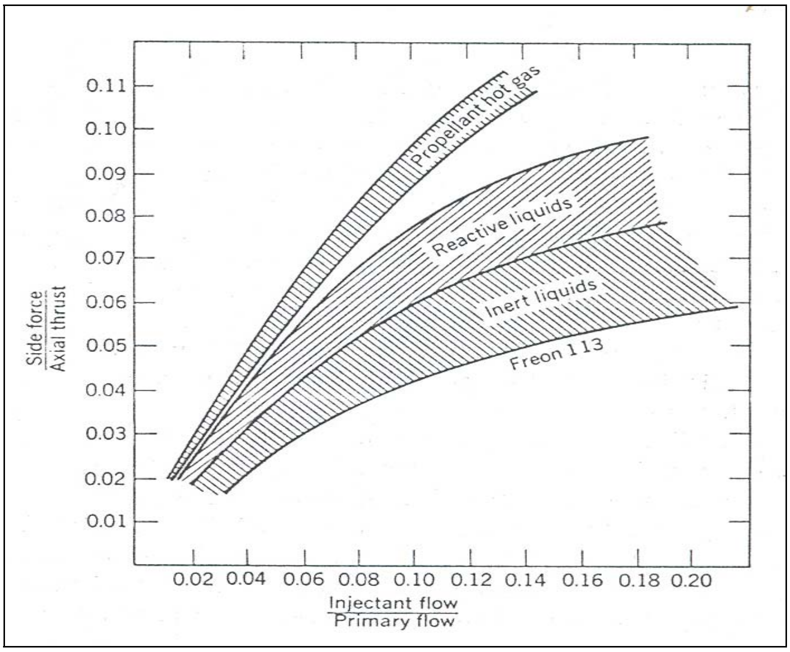

Figure 1-6 Performance characteristics of different injectants [2]

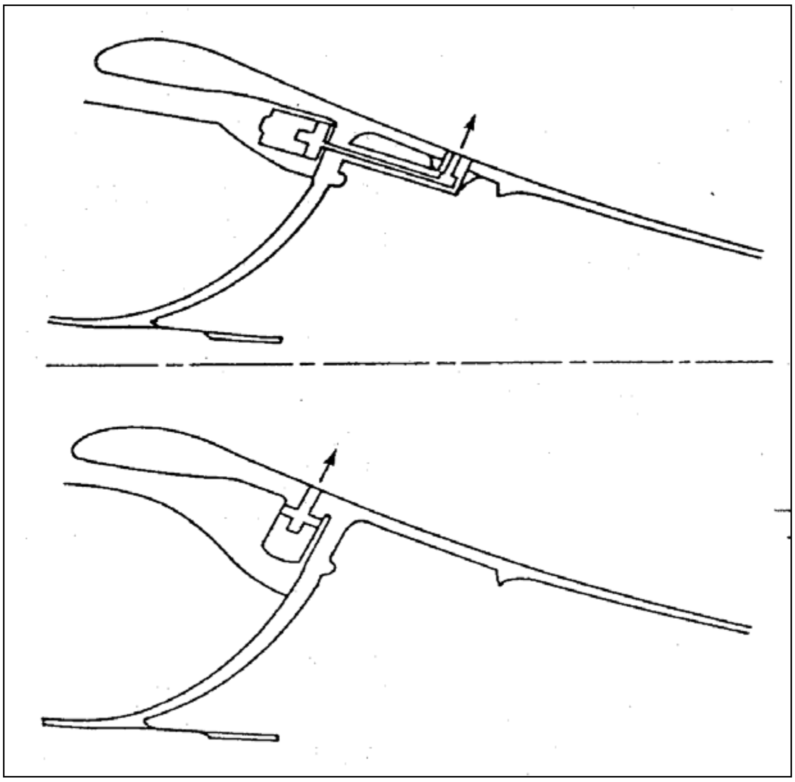

Figure 1-7 Typical chamber bleed systems for SITVC applications [4]

1.3. Earlier Studies of SITVC and Thesis Objective

Since the interaction of secondary jet with the main flow is quite complex, as a matter of fact it is named as "jets in supersonic crossflow" in literature, earlier studies focused on both theoretical tools such as Blast-wave analogy [5] to model the penetration of the secondary jet into main flow and experiments with cold flow tests [8] and also real firing tests [10, 11]. However theoretical models hold only for very low injection flow rates and lack generality whereas both cold flow tests and static firing tests provide precious SITVC data to be used for further analyses although they only provide macroscopic performance estimations and are costly. On the other hand Computational Fluid Dynamics (CFD) has been developed to examine detailed microscopic behavior of fluid flows becoming a strong alternative to previous theoretical models and a complimentary element to experiments. Consequently, the detailed flow field analysis inside rocket nozzles with injection has been made possible with numerical tools. Balu [3] solved three dimensional Euler equations for the prediction of SITVC performance and integrated nozzle wall pressure distributions to yield performance parameters. Recently, Dhinagaran [12] solved numerically both Euler and Navier-Stokes equations in two dimensional nozzles and compared them to each other concluding that Navier-Stokes (N-S) equations with an algebraic turbulence model being more accurate. Ko [6] solved three dimensional N-S equations in a conical rocket nozzle both with an algebraic turbulence model and a two equation (k-ε) turbulence model with low Reynolds number treatment. In addition, it is stated that two different models made very little difference in the prediction of this flowfield and it was noted that the reason for that might be the effect of compressibility on turbulence was not completely modeled instead a correction was implemented in case of k-ε model.

The present study aims at the investigation of flowfield inside a specific conical rocket nozzle in presence of secondary injection and the prediction of the variation of global SITVC performance parameters such as thrust ratio, amplification and axial thrust augmentation (mentioned in the next chapter in detail) with basic SITVC parameters, which are injection mass flow rate, injection location and injection angle.

CHAPTER 2

METHODOLOGY

The main methodology followed in this study is the numerical solution of Reynolds-Averaged three dimensional Navier-Stokes equations with a turbulence closure inside a rocket nozzle with injection with the help of a commercial CFD package, called FLUENT®. In addition, an experimental setup for the cold flow tests of SITVC aiming CFD validation was planned to be established, the layout of experimental setup was drawn, fundamental hardware was selected and preliminary testing without injection was accomplished using compressor system, nozzle and Scanivalve system. However due to the lack of funding the continuation of this research was cut. The detailed description of the experimental setup is mentioned in Appendix E. Therefore this study eventually involves only the numerical part in essence.

2.1. Computational Fluid Dynamics (CFD) Background

The equations governing the fluid motion (explained in Appendix B) are partial differential equations that are non-linear in nature due to convective terms; therefore the analytical solution of these equations, except for simple cases, is not possible. As a consequence numerical tools are developed to simulate the flow behavior with appropriate boundary conditions (BCs). As a general philosophy of the numerical methods, the flow field of interest is discretized (covered and replaced) by a set of cells, called the mesh or solution grid and then the governing equations of the fluid flow are discretized using specific discretization schemes and applied to each cell, resulting a system of algebraic equations for the whole domain

[13-15]. Afterwards this system of equations is solved using various solution strategies with respecting the trade-off between the computational cost and the accuracy of the solution.

2.1.1. Discretization of Governing Equations

FLUENT® uses a control-volume-based technique to convert the governing equations to algebraic equations that can be solved numerically over a flow domain that is discretized into finite control volumes shown in Fig.2-1. This technique consists of integrating the governing equations about each control volume, yielding discrete equations that conserve each quantity on a control-volume basis [13].

The governing equations are expressed in the form of generalized transport equations as in differential form (Eq. 2-1) and later on in integral form (Eq. 2-2) suitable for finite volume approach. In these equations the terms can be summed up into four categories: transient (or unsteady) term, convection (or advection) term, diffusion term (surface forces) and the source term (body forces) [13]. In these equations the variable ϕ is conserved intensive quantity per unit volume of corresponding to the extensive quantity (V without vector sign states volume).

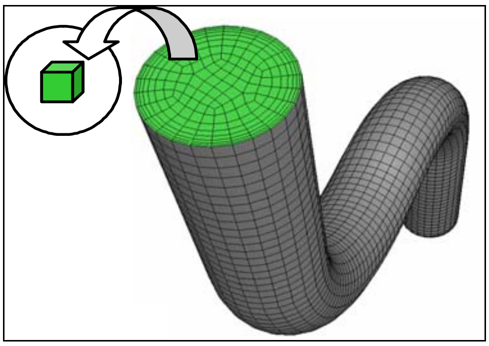

Figure 2-1 Discretization of domain into finite volumes

$$\frac{\partial \rho\phi}{\partial t} + \nabla \cdot \left(\rho\phi\vec{V}\right) = \nabla \cdot \left(\Gamma \nabla \phi\right) + S_{\phi} \qquad (2\text{-}1)$$

$$\int_V \frac{\partial \rho\phi}{\partial t} dV + \int_V \nabla \cdot \left(\rho\phi\vec{V}\right) dV = \int_V \nabla \cdot (\Gamma \nabla \phi) dV + \int_V S_\phi dV \qquad \text{(2-2)}$$

Note that in these equations ϕ takes the values of *1* for continuity equation, $\vec{V}$ (velocity in three directions) for the momentum equation and *e* (internal or total energy per unit volume) for conservation of energy. Each term can be discretized and approximated within a control volume as follows in Equations 2-3 to 2-6 [13, 14]:

Transient Term

$$\int_V \frac{\partial \rho\phi}{\partial t} dV = \frac{V\left[(\rho\phi)^{n+1} - (\rho\phi)^{n}\right]}{\Delta t} \qquad \text{(2-3)}$$

where *n+1* denotes the current time level, and *n* the previous one

Convective Term

$$\int_V \nabla \cdot \left(\rho\phi\vec{V}\right) dV = \int_S \left(\rho\phi\vec{V} \cdot \vec{n}\right) dS = \sum_f (\rho S V)_f \phi_f \qquad \text{(2-4)}$$

where *f* means on each face of cell and ϕ_f is an interpolation of the values of ϕ at the center of the surrounding cells. And the fluxes of ϕ are summed up in each cell.

Diffusive Term

$$\int_V \nabla \cdot (\Gamma \nabla \phi) dV = \int_S \Gamma (\nabla \phi) \cdot \vec{n} dS = \sum_f \Gamma_f \left(\frac{\partial \phi}{\partial n}\right)_f S_f \qquad \text{(2-5)}$$

where $\left(\frac{\partial\phi}{\partial n}\right)_f$ is the partial derivative of ϕ along the face normal, *n*.

Source Term

$$\int_V S_\phi dV = \int_V \left(G_U + G_{p\phi}\right)dV = \left(G_U + G_{p\phi}\right)\cdot V \qquad (2\text{-}6)$$

The discrete values of the scalar ϕ at the cell centers ($c0$ and $c1$ in below figure, Fig. 2-2) are stored. However, face values ϕ_f are required for the convection terms must be interpolated from the cell center values. Several discretization schemes are proposed mainly in space discretizations [13] to obtain an approximation of ϕ such as:

- 1st Order Upwind Scheme
- 2nd Order Upwind Scheme
- Higher Order Schemes (third or fourth order schemes, like MUSCL)

Upwinding means that the face value ϕ_f is derived from quantities in the cell upstream [13], or "upwind" relative to the direction of the normal velocity, U_n.

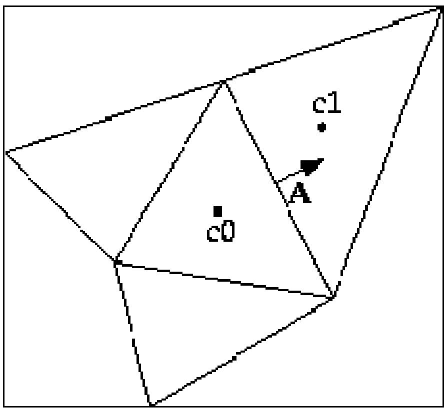

Figure 2-2 Computational stencil

When first-order accuracy is desired, quantities at cell faces are determined by assuming that the cell-center values of any field variable represent a cell-average value and hold throughout the entire cell; the face quantities are identical to the cell quantities. Thus when first-order upwinding is selected, the face value ϕ_f is set equal to the cell-center value of ϕ in the upstream cell. When second-order accuracy is desired, quantities at cell faces are computed using a multidimensional linear reconstruction approach. In this approach, higher-order accuracy is achieved at cell faces through a Taylor series expansion of the cell-centered solution about the cell centroid [13]. Thus when second-order upwinding is selected, the face value ϕ_f is computed using the following expression:

$$\phi_f = \phi + \nabla\phi \cdot \Delta\vec{s} \tag{2-7}$$

where ϕ and $\nabla\phi$ are the cell-centered value and its gradient in the upstream cell, and $\Delta\vec{s}$ is the displacement vector from the upstream cell centroid to the face centroid. This formulation requires the determination of the gradient $\nabla\phi$ in each cell. This gradient is computed using the divergence theorem, which in discrete form is written as:

$$\nabla\phi = \frac{1}{V}\sum_{f}^{Nfaces} \tilde{\phi}_f \cdot \vec{S} \tag{2-8}$$

Here the face values ϕ_f are computed by averaging ϕ from the two cells adjacent to the face. Finally, the gradient $\nabla\phi$ is limited so that no new maxima or minima are introduced or basically for the prevention of oscillations in the solution [13].

In terms of temporal discretization, the integral form of governing equations is expressed in Eq. 2-9 and convective, diffusion terms are replaced by the summation operator over a cell and the resulting equation is given as follows [13,16]:

$$V_{\mathrm{i}} \frac{\partial \phi_i}{\partial t} + \sum_{j=1}^{N_i} [H_n]_{i,j} \Delta S_{i,j} = 0 \tag{2-9}$$

where $\Delta S_{i,j}$ is the ith cell's jth surface area and $[H_n]_{i,j}$ is the net flux (convective and viscous fluxes) flowing into ith cell from jth surface of the same cell. *N* is the number of surfaces in a cell. Then the residual Ri is defined as below in Eq. 2-10, at steady state this term should go to zero.

$$R_i = \sum_{j=1}^{N} [H_n]_{i,j} \Delta S_{i,j} \tag{2-10}$$

By expressing this residual term in the same iteration level (i.e. time level) implicit solution technique is obtained as shown in Eq. 2-11, which has no restriction of marching in time (Courant -Lewy-Friedrich's condition or CFL number can be of value of anything).

$$\phi_i^{n+1} = \phi_i^{n} - \frac{\Delta t}{V_{\mathrm{i}}} R_i^{n+1} \tag{2-11}$$

Then Ri at time level n+1 can be expressed using Taylor series expansion as follows;

$$R_i^{n+1} = R_i^{n} + \frac{\partial R^{n}}{\partial t} \cdot \Delta t + \ldots \tag{2-12}$$

Then the derivative of residual with respect to time can be expressed using chain law afterwards the above equation becomes;

$$R_i^{n+1} = R_i^{n} + \frac{\partial R^{n}}{\partial t} \cdot \Delta t = R_i^{n} + \frac{\partial R^{n}}{\partial \phi} \cdot \frac{\partial \phi}{\partial t} \cdot \Delta t = R_i^{n} + \frac{\partial R^{n}}{\partial \phi} \cdot \Delta \phi^{n} \tag{2-13}$$

The derivative of residual with respect to conserved variables, $\partial R^n / \partial \phi$ is named "Flux Jacobian" and it needs to be computed for implicit methods. Finally Eq. 2-13 is inserted into Eq. 2-11 to yield eventual expression for implicit schemes;

$$\frac{V_{\mathrm{i}}}{\Delta t} \cdot \Delta \phi_i^{\ n} + \frac{\partial R^{\ n}}{\partial \phi} \cdot \Delta \phi_i^{\ n} = -R_i^{\ n} \qquad (2\text{-}14)$$

where $\Delta \phi_i^{\ n} = \phi_i^{\ n+1} - \phi_i^{\ n}$

However for the explicit solution technique, this term is expressed at previous time step as in Eq. 2-15 and CFL number should be less than or equal to 1 for matching of physical domain with computational domain [15].

$$\phi_i^{\ n+1} = \phi_i^{\ n} - \frac{\Delta t}{V_{\mathrm{i}}} R_i^{\ n} \qquad (2\text{-}15)$$

FLUENT® uses both explicit and implicit methods with multidirectional upwinding schemes, but for the sake of accuracy implicit methods are preferable in compressible flows. As a general remark explicit methods are less accurate take longer times to converge, have stability limitations (CFL condition) but are easier to construct and require less computer resources whereas implicit methods are accurate, don't have stability problems but are difficult to construct due to computation of this Flux Jacobians and require more resources.

2.1.2. Discretization of Flow Domain

Since FLUENT® is an unstructured solver; it uses internal data structures to assign an order to the cells, faces, and grid points in a mesh and to maintain contact between adjacent cells. It does not, therefore, require i,j,k indexing to locate neighboring cells. This gives the flexibility to use the grid topology that is best for the problem, since the solver does not force an overall structure or topology on the grid. GAMBIT®, which is the preprocessor or the mesh-generator of FLUENT®, allows the construction of various types of meshes such as in 2D, quadrilateral and triangular cells are accepted, and in 3D, hexahedral, tetrahedral, pyramid, and wedge cells can be used. (Fig. 2-3 depicts each of these cell types.) Obviously, the choice of which mesh type to use will depend on the application, i.e. the flowfield to be resolved such as different structures embedded in the flow and the wall effects in wall bounded flows, etc..

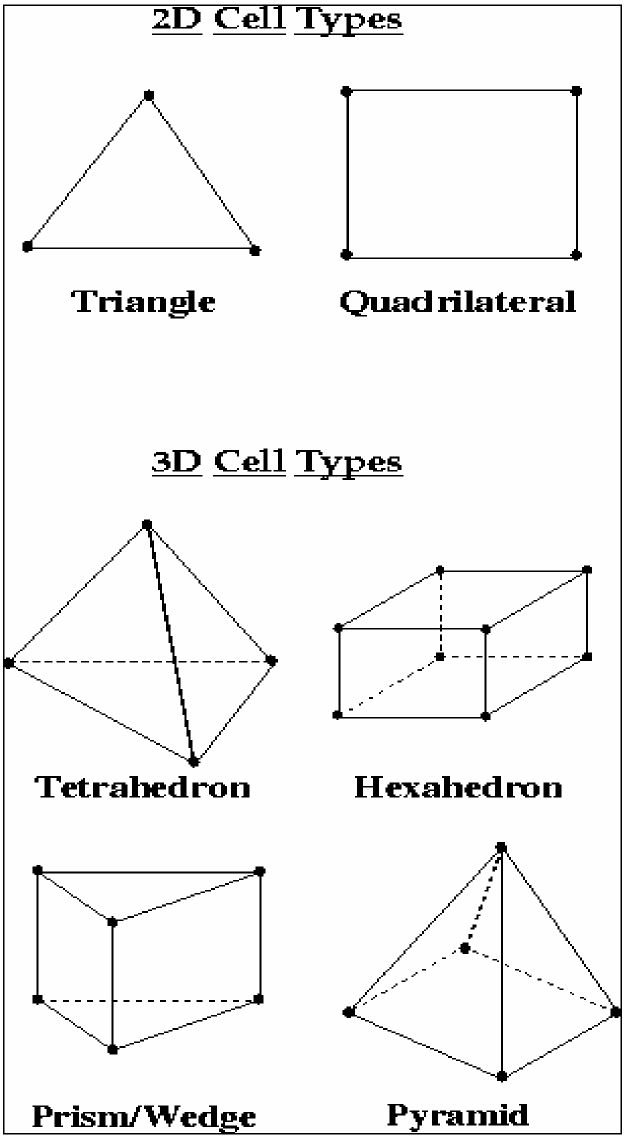

Figure 2-3 Various mesh types provided by GAMBIT®

When choosing mesh type, the following issues should be considered [13]:

1. Setup time

2. Computational expense

3. Numerical diffusion

Setup Time

Setup time for complex geometries is, therefore, the major motivation for using unstructured grids employing triangular or tetrahedral cells. If the geometry is relatively simple structured grids can be employed, however there is no clear time saving.

Computational Expense

When geometries are complex or the range of length scales of the flow is large, an unstructured triangular/tetrahedral mesh can often be created with far fewer cells than the equivalent mesh consisting of quadrilateral/hexahedral elements. This is because a triangular/tetrahedral mesh allows cells to be clustered in selected regions of the flow domain especially using size functions, whereas structured quadrilateral/hexahedral meshes will generally force cells to be placed in regions where they are not needed. It is quite obvious that the regions with high gradients of flow variables (stagnation points, shock waves, boundary layers and mixing layers, etc.) should be taken care of by clustering the grid around these regions. Therefore the versatility of unstructured meshes provides computationally reasonable simulations. Unstructured quadrilateral/ hexahedral meshes offer many of the advantages of triangular/tetrahedral meshes for moderately-complex geometries. One characteristic of quadrilateral/hexahedral elements that might make them more economical in some situations is that they permit a much larger aspect ratio than triangular/tetrahedral cells. A large aspect ratio in a triangular/tetrahedral cell will invariably affect the skewness of the cell, which is undesirable as it may impede accuracy and convergence [13].

Numerical Diffusion

A dominant source of error in multidimensional situations is numerical diffusion, also termed false diffusion. (The term “false diffusion” is used because the diffusion is not a real phenomenon, yet its effect on a flow calculation is analogous to that of increasing the real diffusion coefficient.) The following points can be made about numerical diffusion:

Numerical diffusion is most noticeable when the real diffusion is small, that is, when the situation is convection-dominated. All practical numerical schemes for solving fluid flow contain a finite amount of numerical diffusion. This is because numerical diffusion arises from truncation errors that are a consequence of representing the fluid flow equations in discrete form.

The second-order discretization scheme used in FLUENT® can help reduce the effects of numerical diffusion on the solution as mentioned above. The amount of numerical diffusion is inversely related to the resolution of the mesh. Therefore, one way of dealing with numerical diffusion is to refine the mesh. Numerical diffusion is minimized when the flow is aligned with the mesh.

2.2. Turbulence Modeling

Unlike laminar flow, in which the flow behaves in a manner of layers and the mixing is not pronounced, turbulent flows involve oscillating, irregular, unsteady 3D motion of particles where mixing is highly promoted. Within the content of these chaotic, fluctuating nature of flows there exits wide spectrum of time and length scales through the motion of swirling structures called Eddies. As a matter of fact these Eddies are produced through the interaction of mean flow and the disturbances contained in the flow and they basically transfer the turbulent kinetic energy (i.e. transfer of momentum) to the smaller Eddies to the smallest Eddies where the energy of turbulence is dissipated through viscosity, it is called "Energy cascade for turbulence" and shown in Fig. 2-4. In fact turbulent flows are always energetic and chaotic on the other hand they are dissipative [14].

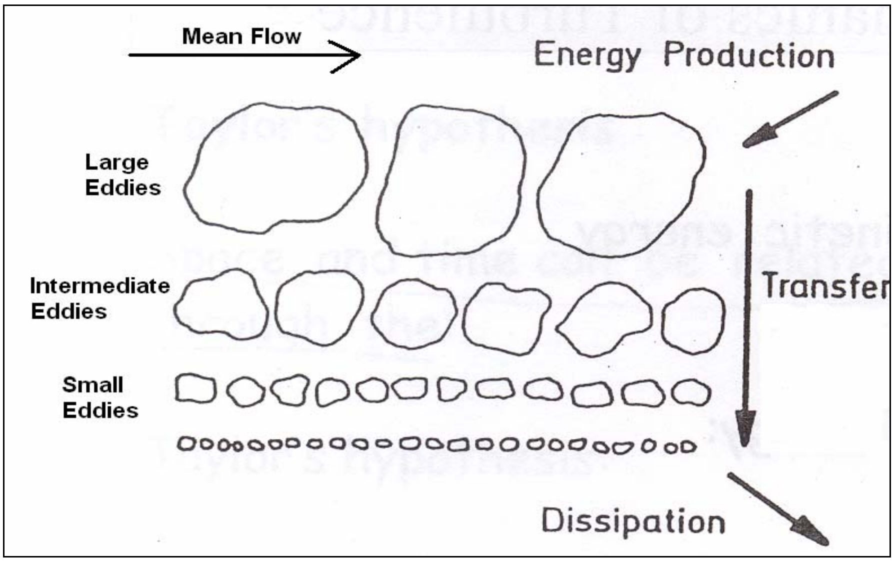

Figure 2-4 Energy cascade of turbulence

The main need for the turbulence modeling comes from the fact that it is technically very difficult, practically impossible to resolve all the structures of turbulence at a very wide range of motion and scales. In other words the frequency spectrum (of the Eddies for instance, or motions) of turbulent flows is so large that these irregular motions can not be fully captured unless Direct Numerical Simulation (DNS) is applied. In fact DNS is known to be most time and memory consuming and thus most computationally expensive approach to resolve turbulence and in addition the applicability is limited to the computer memory since it requires extremely fine computational meshes, as a consequence only low Reynolds number flows are handled with DNS [13, 17].

Therefore for the practical use, turbulence should be somehow modeled or simulated in order to have the effect of Eddies on the mean flow. This is done using turbulence models, providing link between the fluctuating structures to mean flow [18, 20]. It is an unfortunate fact that no single turbulence model is universally accepted as being superior for all classes of problems. The choice of turbulence model depends on considerations such as the physics encompassed in the flow, the established practice for a specific class of problem, the level of accuracy required, the available computational resources, and the amount of time available for the simulation [13]. In addition to the governing equations some models require either one or two (Reynolds Averaged Navier Stokes models, (RANS)) or even more equations (Reynolds Stresses Modeling, RSM) to be solved all together, or in very simple models an algebraic approach is used (Prandtl's mixing length theory).

In Reynolds averaging, the solution variables in the instantaneous (exact) Navier-Stokes equations are decomposed into the mean (ensemble-averaged or time-averaged) and fluctuating components as in Eq. 2-16 by applying Reynolds Decomposition. For the velocity components [17]:

$$u(x, y, z, t) = \overline{u}(x, y, z) + u'(t) \qquad \text{(2-16)}$$

where $\overline{u}$ is the mean velocity or averaged velocity and u' is the fluctuation. Likewise for pressure or scalar quantities, ϕ , Eq. 2-17 states:

$$\phi = \overline{\phi} + \phi' \qquad \text{(2-17)}$$

This decomposition (decomposing into mean and fluctuating parts) is the basis of statistical models, which are RANS models. If the Reynolds Decomposition is applied on the continuity and momentum equations and time averaging is utilized afterwards these equations become as follows in indicial notation:

$$\frac{\partial \rho}{\partial t}+\frac{\partial}{\partial x_i}(\rho u_i)=0 \qquad (2\text{-}18)$$

$$\frac{\partial}{\partial t}(\rho u_i)+\frac{\partial}{\partial x_j}(\rho u_i u_j)=-\frac{\partial p}{\partial x_j}+\frac{\partial}{\partial x_j}\left[\mu\left(\frac{\partial u_i}{\partial x_j}+\frac{\partial u_j}{\partial x_i}-\frac{2}{3}\delta_{ij}\frac{\partial u_i}{\partial x_i}\right)\right]+\frac{\partial}{\partial x_j}\left(-\rho\overline{u_i' u_j'}\right)$$

(2-19)

Now a new term appears that is the correlation of u_i' with u_j' (Reynolds Stresses), this term needs special attention and it is related with the kinetic energy of the fluctuations. That's why the models are used to model that term to close the set of equations. A common approach is to use Boussinesque hypothesis to relate Reynolds Stresses to mean velocity gradients as shown in Eq. 2-20.

$$-\rho\overline{u_i' u_j'}=\mu_t\left(\frac{\partial u_i}{\partial x_j}+\frac{\partial u_j}{\partial x_i}\right)-\frac{2}{3}\left(\rho k+\frac{\partial u_i}{\partial x_i}\right)\delta_{ij} \qquad (2\text{-}20)$$

It is utilized for both one (Spalart-Allmaras) and two equation (k-ε and k-ω) models. The advantage of this approach is the relatively low computational cost associated with the computation of the turbulent viscosity, μ_t. In the case of the Spalart-Allmaras model, only one additional transport equation (representing turbulent viscosity) is solved. In the case of the k-ε and k-ω models, two additional transport equations (for the turbulence kinetic energy, k, and either the turbulence dissipation rate, ε, or the specific dissipation rate, ω) are solved, and μ_t is computed as a function of k and ε. The disadvantage of the Boussinesque hypothesis as presented is that it assumes turbulent viscosity is an isotropic scalar quantity, which is not strictly true [17-20]. The alternative approach, RSM, is to solve transport equations for each of the terms in the Reynolds stress tensor. An additional scale determining equation (for ε) is also required. This makes seven additional equations to solve and brings quite a computational burden, and it is not justified in many cases except for situations in which the anisotropy of turbulence has a dominant effect on the mean flow [17]. For more information on turbulence the reader should refer to Ref [17-20].

2.3. Followed Approach and Performance Definition

The followed approach involves two successive parts for the handling SITVC problem numerically.

The first part is the solution of three dimensional flowfield inside a test case nozzle used by Masuya [8] and Ko [6] with various solution parameters such as distinct mesh sizes, turbulence models and solver types. Afterwards all these different numerical simulations with different solution parameters are compared with the experimental data obtained by Masuya [8] leading to not only the validation of the solver but also the determination of optimum solver parameters for adequate accuracy with reasonable computational cost, which are going to be used in the next part. For the mesh size parameter, three distinct computational grids are constructed regarding two different turbulent wall treatment approaches. Extra attention to physical phenomenon, which is very complex, unsteady, three-dimensional and inherently turbulent, is given when generating grids. For turbulence treatment, again the physical behavior is taken into account. Remembering that a rocket nozzle is always turbulent due to the instabilities in the solid propellant motors, which are at the upstream of nozzle, and in addition in this specific problem the interaction of the secondary jet with the main flow, which is actually boundary layer-shock wave interaction occurring in the neighborhood of injection location, enhances turbulence. As boundary layer separates at upstream, it interacts with the strong bow shock. Therefore the choice for the most suitable turbulence model plays a significant role. In case of turbulence models, one and two equation turbulence models (Spalart-Allmaras model, k-ε and k-ω models) are used in this study. And finally for the solver types two different solvers are used; coupled and segregated solvers. The segregated and coupled approaches differ in the way that the continuity, momentum, and (where appropriate) energy and species equations are solved: the coupled solver simultaneously solves governing equations and following the sequence shown in Fig.2-5 whereas the segregated solver solves these equations sequentially based on pressure velocity coupling and following the sequence shown in Fig.2-6 [13]. For the segregated solver only implicit time stepping is available however for coupled solvers both implicit and explicit time discretizations can be used.

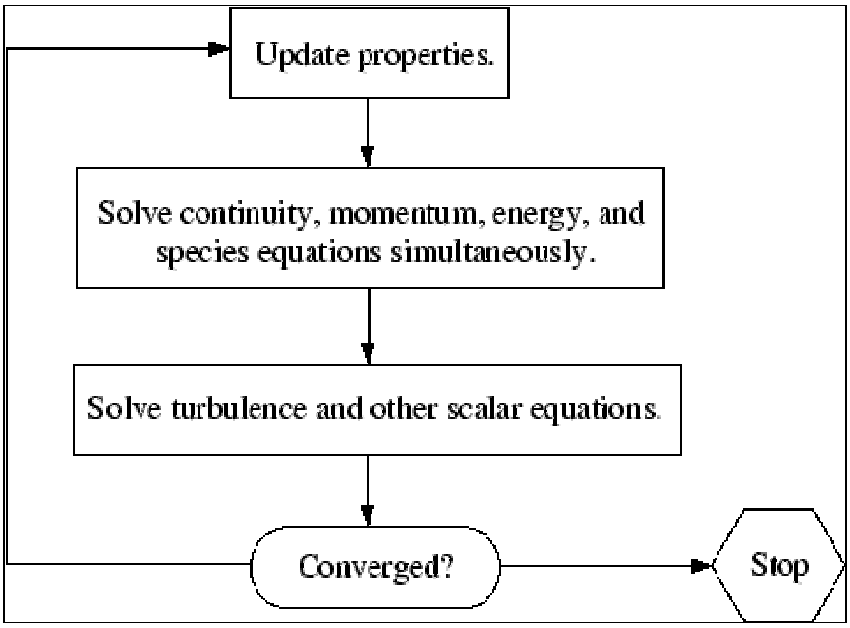

Figure 2-5 Coupled solvers flow chart

For this study segregated implicit and coupled explicit solves are tested, coupled implicit solver is discarded due to memory restrictions. Moreover for the spatial discretization of the fluid flow equations second-order upwind scheme is used for both flow and turbulence for high accuracy. However firstly the simulations are started with first order upwind scheme and after they converge, the scheme is changed to second order upwinding and final convergence is attained for the segregated solver. For the coupled solver the numerical scheme is chosen as second order upwinding from the start. Convergence is commonly measured by the orders of drop in residuals of continuity; momentum and energy with turbulence quantities (k and ε or ω, or υ), therefore residuals are plotted to decide for convergence in addition to velocity plots at certain locations and mass imbalance values. For speeding up convergence a sophisticated initialization method is utilized that is Full Multigrid initialization (FMG initialization). It can provide a better initial and approximate solution, instead of constant initial values specified at boundaries, at a minimum cost to the overall computational expense [13]. In the FMG iteration, the inviscid Euler equations are solved using coupled explicit solver with first order-discretization to obtain the approximate solution then the simulation is commenced with initially selected solver with the original solver settings staring from this initial condition. However, turbulence equations or any other transport scalars are not solved in the FMG initialization [13]. Finally under-relaxation factors for both solvers and CFL number for the coupled solver are set to proper values to ensure numerical stability.

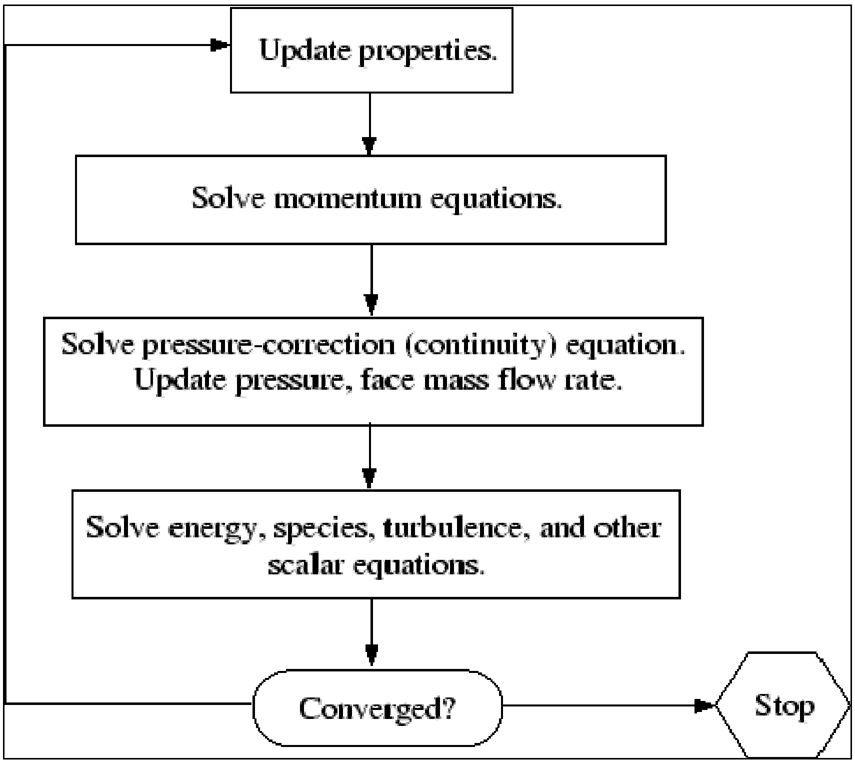

Figure 2-6 Segregated solvers flow chart

The second part of the study involves the solution of three dimensional flowfield inside a typical conical rocket nozzle with various SITVC parameters mentioned in

Introduction section. Once the optimum solution parameters have been set in the first part for test case nozzle, they are used without any doubt in this different rocket nozzle. Of course another grid dependency study is essential and done with three distinct computational grids for this geometry. A test matrix has been constructed and several runs have been accomplished to investigate the dependence of global SITVC performance on SITVC parameters. Global performance parameters are thrust ratio, amplification and axial thrust augmentation respectively.

Thrust ratio (TR) is the ratio of the side thrust force to axial thrust force, amplification (K) is the ratio of side specific impulse (*Isp*)s to main or primary axial specific impulse (*Isp*)p and it determines the amount of fluid to be injected to have a specified side force [1,6]. And the last one, axial thrust augmentation, is the ratio of the augmented axial impulse (Δ*Isp*)p to main specific axial impulse and is a measure of the penalty of the overall system to obtain this side force [1, 6]. All parameters are expressed as shown in Equations 2-21 to 2-23.

$$TR = \frac{F_s}{F_p} = \frac{R_y}{R_x} \tag{2-21}$$

$$K = \frac{Isp_s}{Isp_p} = \frac{F_s / m_s}{F_p / m_p} = \frac{R_y / m_s}{R_x / m_p} \tag{2-22}$$

$$ATA = \frac{\Delta Isp_p}{Isp_p} = \frac{\Delta F_p / m_s}{F_p / m_p} = \frac{\Delta R_x / m_s}{R_x / m_p} \tag{2-23}$$

If all these performance parameters are known the global effect of a SITVC system can be evaluated. However in order to accurately estimate these parameters, axial thrust and side forces should be computed accurately. The computation of side force involves the integral of pressure distribution over the nozzle wall and then added to the momentum of the injectant. Specifically for side thrust force calculation only the divergent section of the nozzle is considered and pressure and shear stress is integrated over this section to be complete and the effect of injection is always compared to the case without injection. Furthermore the augmented axial thrust is computed from the differential between injection case and no-injection case. Unlike what Ko [6] and Balu [3] did for the evaluation of side and axial thrust forces, a different approach based on simple force balance for a control volume on the rocket nozzle is followed to find R_x and R_y resultants and none of the terms is neglected except the shear stress on inlet and outlet surfaces, which is really small compared to the effect of pressure.

CHAPTER 3

PART ONE - TEST CASE NOZZLE

3.1. Nozzle Geometry and Boundary Conditions

As mentioned in previous chapters, for this part test case nozzle by Masuya[8] and Ko[6] is used with specified inlet boundary conditions (P_0=2MPa, T_0=616K and M=0.2). The injection is sonic, has same reservoir conditions as inlet and it is normal to the nozzle wall through a single orifice located at 30mm from the nozzle throat. Both fluids are air and mass flow rate of secondary jet is 2.4% of the main mass flow rate. The experimental data consisted of Mach number data along symmetry lines at planes located 50mm and 70mm from nozzle throat and in addition Mach number distribution at the exit plane. Thus the experimental data on symmetry lines are used to compare qualitatively the flowfields in terms of profiles whereas Mach number distribution is used for quantitative comparison in terms of main flow structures.

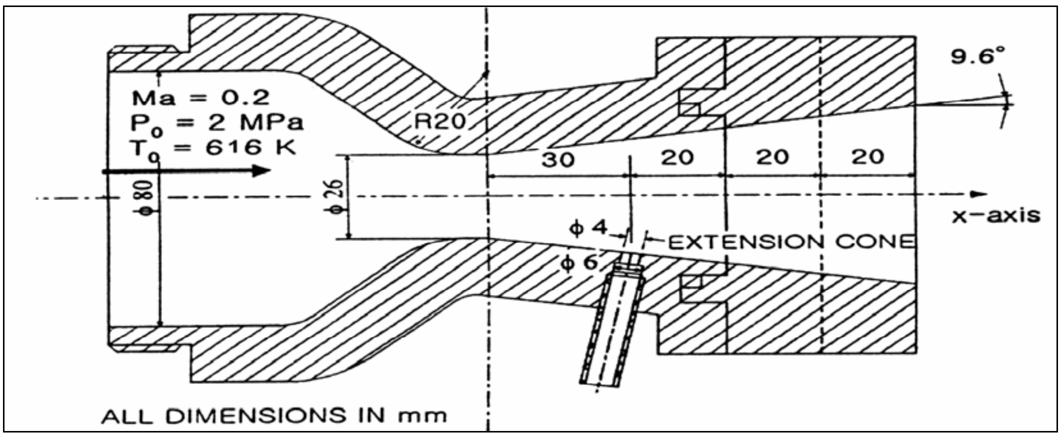

Figure 3-1 Test case nozzle with dimensions [8]

In terms of boundary conditions the ones suitable to this SITVC problem are picked, which is essentially "sonic jet into supersonic crossflow" problem. The flow is compressible and governed by hyperbolic partial differential equations. Compressible flows are typically characterized by the total pressure P_0 and total temperature T_0 of the flow. For an ideal gas, these quantities can be related to the static pressure and temperature by the following equations:

$$\frac{p_0}{p} = \left(1 + \frac{\gamma - 1}{2} M^2\right)^{\gamma/(\gamma-1)} \quad (3\text{-}1)$$

$$\frac{T_0}{T} = \left(1 + \frac{\gamma - 1}{2} M^2\right) \quad (3\text{-}2)$$

These relationships describe the variation of the static pressure and temperature in the flow as the velocity (Mach number) changes under isentropic conditions. In addition for compressible flows, the ideal gas law is written in the following form:

$$\rho = \frac{p}{\frac{R}{M_w} T} \quad (3\text{-}3)$$

where p is the local static pressure relative to the operating pressure, R is the universal gas constant, and M_w is the molecular weight. The temperature, T, will be computed from the energy equation.

The commonly used inlet and exit boundary condition options in FLUENT® are as follows [13]:

- Pressure inlet boundary conditions are used to define the total pressure and other scalar quantities at flow inlets.

- Pressure outlet boundary conditions are used to define the static pressure at flow outlets (and also other scalar variables, in case of backflow).

- Pressure far-field boundary conditions are used to model a free-stream compressible flow at infinity, with free-stream Mach number and static conditions specified. This boundary type is available only for compressible flows.

The inlet and injection BCs are basically pressure inlet type, the outlet boundary condition is pressure outlet and the middle plane is symmetry obviously whereas the rest is wall as shown in Fig. 3-2. The list of required variables for these BCs is noted below.

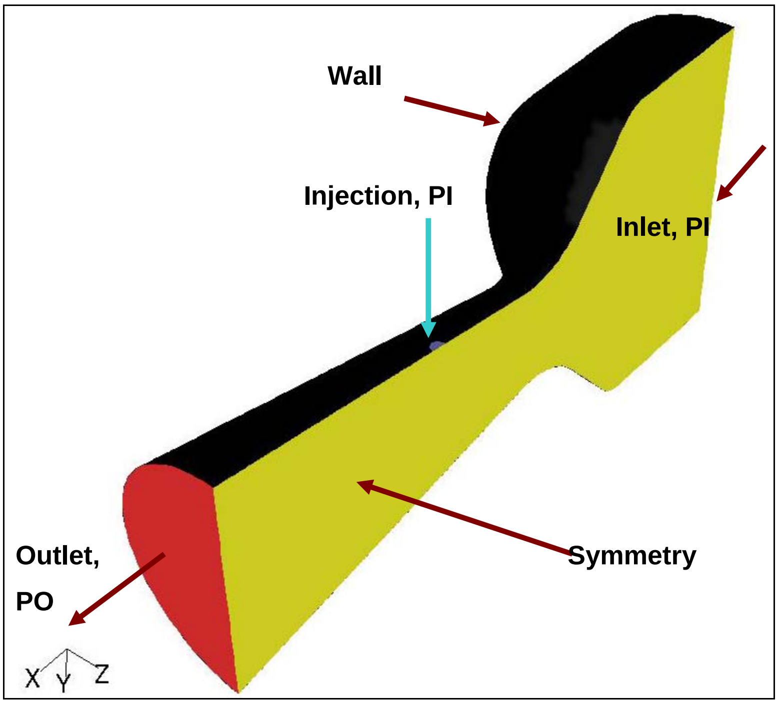

Figure 3-2 Computational domain with boundary conditions

FLUENT® uses following variables to be defined at inlets (pressure inlet BC):

- Total (stagnation) pressure
- Total (stagnation) temperature
- Flow direction
- Static pressure
- Turbulence parameters

In case of total pressure and static temperature the specified values are given, for the static pressure Eq. 3-1 is utilized, and for flow direction normal to boundary injection is used. Moreover for the turbulence parameters such as "eddy" turbulent viscosity for Spalart-Allmaras model or turbulence kinetic energy, k and turbulence dissipation rate, ε for *k*-ε turbulence models or specific dissipation rate, ω for *k*-ω models are to be specified at the boundaries. These specifications can also be done in terms of Turbulence Intensity (TI), and length scale (or hydraulic diameter, D_h). Alternative ways for specifying turbulence conditions at boundaries can be found in [13]. For simplicity and avoiding confusion TI and D_h are selected for turbulence specification method at boundaries. For moderately turbulent flows like the ones in rocket nozzles 5% of TI is appropriate and hydraulic diameter is dependent upon geometry regardless of the turbulence model that is used. That is the inlet radius for the half geometry.

FLUENT® uses following variables to be defined at outlets (pressure outlet BC):

- Static pressure
- Backflow conditions
- Total (stagnation) temperature (for energy calculations in case of backflow)
- Turbulence parameters (for turbulent calculations in case of backflow)

Pressure outlet boundary conditions require the specification of a static (gauge) pressure at the outlet boundary. The value of static pressure specified is used only while the flow is subsonic. Should the flow become locally supersonic, the specified pressure is no longer used; pressure will be extrapolated from the flow in the interior. All other flow quantities are extrapolated from the interior [13].

The inlet, inject and outlet boundary conditions with corresponding turbulence conditions are calculated using MathCad® as in Figures C-1 to C-5 in Appendix C.

3.2. Computational Grid

Mesh generation is accomplished by a sequence of processes; Fig. 3-3 summarizes the flow chart of this series of processes done by AutoCad®, GAMBIT®, and TGRID® respectively. The nozzle geometry is created by AutoCad® then exported to GAMBIT®. In GAMBIT®, unstructured surface mesh is generated over whole geometry using size functions to sustain smooth transition from regions of high density grid to low density grid parts like from the proximity of injection port to unaffected region, moreover boundary types are defined on surfaces, and afterwards the mesh file is formed and it is exported to TGRID®. In TGRID®, boundary layer (BL) grid is generated by extruding the surface mesh as prisms and then the rest of the domain is filled with unstructured grid on top of BL grid to reduce the overall mesh size yet still providing enough accuracy. Finally it is exported to FLUENT® ready for simulation. Fig. 3-4 shows the computational grid created using this procedure; it includes about 750,000 hybrid cells both structured and unstructured for the half geometry (Mesh5). Special attention has been given to physics of the problem obviously, the diverging section of the nozzle especially in the neighborhood of injection port along the nozzle wall is finely clustered and for the boundary layer grid the first cell centroid is placed according to the near wall treatment chosen.

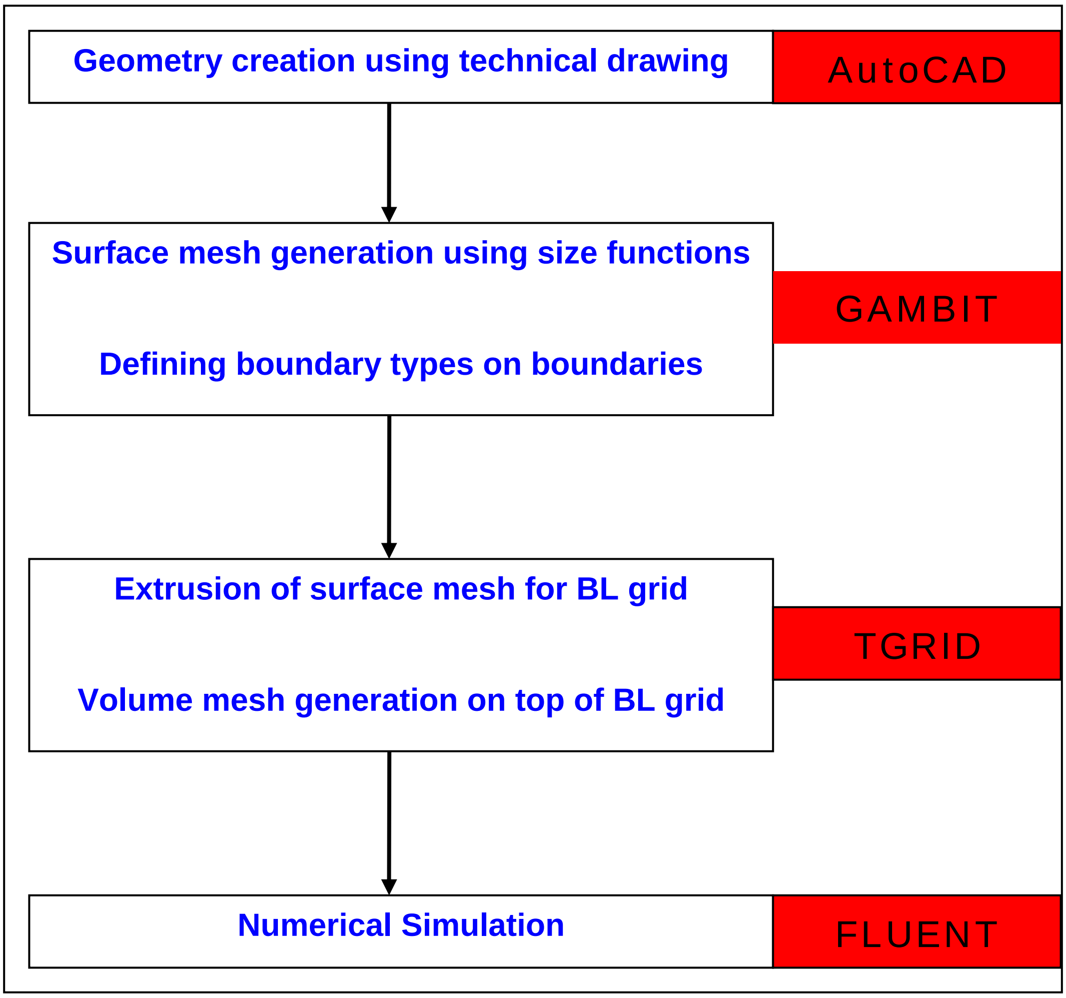

Figure 3-3 Grid generation flow chart

As mentioned earlier two different wall treatment approaches has been tested, wall functions and enhanced wall treatment. In wall functions approach viscosity affected inner region (viscous sublayer and buffer layer) is not resolved instead the wall is bridged to fully turbulent region (log-layer and beyond) on the other hand in the enhanced wall treatment approach all the way to the wall is resolved with a fine mesh [17].

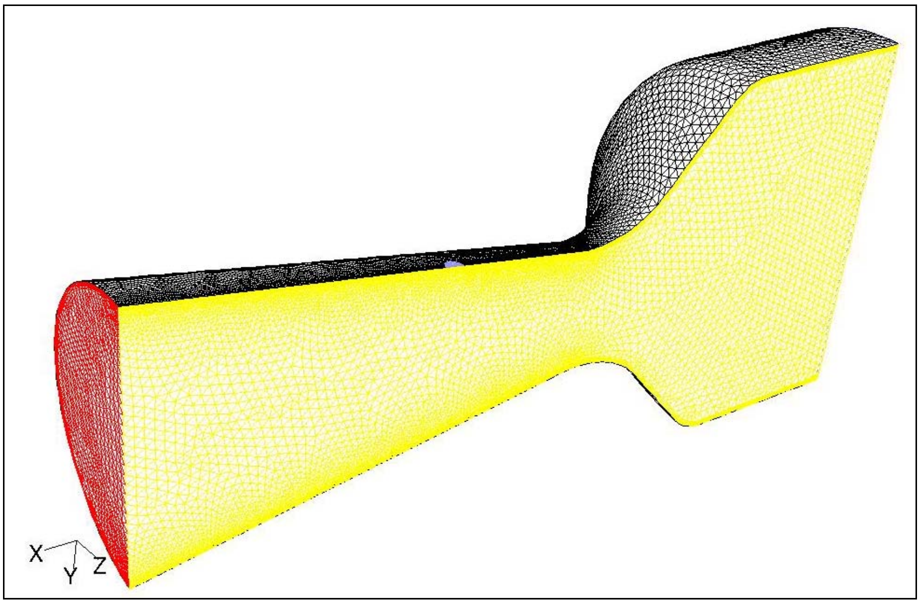

Figure 3-4 Computational grid (Mesh5)

Although the use of wall functions is economical in computation point of view, the major drawback is that these functions behave poorly in the cases of flows with strong pressure gradients leading to separations, non-equilibrium conditions (when production of turbulence is not equal to dissipation), low Reynolds number effects, high three dimensionality and transpiration from the wall [17]. On the contrary enhanced wall treatment resolves the turbulent phenomena better in above cases and especially when shockwaves do interact with boundary layers and impose strong pressure gradients on them. Specifically for turbulent boundary layers the interaction is quite strong and less diffusive compared to laminar boundary layers [21, 22]. However the main disadvantage of this approach is that it is computationally demanding (it requires a grid with $y^+ \approx 1$; whereas wall functions require $y^+ \approx 30$). The first grid spacing estimation is estimated using skin friction coefficient (*Cf*) as in Eq. 3-4 for pipe flows [22, 23].

$$Cf/2 \approx 0.046 \cdot \mathrm{Re}_x^{-0.2} \tag{3-4}$$

Note that x is the distance from the inlet to injection port, in front of which boundary layer separates, and using the definitions of y^+ and U_τ the first cell distance is estimated for both approaches as shown in Fig. 3-5.

Yplus on the Wall Estimation (Pipe Flow):

$$x := 100mm \qquad yplus1 := 1$$

$$Rex := \frac{U \cdot x}{\nu} \qquad y := \frac{yplus1 \cdot \nu}{U \cdot \sqrt{0.046 Rex^{-0.2}}} \qquad y = 5.856 \times 10^{-7} m$$

$$Rex = 3.603 \times 10^{6}$$

Figure 3-5 y^+ estimation on the wall using pipe flow approach

3.3. Results and Discussion

In this part of the study three computational grids of 510262 hybrid cells with non-equilibrium wall function approach (Mesh4), 748346 hybrid cells with enhanced wall treatment approach (Mesh5) and 622640 fully structured cells with non-equilibrium wall function approach (Mesh6), as shown in Table 3-1, are generated. The grid resolutions of these three meshes on the symmetry planes are shown in Fig. 3-6. In essence these meshes are not independent of each other, Mesh4 and Mesh 5 share the same surface mesh but they have different boundary layer meshes obviously, and Mesh4 and Mesh6 share the same boundary layer mesh in terms of first cell height, expansion ratio and total number of cells but they have different mesh types. And for the total boundary layer grid, a height of 1.3mm (10% of throat radius) is used appropriately in high Reynolds number flows and it ensures good mesh quality in terms of skewness of the boundary layer cells by enabling a gradual ascent of these cells along BL. Estimated y^+ value is checked with numerical simulations and validated as shown in contour plots for Mesh5 and Mesh6 in Figures 3-7 and 3-8. The y^+ contour for Mesh6 is not shown since it has the same boundary layer (BL) grid with Mesh4, hence similar values of y^+ are obtained.

Table 3-1 Computational grid specifications

Mesh ID	**Mesh 4**	**Mesh 5**	**Mesh 6**
Mesh Type	Hybrid	Hybrid	Structured
# of Cells	510262	748346	622640
# of Nodes	192171	317220	643878
Wall treatment	Non-equilibrium wall functions	Enhanced wall treatment	Non-equilibrium wall functions
BL grid height (mm)	1.3	1.3	1.3
BL grid first cell height (mm)	0.018	0.0006	0.018
# of cells in BL grid	15	28	13

In essence by comparing Mesh4 and Mesh5 the effect of wall treatment is addressed on the other hand the comparison between Mesh4 and Mesh6 assesses the suitable mesh type for this problem. For the turbulence models Spalart-Allmaras (SA), Rke, Renormalization Group k-ε (RNG), standard k-ω and shear stress transport k-ω (SST) are tested also together with an Euler solution. Finally for the solver types two different solver types are compared; segregated implicit and coupled explicit solvers.

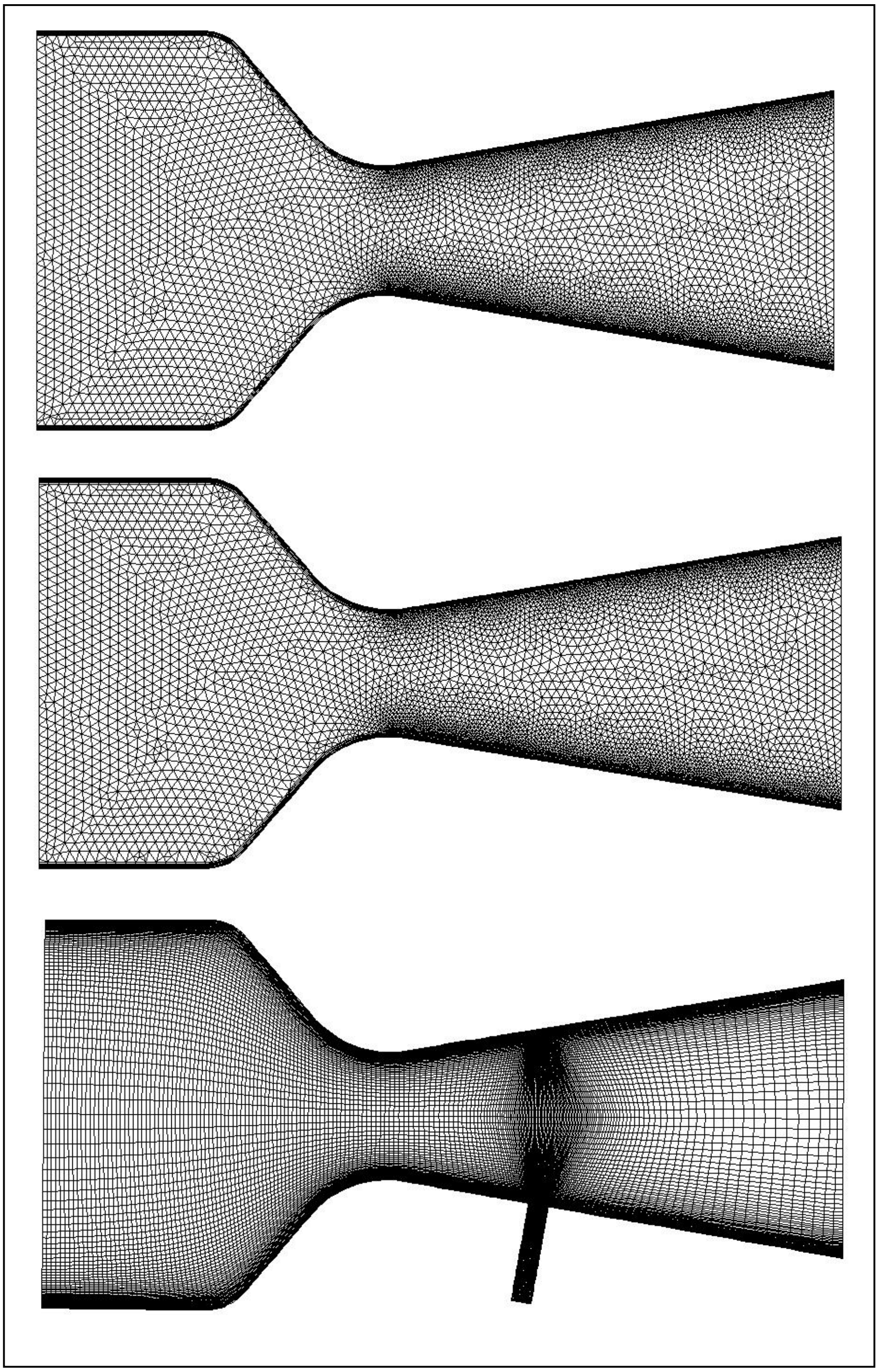

Figure 3-6 The grids on the symmetry planes corresponding to Mesh4, Mesh5 and Mesh6

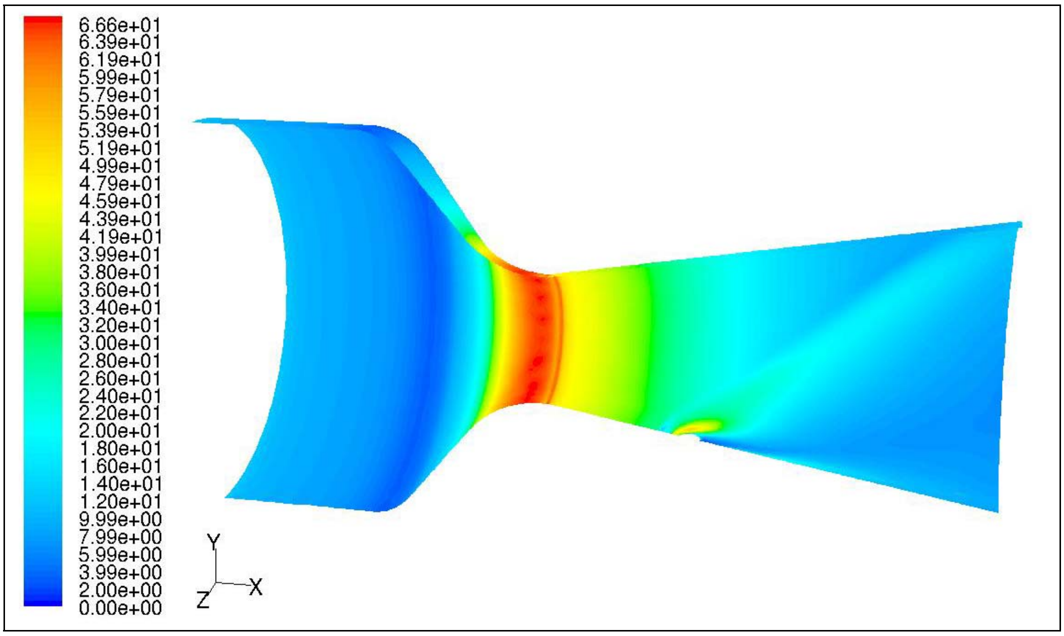

Figure 3-7 y^+ contours for Mesh4 (with rke turbulence model)

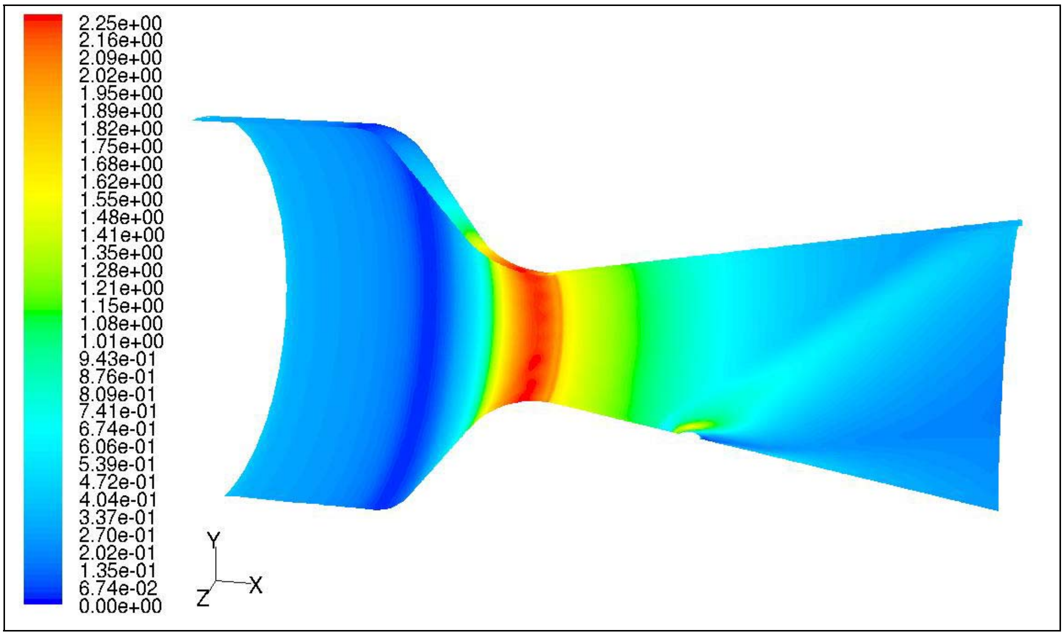

Figure 3-8 y^+ contours for Mesh5 (with rke turbulence model)

The quantitative comparison of these simulations with experimental data [8] on the symmetry line at an axial distance of *50mm* and *70mm* from nozzle throat is shown in Figures 3-9 to 3-12 and Figures 3-13 to 3-16 respectively. Four plots are drawn for each axial location, the first one is overall comparison, second one is turbulence model evaluation (all have the same Mesh4 except for Euler simulation, which has the same surface mesh with Mesh4 but it does not have any boundary layer mesh, of course), third one yields mesh size and type evaluation and the last one is solver type comparison. Note that the vertical distance has been non-dimensionalized by injection orifice diameter, and the legends without mesh numbers refer to Mesh4.

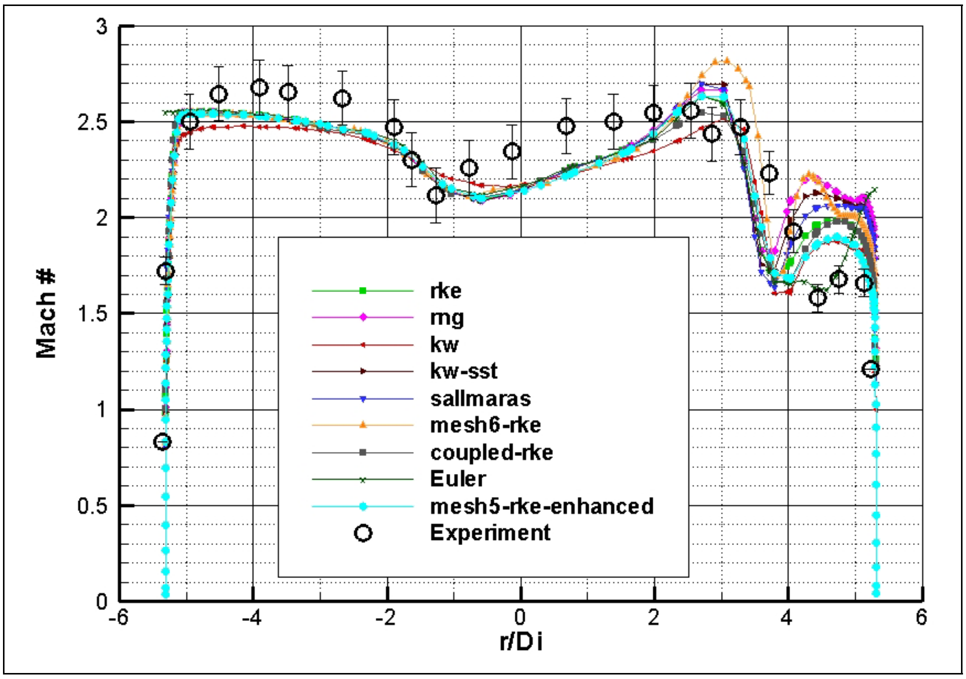

Figure 3-9 Overall comparison of Mach number profile at x=50mm with measured data

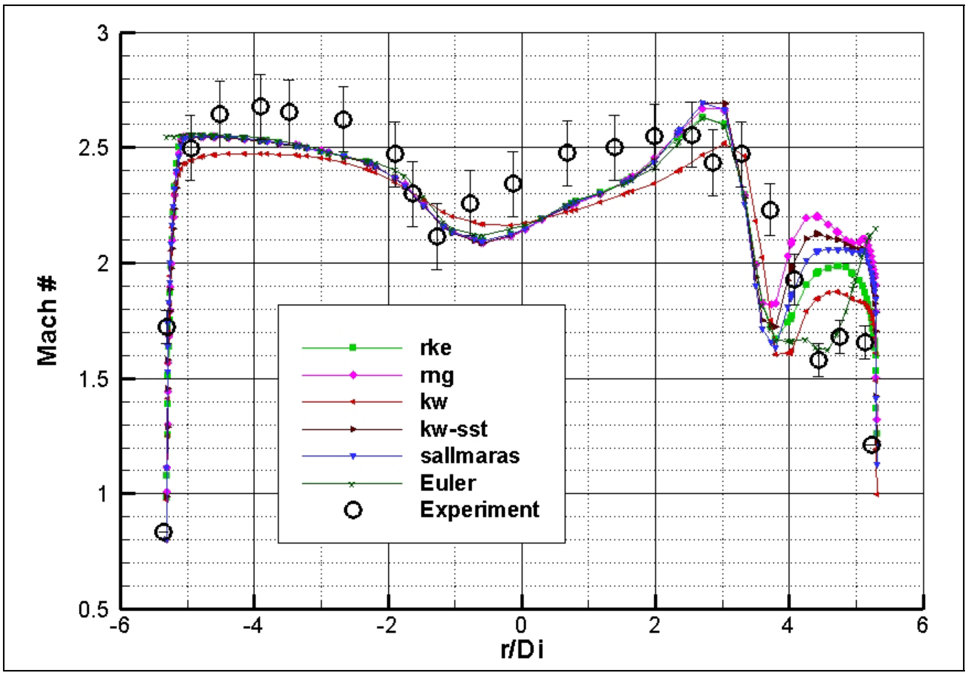

Figure 3-10 Comparison of Mach number profile at x=50mm with measured data -Turbulence model

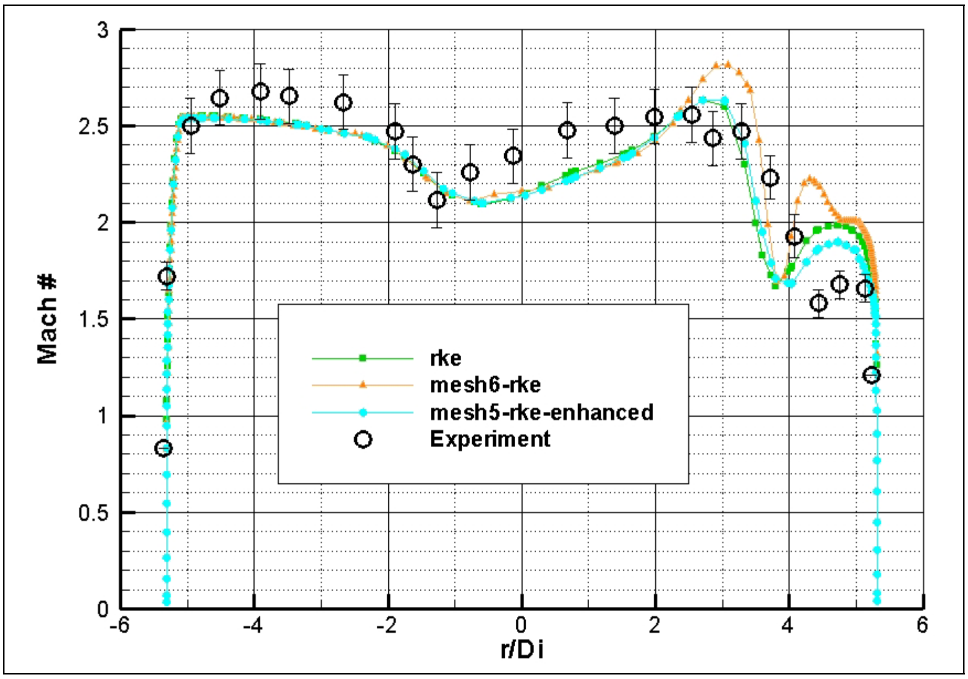

Figure 3-11 Comparison of Mach number profile at x=50mm with measured data - Mesh size

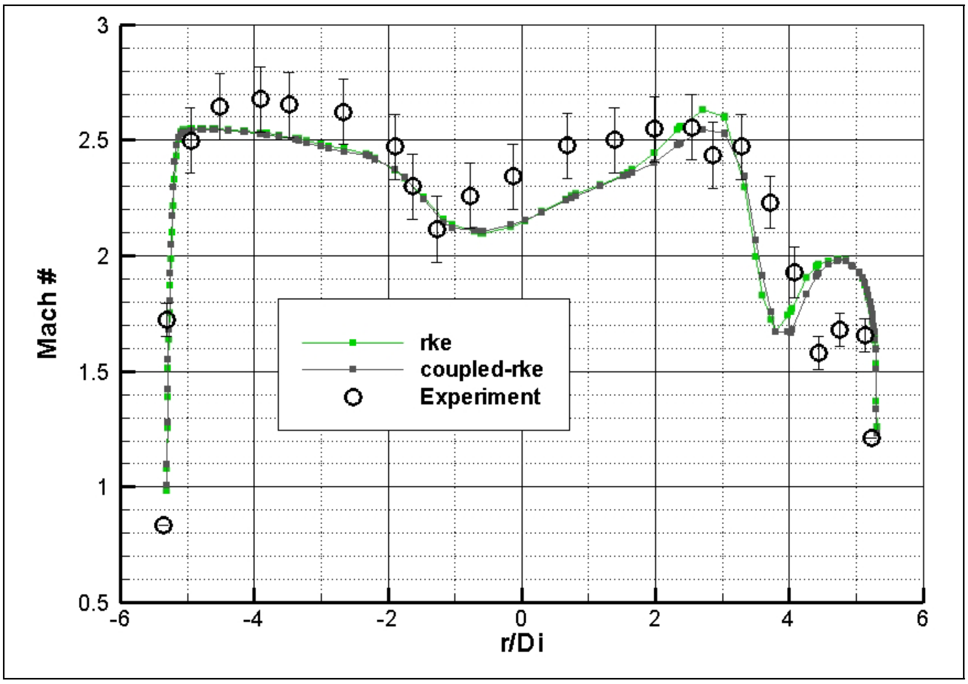

Figure 3-12 Comparison of Mach number profile at x=50mm with measured data - Solver type

For *x=50mm* plane (see Figures 3-9 to 3-12) along the symmetry line, quantitative comparison of Mach number profile with experimental values reveals;

- Mesh6 overpredicts the experiments under the bow-shock in the recompression region ($3<r/D_i<4$) and secondary jet core region ($4<r/D_i<5$). Mesh4 and Mesh5 show more or less the same trend; however Mesh5 gives the best results closer to experimental values [8], even better than the numerical simulation by Ko [6] in these regions.

- The rke simulation with Mesh5 contains roughly 750,000 cells with enhanced wall treatment approach. It provides accurate resolution of the regions close to the wall and accounts for strong pressure gradients and complex separation phenomenon, which is the case for this problem.

- The discrepancies are considerable both in unaffected region (above the strong bow-shock, $-5<r/D_i<-2$) and under the bow-shock region ($2<r/D_i<5$). The maximum difference in Mach number is 0.3 around the shock, and the reason for that might be the bias in experimental values associated with the intrusive character of the pressure probe inserted in flowfield plus the incapability of turbulence models to resolve fine scales of turbulence together with inherent isotropic eddy viscosity assumption.

- As far as the turbulence models are considered, all models behave similarly in the unaffected region while k-ω is showing a slightly lower trend. They all underpredict slightly, whereas in the recompression and secondary jet core region Rng overpredicts the most, k-ω, k-ω SST, rke and k-ω overpredicts the experimental value in a decreasing order.

- In terms of solver choices, the difference between coupled-explicit solver and segregated solver is negligible, coupled solver performs slightly better, nevertheless segregated solver is robust, converges fast and residuals of continuity, momentum, energy and turbulence drop to levels of 10e-9 in 3000 iterations. Although the problem at hand is a turbulent compressible flow problem and the coupling of energy equation with continuity and momentum is essential [13], the coupled explicit solver does not produce necessarily better results and takes much more time to converge. The segregated solver based pressure-velocity coupling should be used with extra care to ensure numerical stability, for instance the solution limits should be set to meaningful values to prevent unbounded oscillations.

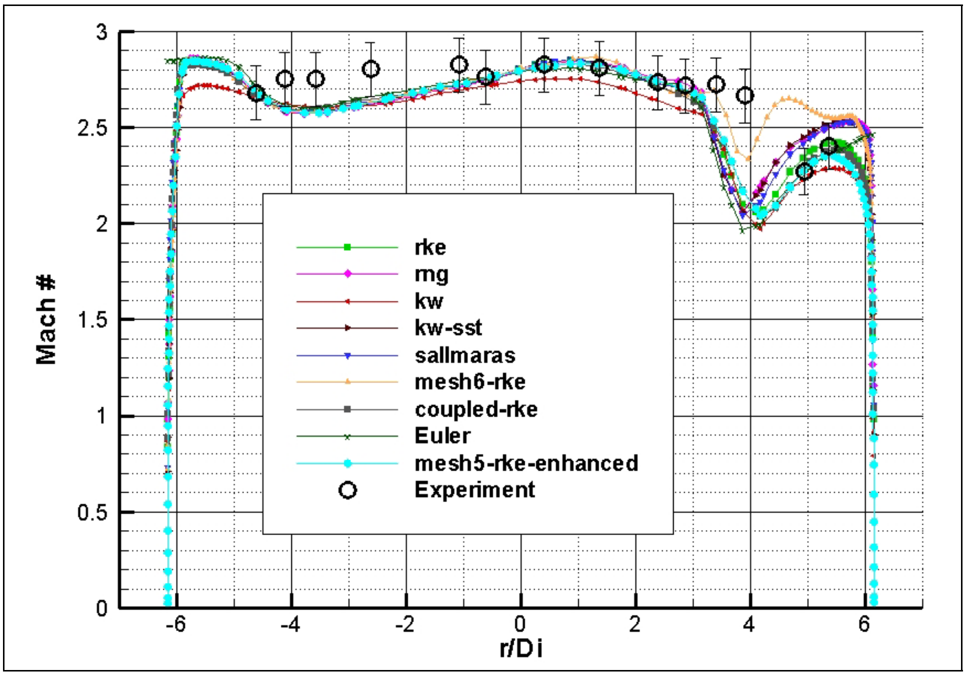

Figure 3-13 Overall comparison of Mach number profile at x=70mm with measured data

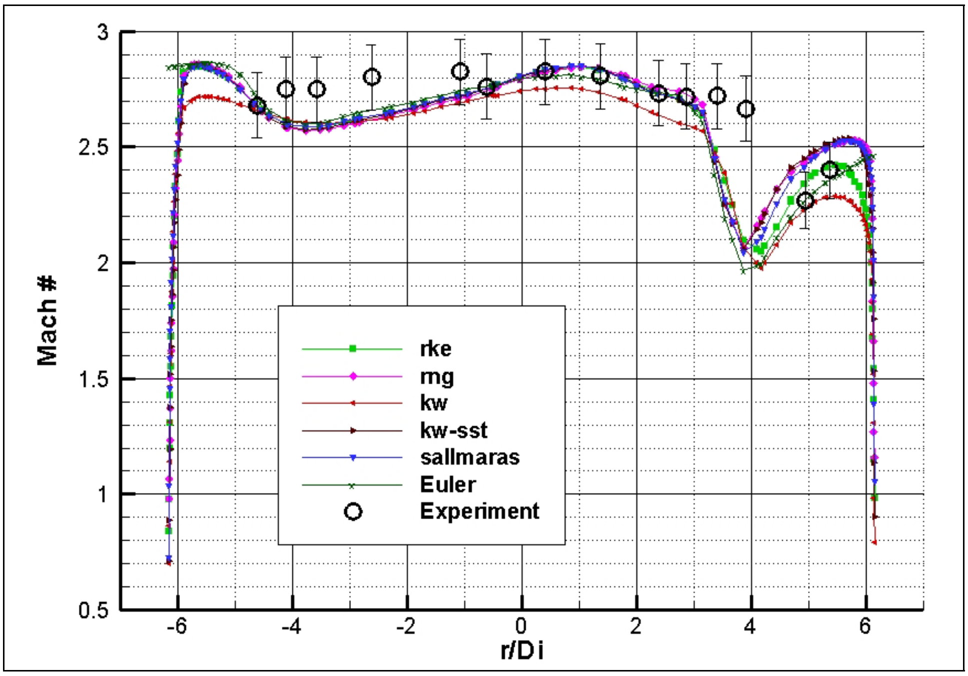

Figure 3-14 Comparison of Mach number profile at x=70mm with measured data -Turbulence model

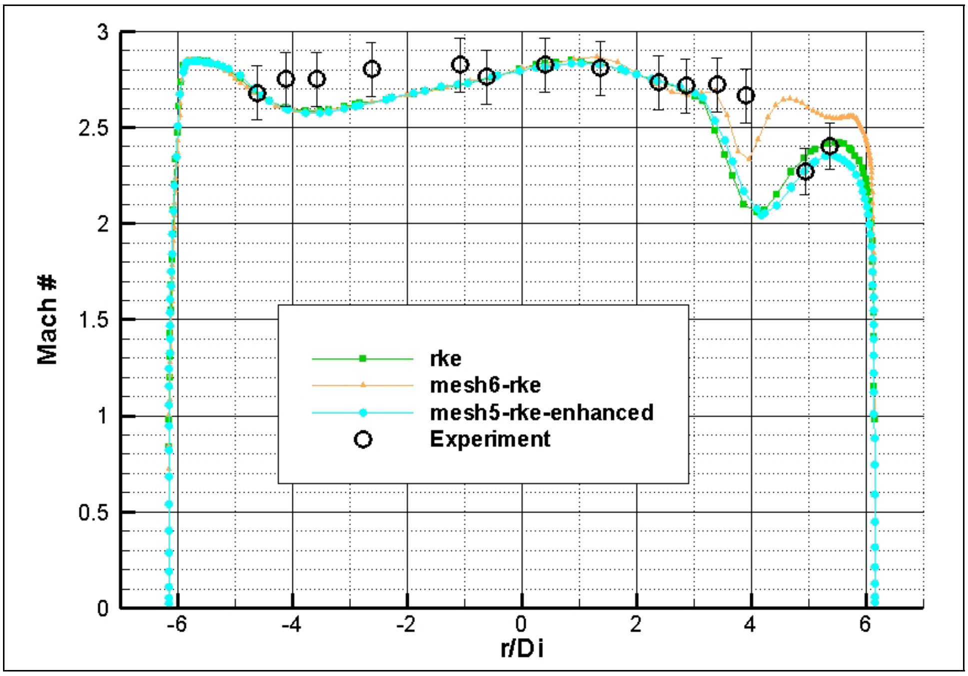

Figure 3-15 Comparison of Mach number profile at x=70mm with measured data - Mesh size

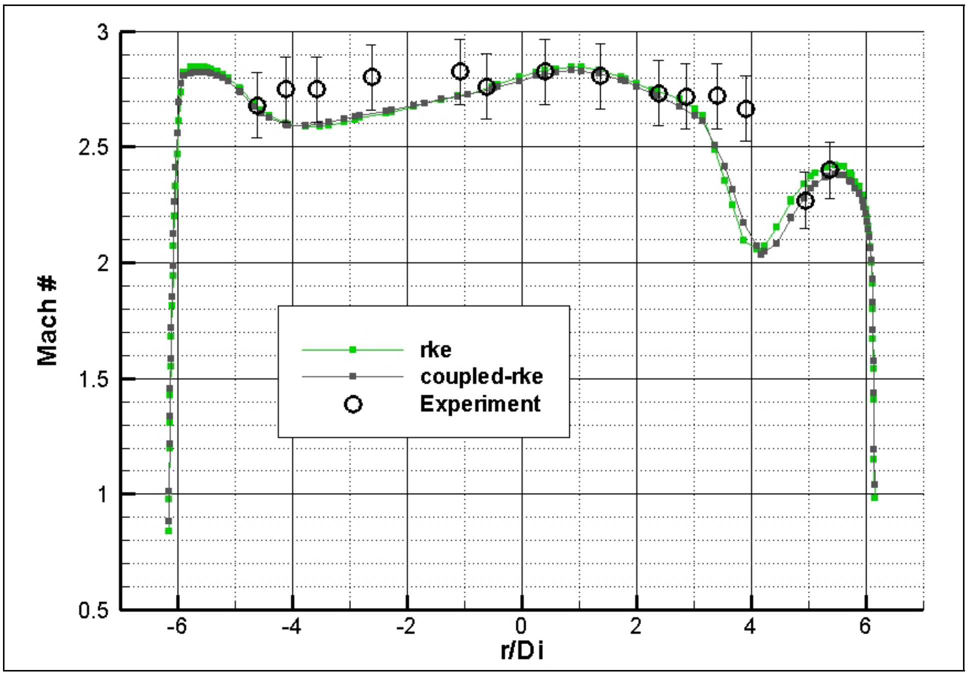

Figure 3-16 Comparison of Mach number profile at x=70mm with measured data - Solver type

For *x=70mm* plane (see Figures 3-13 to 3-16) along the symmetry line, quantitative comparison of Mach number profile with experimental values reveals;

- All computational grids show similar behaviors in fact they are very close to each other, except Mesh6 being overpredictive in both recompression and secondary jet core regions. It is worth to note that as it is gone along the nozzle towards the nozzle exit, the mixing of secondary jet into the primary flow is increased and steep gradients are relaxed, thus the discrepancies are diminished at this *x=70mm* station.

- For the turbulence models, they all behave close to each other; only k-ω shows small deviations from the main trend. Similar to previous station results almost all models follow the same manner above and under the bow-shock up to recompression region. Rng, SA and k-ω SST overpredicts the flow slightly in the core region. Even Euler solution captures most of the flow phenomena and it is close to rke and k-ω. In fact rke is the one closest to the experiments in the core region, however in the recompression region; the agreement is not very satisfactory due to the reasons explained above, as in case of numerical simulations by Ko [8].

- In terms of solver selection the segregated solver seems to be the most feasible option and the differences with coupled solver is negligible.

The qualitative comparison of simulations for these solution parameters with experimental data on the nozzle exit plane is shown in Figures 3-17 to 3-20.

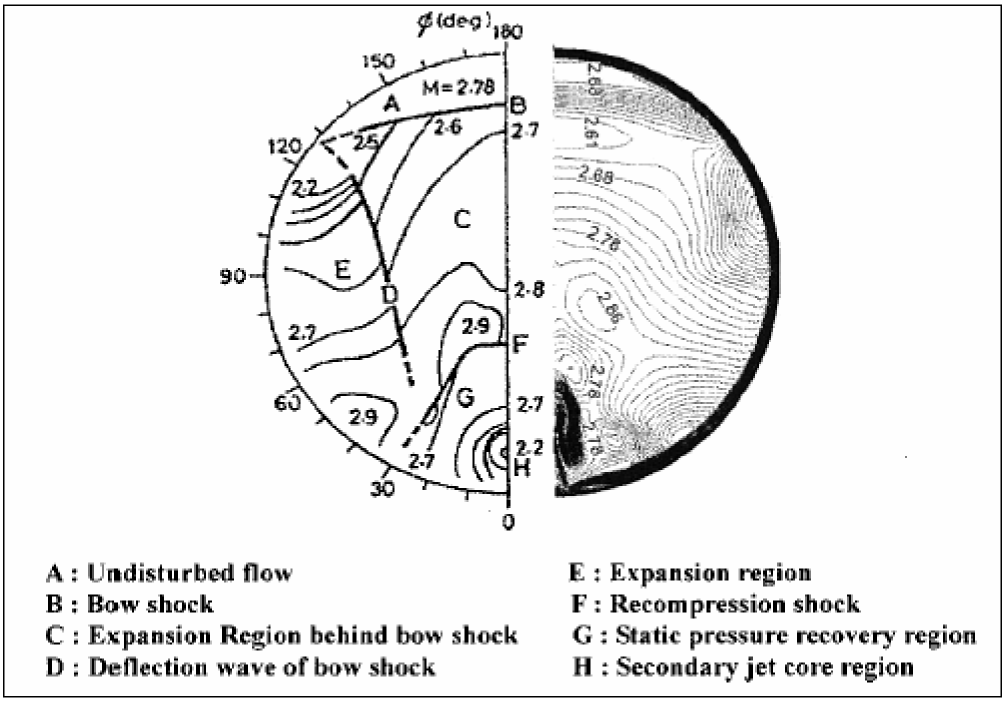

Figure 3-17 Mach number contours at exit plane measured by [8] (left) and computed by [6] (right)

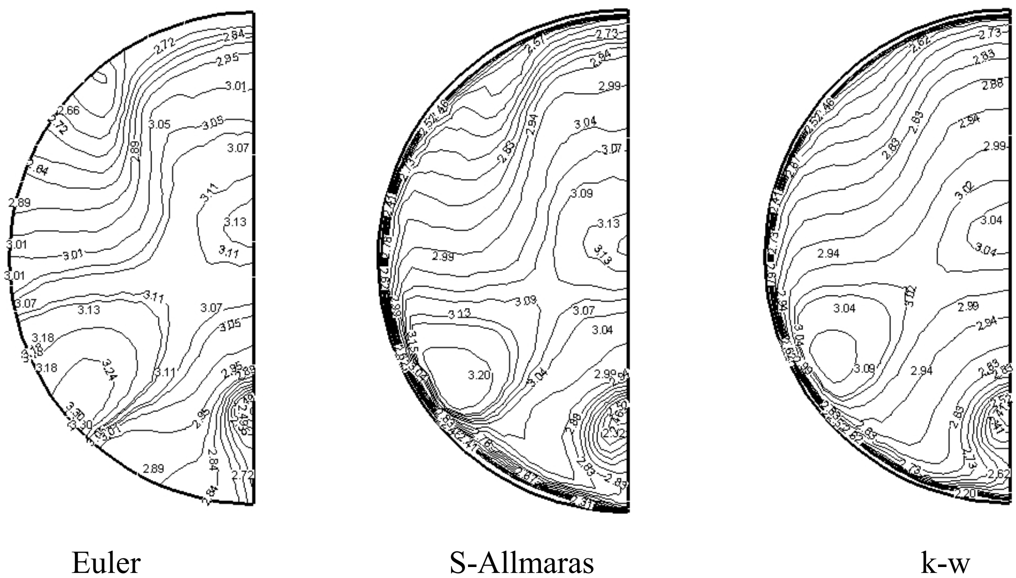

Figure 3-18 Mach number contours at exit plane Euler, S-Allmaras and k-w

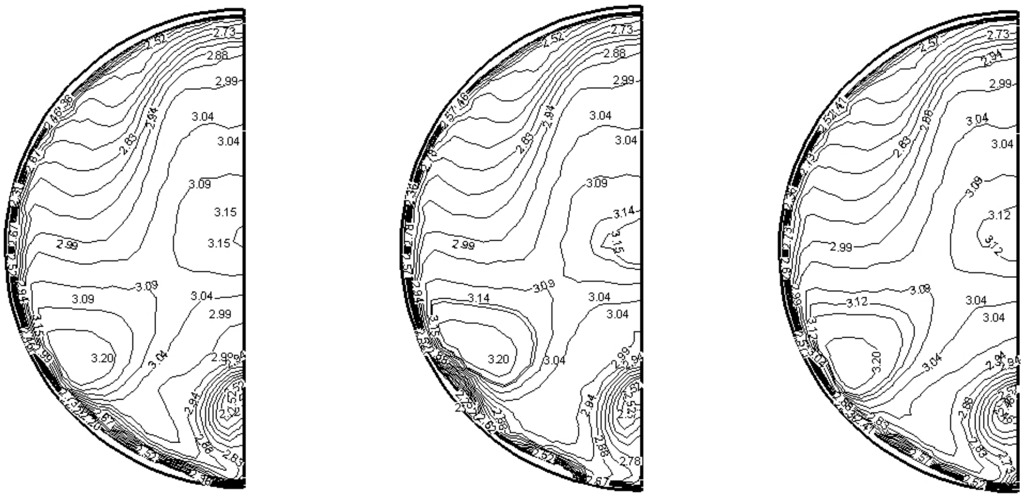

k-w SST Rng Rke

Figure 3-19 Mach number contours at exit plane k-w SST, Rng and Rke

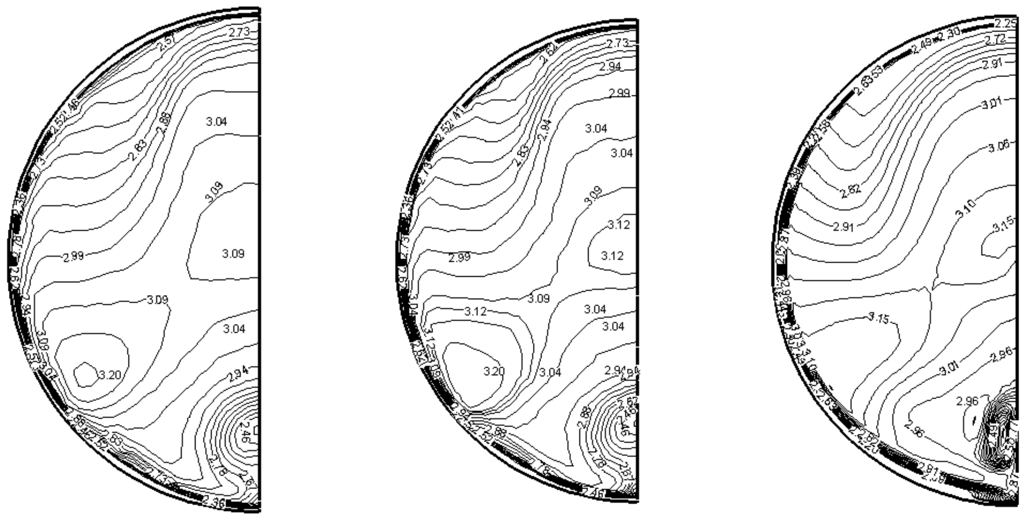

Cp-rke Enh-rke Structured-Rke

Figure 3-20 Mach number contours at exit plane Coupled Rke, Enhanced Rke and Structured Rke

For exit plane (see Figures 3-17 to 3-20), qualitative comparison of Mach number contours with both experiments and numerical simulations yields;

- The overall flow structures for all cases are similar to each other, however the flowfield is slightly overpredicted in all cases, especially in expansion region (denoted by E) behind the reflected shock wave up to recompression region (denoted by E).

- Secondary jet core region (denoted by H) and static pressure recovery region (denoted by G) are captured in all cases. However, the strong bow-shock is reflected from the opposite wall at the very end part of the nozzle contrary to experiments, therefore the internal flow structure is altered slightly resulting higher values of Mach number.

The qualitative comparison of simulations for these solution parameters with experimental data at a plane of *x=50mm* from the nozzle throat is shown in Figures 3-21 to 3-24.

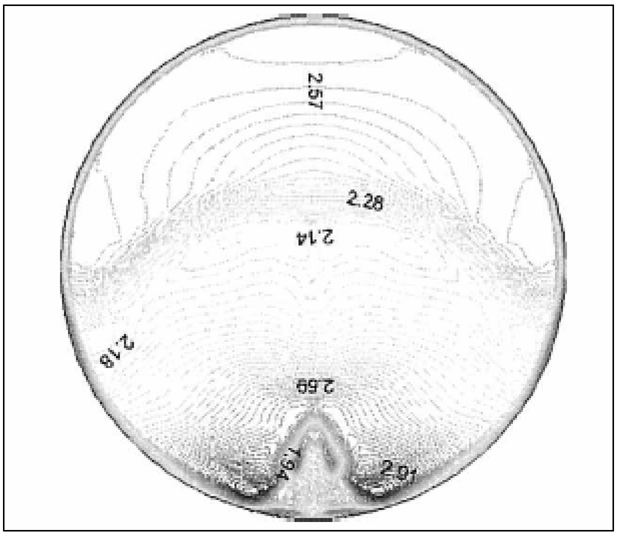

Figure 3-21 Mach number contours at a plane of x=50mm computed by [6]

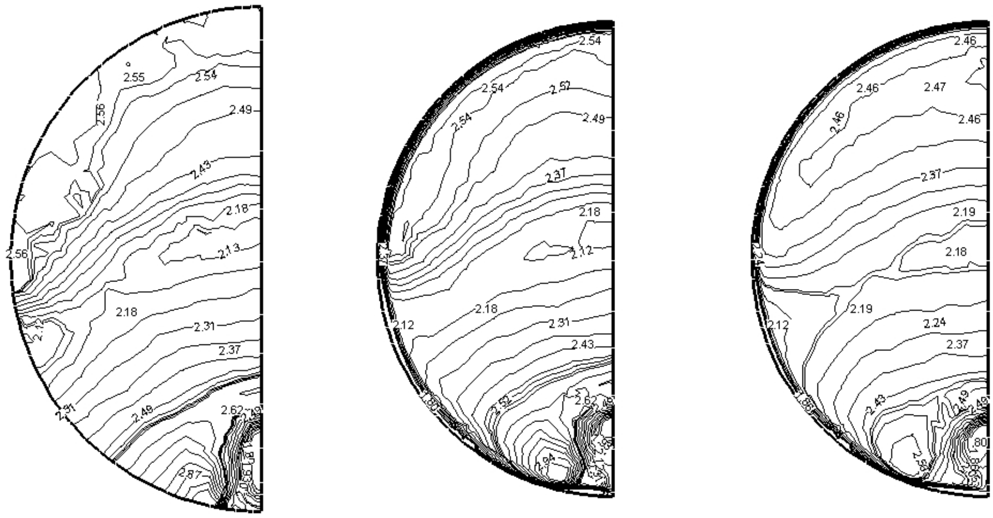

Euler S-Allmaras k-w

Figure 3-22 Mach number contours at a plane of x=50mm exit plane; Euler, S-Allmaras and k-w

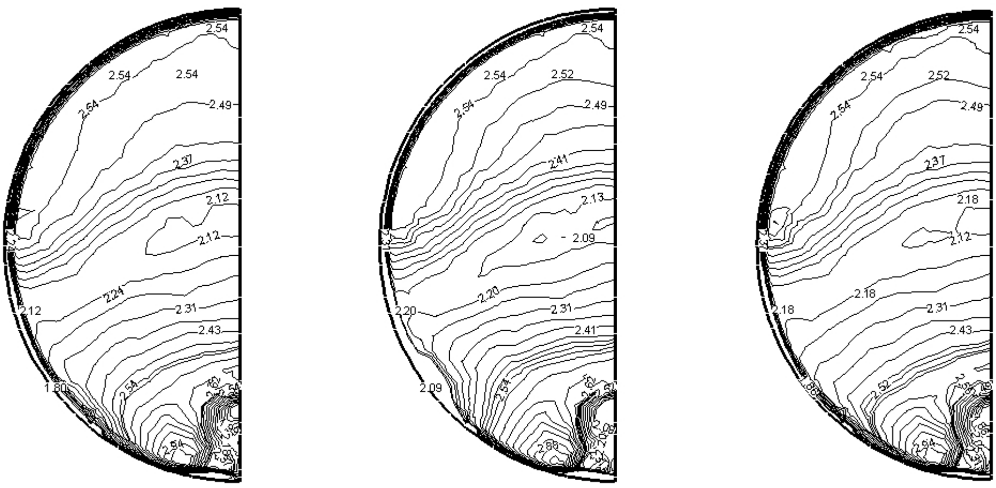

k-w SST Rng Rke

Figure 3-23 Mach number contours at a plane of x=50mm; k-w SST, Rng and Rke

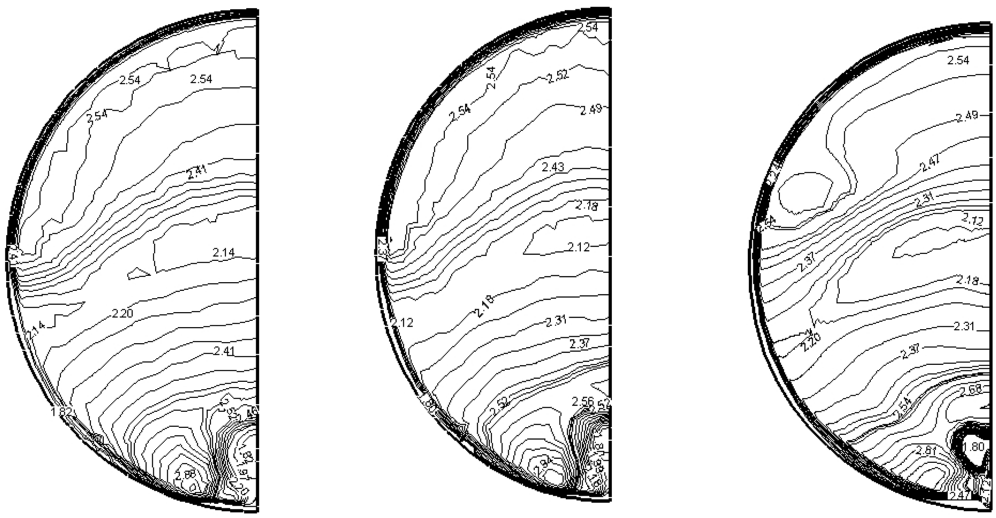

Cp-rke Enh-rke Struc-Rke

Figure 3-24 Mach number contours at a plane of x=50mm; Coupled Rke, Enhanced Rke and Structured Rke

For *x=50mm* exit plane (see Figures 3-20 to 3-24), qualitative comparison of Mach number contours with both experiments and numerical simulations yields that overall flow structures for all cases are similar to each other and agrees well with numerical flow pattern by Ko [6]. The contour values are quite close to numerical values, secondary jet core region and strong bow shock are captured in all cases.

The qualitative comparison of simulations for these solution parameters at symmetry plane is shown in Figures 3-25 to 3-33. It can be easily observed from the figures that the overall contour plots of velocity do not satisfactorily indicate discrepancies between different cases; as a matter of fact all cases look quite alike in terms of overall contour plots. Therefore general plots are not used for a decisive evaluation instead close up plots of velocity focused on the injection port with streamtraces drawn in the proximity accompanied by grid resolution has been used. Afterwards flow structures are compared within each other; note that the contour variable is velocity in m/s.

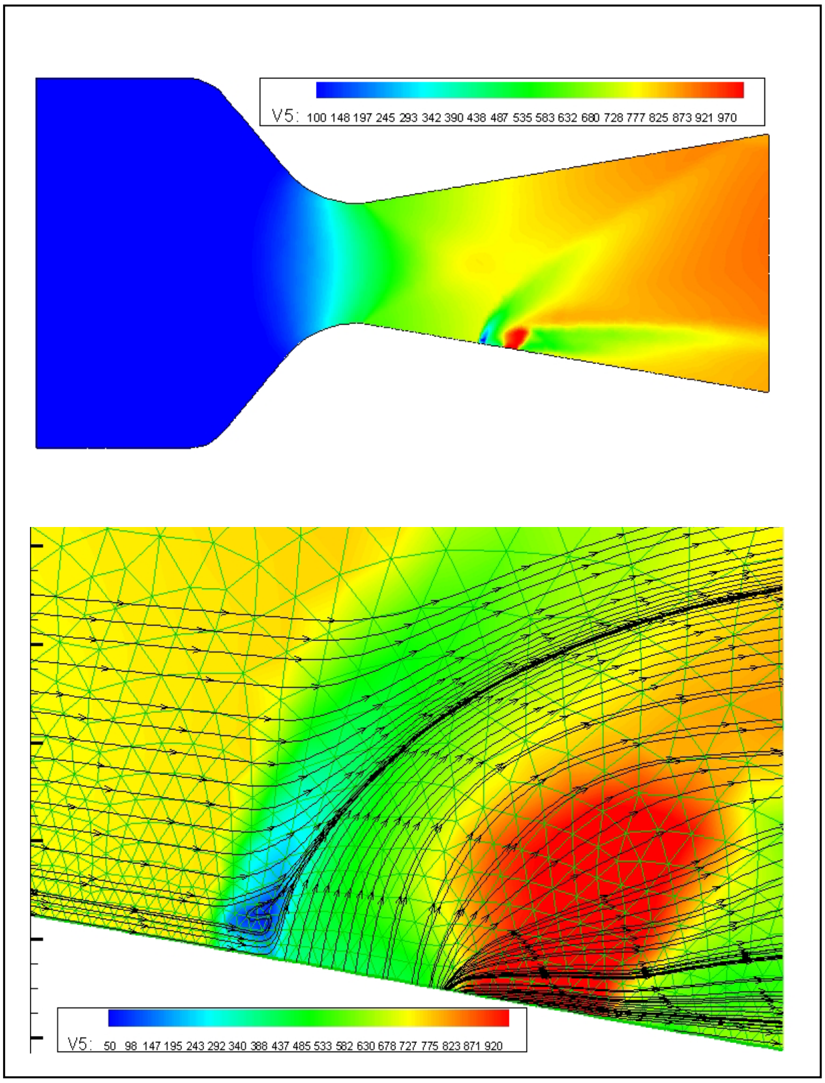

Figure 3-25 Contours of velocity magnitude at symmetry plane with Mesh4; Euler case

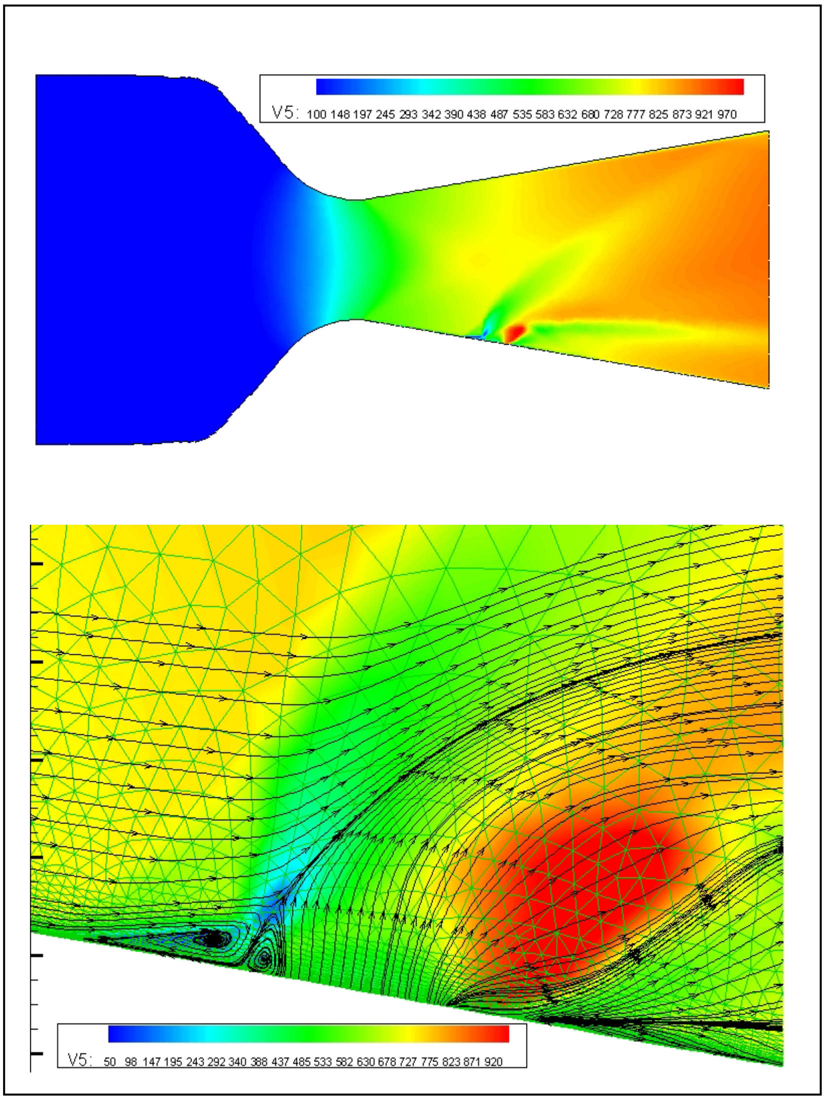

Figure 3-26 Contours of velocity magnitude at symmetry plane with Mesh4; S-A case

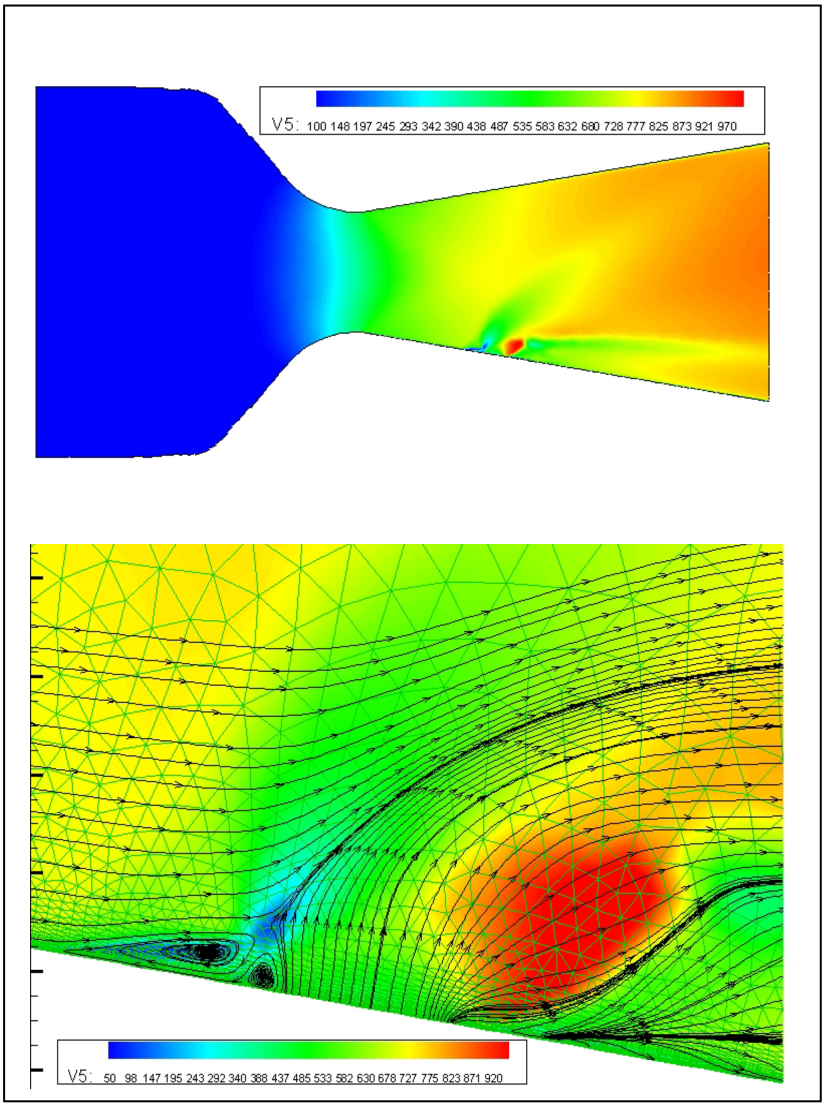

Figure 3-27 Contours of velocity magnitude at symmetry plane with Mesh4; k-w case

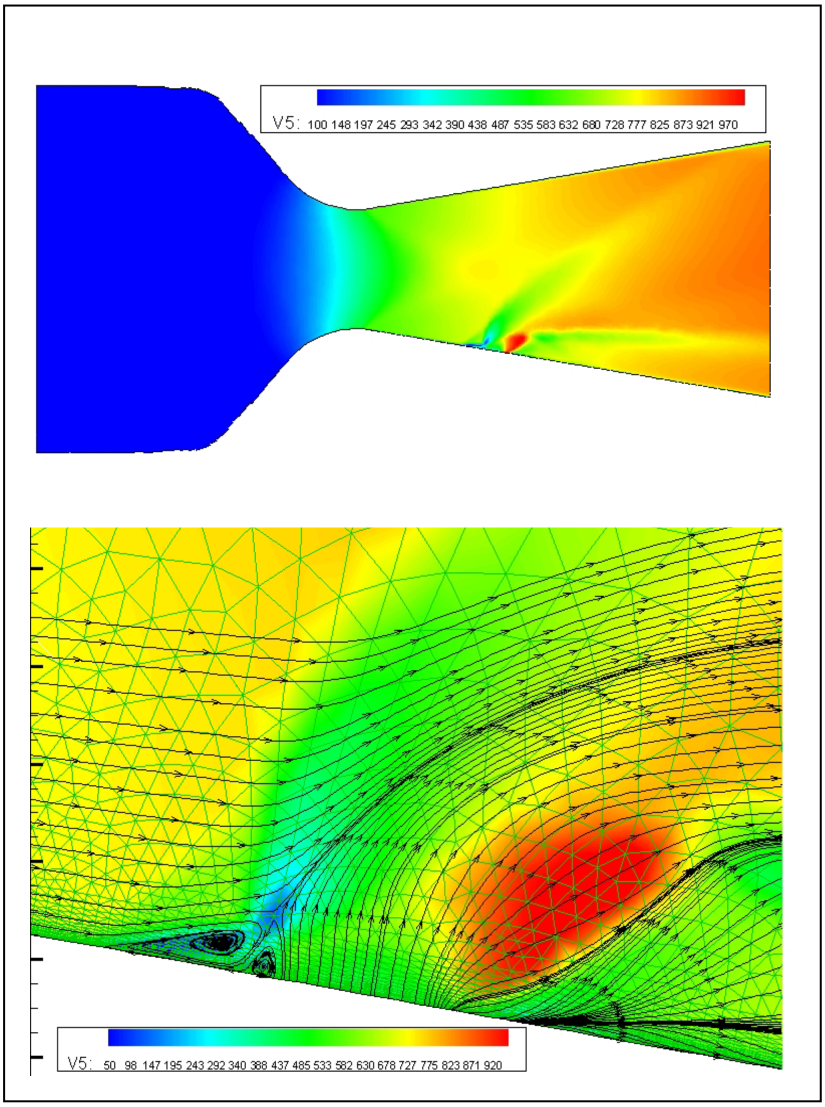

Figure 3-28 Contours of velocity magnitude at symmetry plane with Mesh4; kw SST case

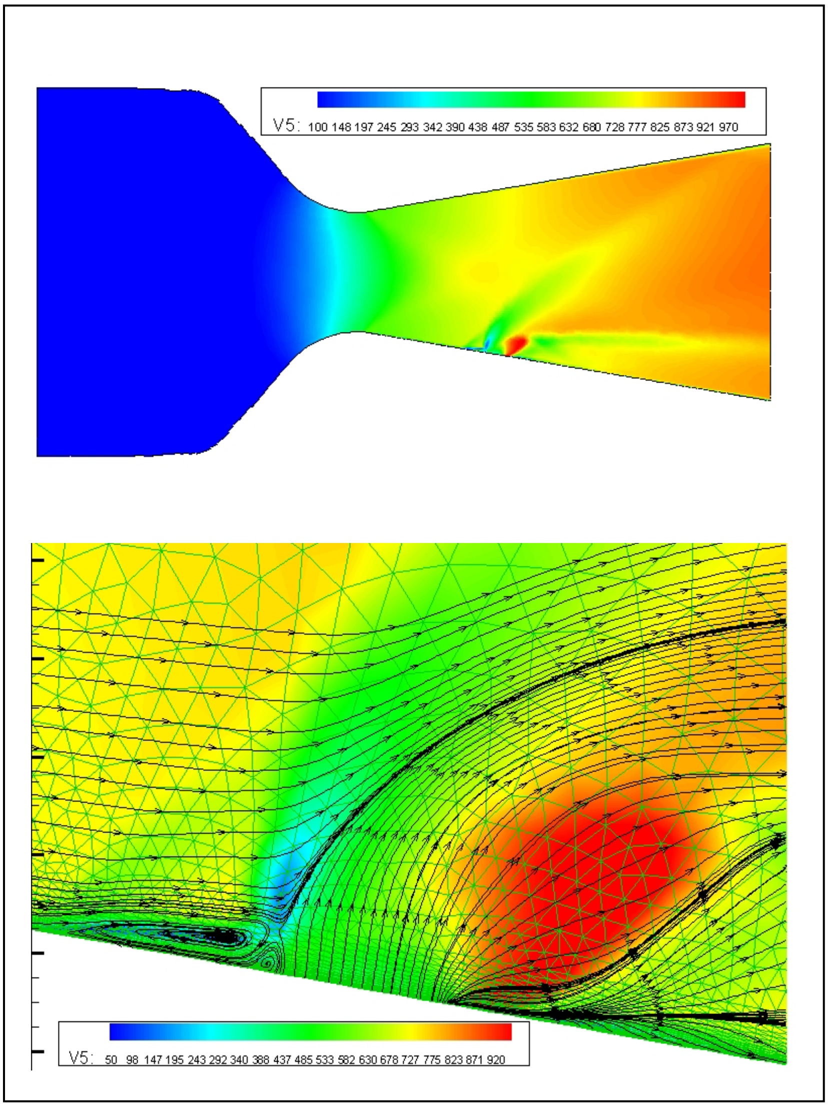

Figure 3-29 Contours of velocity magnitude at symmetry plane with Mesh4; Rng case

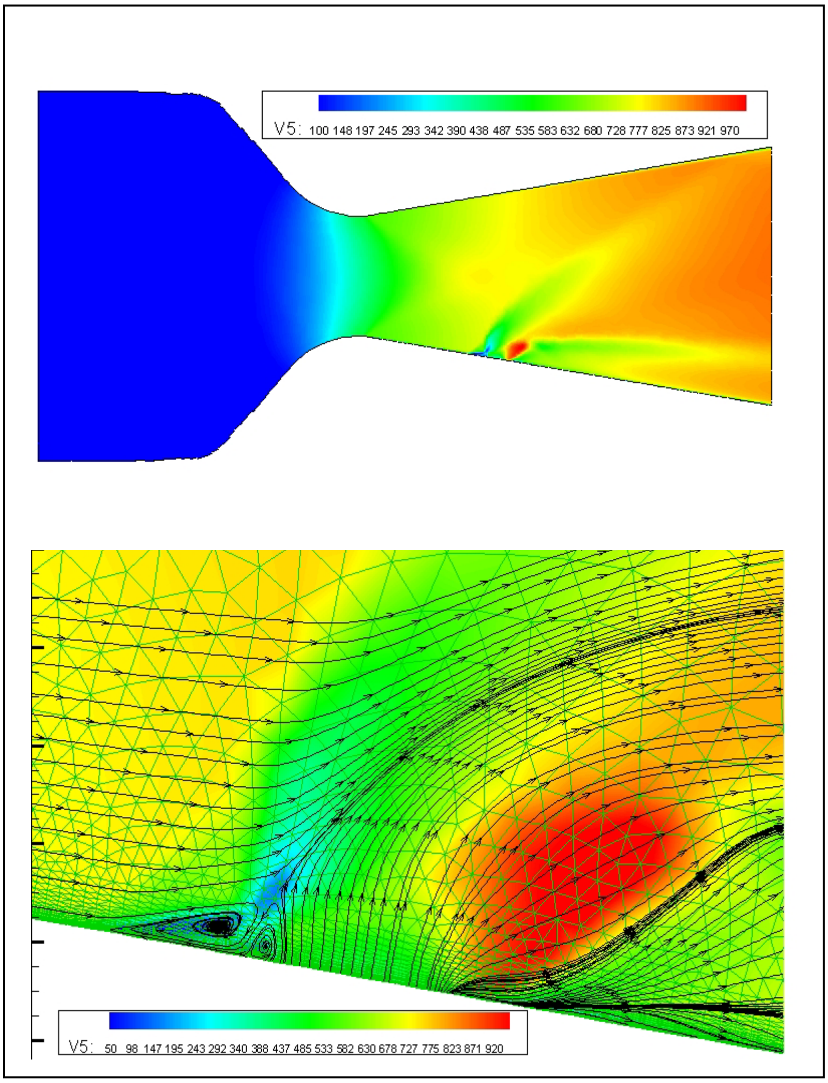

Figure 3-30 Contours of velocity magnitude at symmetry plane with Mesh4; Rke case

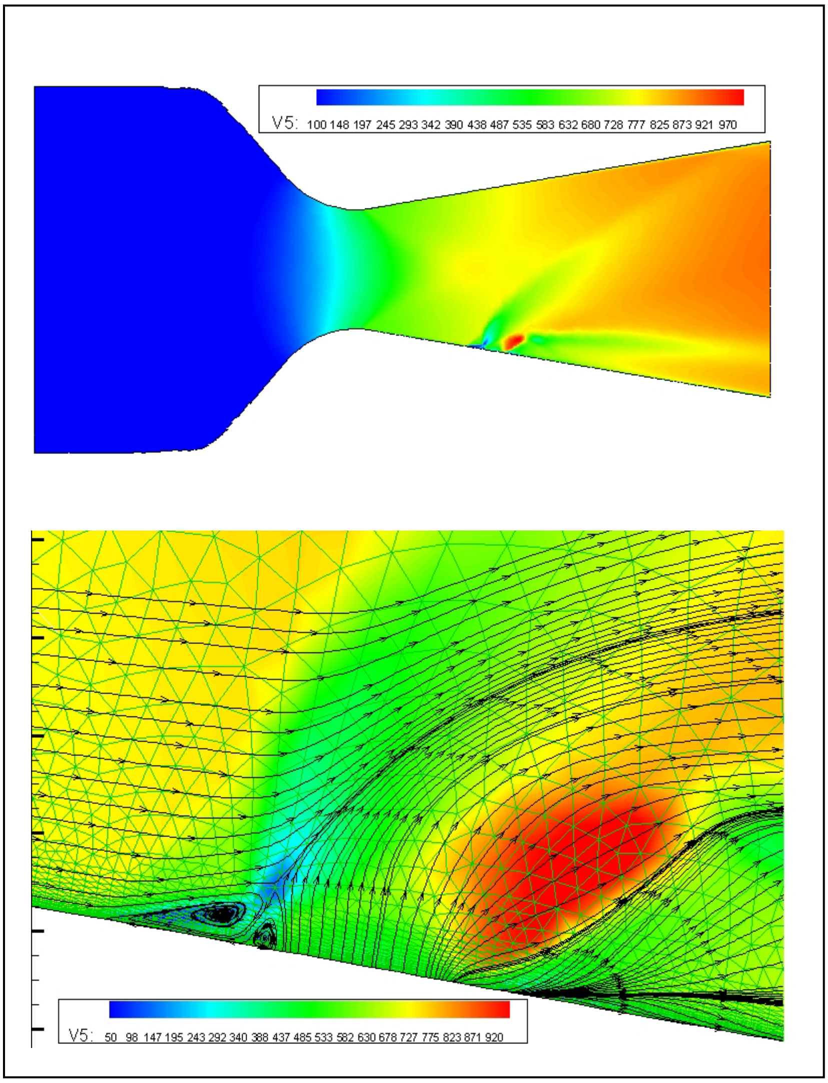

Figure 3-31 Contours of velocity magnitude at symmetry plane with Mesh4; Cp-rke case

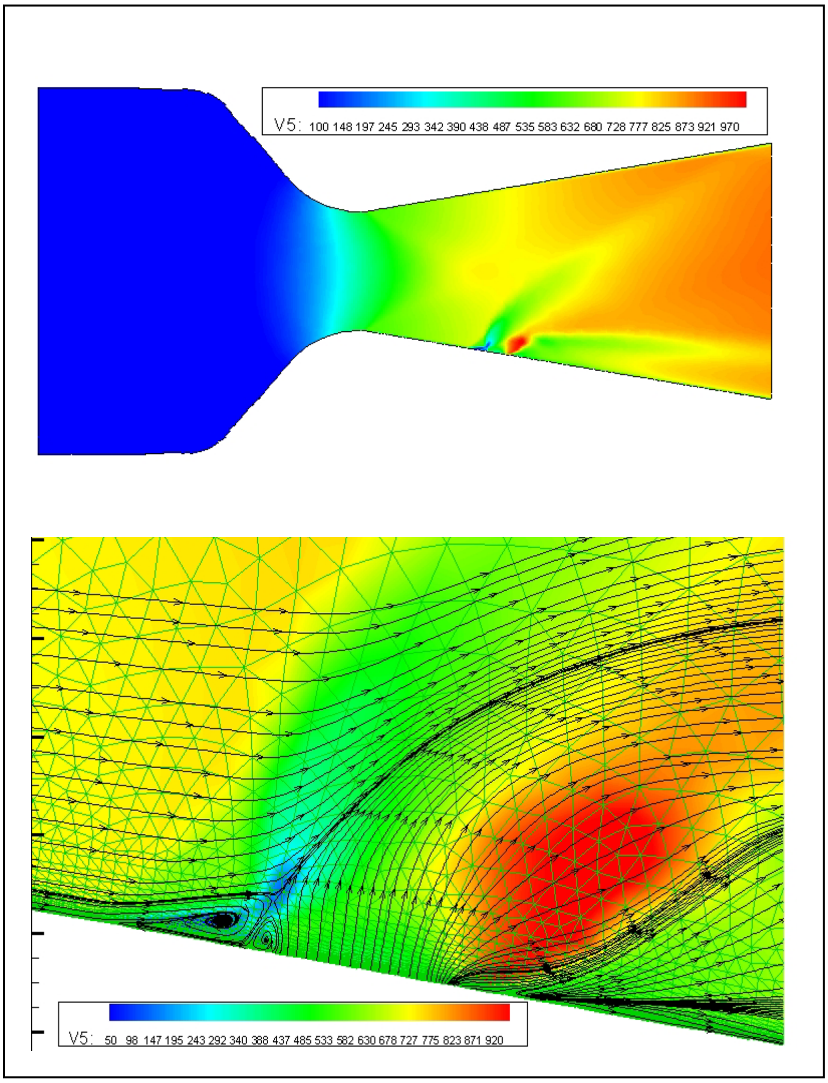

Figure 3-32 Contours of velocity magnitude at symmetry plane with Mesh5; Enh-rke case

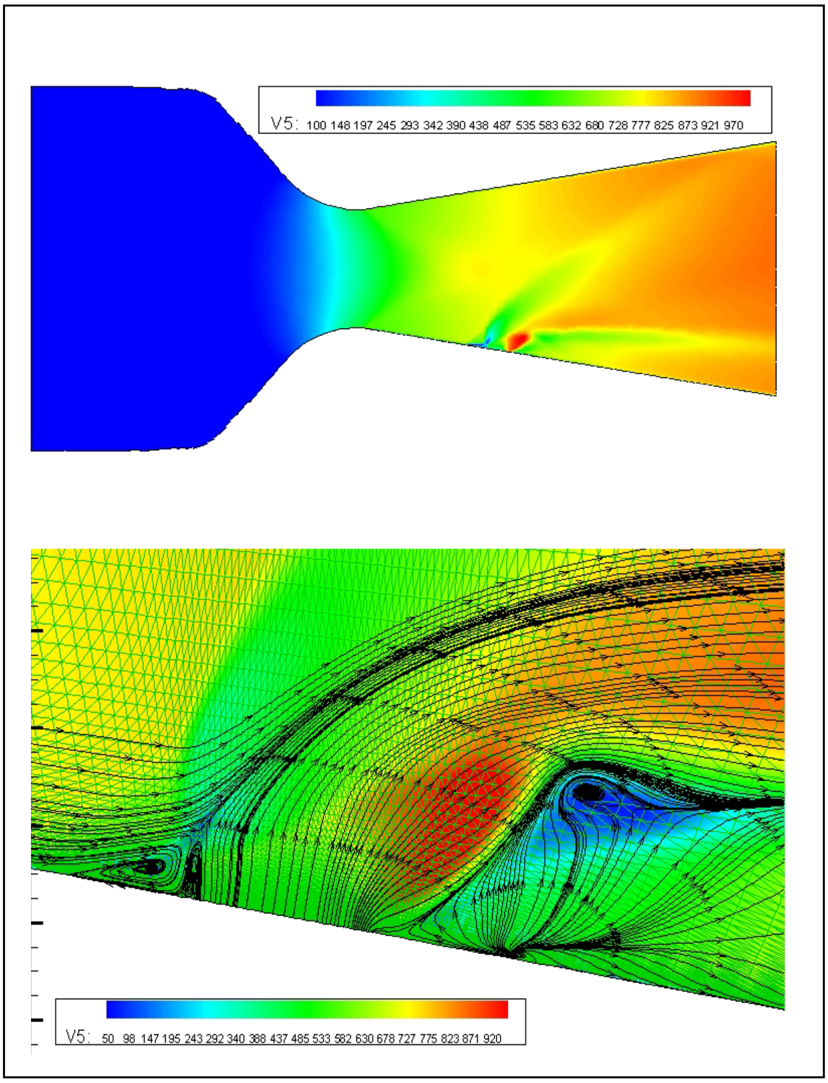

Figure 3-33 Contours of velocity magnitude at symmetry plane with Mesh6; Struc-rke case

For injection port vicinity, (see Figures 3-25 to 3-33), qualitative comparison of velocity contours of numerical simulations in terms of flow structures yields;

- None of the upstream circulating zones are captured in Euler simulation different from all other cases; and the Mach disk (sudden expansion region) is larger than the ones in other cases leaning to wall just downstream of the injection port. Another thing to note is that the bow shock is quite steep down to the wall and not smeared. Obviously it is not interacted with upcoming turbulent boundary layer that is separated.

- In SA, all k-ω and k-ε cases upstream circulating regions are captured, however the size of the regions varies from one simulation to other. In SA, k-ω, k-ω SST and Rng cases circulation zones are bigger whereas in Rke cases they are smaller, especially in Struc-Rke they have the smallest size. In terms of Mach disc all simulations except Euler reveal more or less the same size of structure, nevertheless in Struc-Rke this Mach disc is interacting with another low velocity structure unlike any other case.

- In case of bow shock k-ω case shows the most dissipated and smeared out shock structure on the other hand k-ω SST shows similar flow feature as in other cases. The strong bow shock is quite sharply captured in Struc-Rke case due to the high mesh density in the neighborhood. The difference in shock structures between two different solver types is literally negligible, which justifies the segregated solver selection provided that second order upwind scheme is used for density as suggested in [13].

- All of the cases captured downstream circulation region, however it is quite small as opposed to the schematic flow structure designated in [3] (see Fig. 1-4). The main reason for that is the angled injection in the figure opposing to main flow instead of crossing it with 90 degrees, in that case Mach disc is quite upright instead of leaning on the wall. Thus the circulation zone downstream is quite big whereas in numerical simulations it is quite small oppressed by Mach disc that is aligned more to the wall.

3.4. Conclusion

Final conclusion of this part suggests the following;

- A computational mesh composed of hybrid cells, i.e. a boundary layer grid that goes down very close to wall ($y^+ \approx 1$) and an unstructured grid on top of it, is suitable and computationally feasible while being accurate for this problem.

- Enhanced wall treatment is essential to accurately capture this complex phenomena occurring both upstream and downstream of the injection port. Even though it is computationally demanding, the resolution of flow features very close to the wall results a better estimation of side force, which is the integral of pressure on the nozzle wall added to the momentum of the secondary injectant.

- Rke is the most suitable choice for turbulence closure since it is the one closest to experimental results. In addition it is advised for complex three dimensional turbulent flows with separation, recirculation, reattachment and boundary layer under strong pressure gradients, which is the case for this problem [17].

- Segregated solver outperforms coupled-explicit solver in aspects of convergence speed, computer memory and robustness at the expense of a negligible loss of accuracy.

CHAPTER 4

PART TWO – A TYPICAL ROCKET NOZZLE

4.1. Nozzle Geometry and Boundary Conditions

The second part of this study involves the solution of three dimensional flowfield inside a typical conical rocket nozzle with various SITVC parameters mentioned in previous chapters above. Once the optimum solution approach is chosen in the first part of the study for a test case nozzle, which is the solution of RANS with segregated solver accompanied by Realizable k-ε (Rke) turbulence model with enhanced wall treatment approach, it is used without any doubt for this distinct rocket nozzle with a divergence angle of 8.5 degrees. The nozzle has a convergence angle of 45 degrees; throat radius of 20.9mm, the divergent section is about five times the diameter of throat as depicted in Fig. 4-1. For this part the inflow boundary conditions are different than the first part (P_0=7bar, T_0=314K and M=0.1), these values are set according to the capacity of the high pressure air supply system suitable for the cold flow tests that are planned before. The condition for the choking of this nozzle is checked with this supply system i.e. the required mass flow rate for the nozzle to be choked can be supplied with the current reservoir as calculated using MathCad® shown in Figures D-1 to D-3 in Appendix D. For these calculations one-dimensional isentropic gas dynamics equations [24] are utilized for simplicity, note that Mach numbers at exit and inlet are found from “area-Mach relation” tabulated at Ref. [24] and they are not interpolated, therefore the mass flow rates at inlet and exit differ a bit. In fact the inlet Mach number is slightly lower than 0.1 and both mass flow rates values are well below the value of the supply system. Again the turbulence boundary conditions are set to suitable values such as 5% TI and hydraulic diameter of the nozzle, which is the inlet radius of the half geometry as in Fig. D-4. In terms of injection; it is sonic but now with different reservoir conditions from the inlet as in chapter three, compatible to bleed type SITVC configuration (total pressure of the injectant is smaller or at maximum equal to the total pressure of the reservoir) and again it is normal to the nozzle wall through a single orifice located at various locations from the nozzle throat (1.5, 2.5 and 3.5 throat diameters from nozzle throat). Both fluids are air and the orifice size has been estimated as 5mm using one dimensional isentropic flow equations to supply injection mass flow rate 2.8% to 5.7% of the main mass flow rate as shown in Fig. D-5. Finally the choking condition of injection nozzle is checked in Fig.D-6.

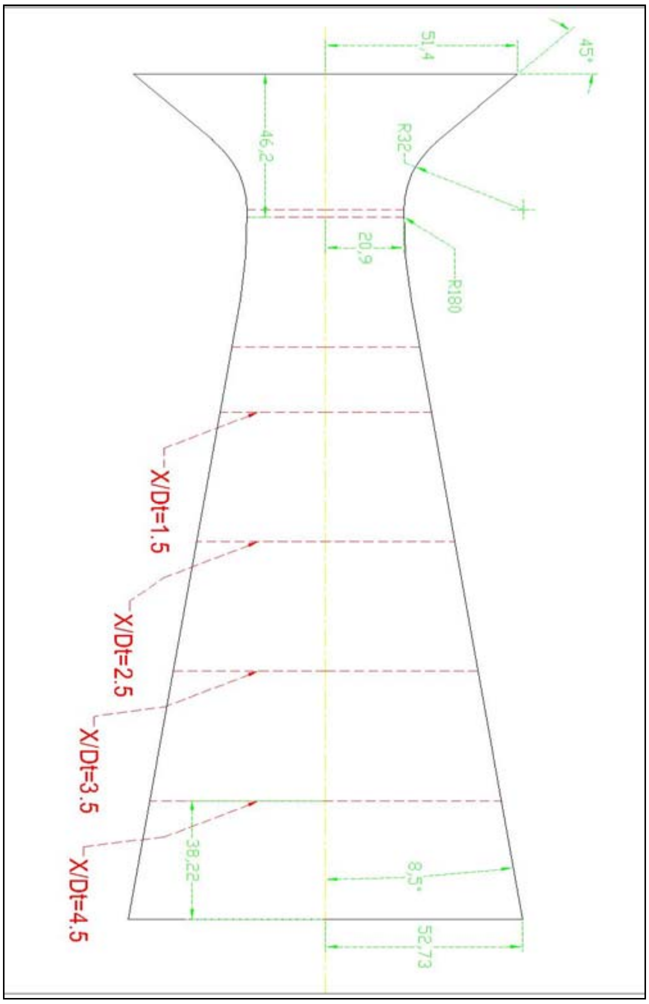

Figure 4-1 Nozzle geometry

Once the geometry and boundary conditions are set in accordance with cold flow test configurations as mentioned in Appendix D, a test matrix is constructed for the SITVC parametric study as shown in Table 4-1. The parameters are injection mass flow rate, the injection location and the injection angle. The injection mass flow rate is commonly non dimensionalized by main mass flow rate and then expressed as total pressure ratio of two jets as in Table 4-1 because the mass flow rate of the injectant is directly proportional to the injection total pressure as noticed from Figures D-1 and D-4. In case of injection location, it is measured from the nozzle throat to injection port and its distance is non dimensionalized by throat diameter.

Table 4-1 Test matrix

Parameter \ Test Run	Injection Location (x/Dt)	Injection Total Pressure ($P_{0inject}/P_0$)	Injection Angle (wrt absolute axes, in degrees)
A1	1.5	1	8.5
A2	1.5	0.84	8.5
A3	1.5	0.68	8.5
A4	1.5	0.5	8.5
B1	2.5	1	8.5
B2	2.5	0.84	8.5
B3	2.5	0.68	8.5
B4	2.5	0.5	8.5
C1	3.5	1	8.5
C2	3.5	0.84	8.5
C3	3.5	0.68	8.5
C4	3.5	0.5	8.5
E1	2.5	1	45
E2	2.5	0.84	45
E3	2.5	0.68	45
E4	2.5	0.5	45

The physics of this “jet in supersonic crossflow” problem is mainly dominated by the momentum ratio of the secondary jet to the primary one (crossing supersonic jet) [25]. If the momentum ratio is high the interaction between the crossing streams is quite strong and high side forces are attained. Consequently in case of injection location, if the injection is made more upstream (closer to nozzle throat) the momentum ratio of the crossing jets would be high thus the effect of interaction is enhanced. For injection mass flow rate, higher injectant flow rates results higher momentum ratios, hence stronger interactions. Finally for injection angle the scenario is a bit different, in the normal to boundary injection; the angle between crossing flows is 90 degrees therefore the momentum ratio is at its maximum, however if the injection angle is decreased i.e. if secondary jet is aligned more to primary stream the momentum ratio of the jets would decrease due to the loss in the secondary jet momentum. Its effective momentum would be multiplied by the cosine of the injection angle. As a consequence for a rocket nozzle with a specific divergence angle, the most efficient way to inject a secondary jet is to inject normal to boundary and for testing different injection angles a common approach is change the divergence angle of the nozzle but still keeping the “crossing angle” as 90 degrees [6]. Because of this, the injection angle investigation is done separately on a fixed injection location (2.5 throat diameters from the nozzle throat) only for 45 degrees of injection.

4.2. Computational Grid and Grid Dependency Study

Figure 4-2 shows the computational grid done by commercial grid generator GAMBIT®; it includes about 840,000 hybrid cells both structured and unstructured for the half geometry (Mesh2); and it has the same boundary types as in the first part obviously. The grid generation methodology is the same as in the previous part, i.e. special attention is given to the diverging section of the nozzle especially in the neighborhood of injection ports thus the mesh is clustered at these regions. The first grid spacing estimation is done again using skin friction coefficient (*Cf*) as in Eq. 3-4 for pipe flows [22, 23] shown in Fig.4-3. Note that x is the distance from the inlet to the injection port, in front of which boundary layer separates, and increasing x distance (injection location in other words) increases first cell centroid distance for $y^{+}\approx 1$ criterion, thus the first cell centroid value is chosen according to closest injection port.

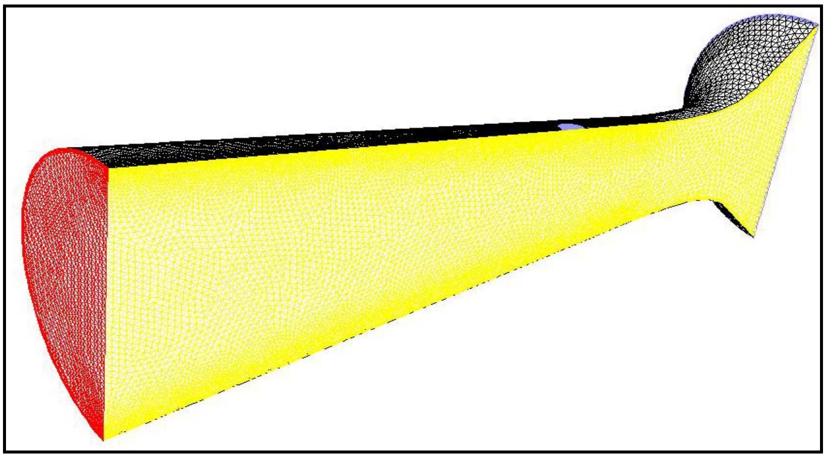

Figure 4-2 Computational grid used in second part

Yplus Estimation (Pipe Flow):

$x := 100mm$ closest injection location $yplus := 1$

$$Rex := \frac{Uinlet \cdot x}{vinlet} \qquad y := \frac{yplus \cdot vinlet}{Uinlet \cdot \sqrt{0.046\,Rex^{-0.2}}} \qquad y = 1.337\times 10^{-6}\,m$$

$Rex = 1.44\times 10^{6}$

Figure 4-3 y^{+} estimation using pipe flow approach

Since the geometry is different than the first part grid dependency study is necessary and done with five distinct computational grids of about 490,000 cells (Mesh0), 740,000 cells (Mesh1), 840,000 cells (Mesh2), 1,090,000 cells (Mesh3) and finally 1,700,000 cells (Mesh4) on case A1 depicted in Table 4-1. The specifications of the computational grids are tabulated in Table 4-2 in terms of mesh type, cell and node numbers, wall treatment together with boundary layer grid features.

Table 4-2 Specifications of the grids tested

Mesh ID	**Mesh 0**	**Mesh 1**	**Mesh 2**	**Mesh 3**	**Mesh 4**
Mesh Type	Hybrid	Hybrid	Hybrid	Hybrid	Hybrid
# of Cells	487446	736245	837063	1091206	1680811
# of Nodes	203469	311866	352309	461512	717996
Wall treatment	Enhanced wall treatment	Enhanced wall treatment	Enhanced wall treatment	Enhanced wall treatment	Enhanced wall treatment
BL grid height (mm)	1.6474	1.6474	1.6474	1.6474	1.574
BL grid first cell height (mm)	0.00133	0.00133	0.00133	0.00133	0.00133
# of cells in BL grid	25	25	25	25	25

The grid resolutions at the symmetry planes corresponding to these five independent grids are shown in Figures 4-4 and 4-5. For this time global (integral) quantities are compared to yield a grid independent simulation, a simple force balance for both axial and side force calculations is accomplished. As mentioned in second chapter only the divergent section of the nozzle is considered; pressure and shear stress are integrated over this section to be complete together with the integration of velocity distribution in three dimensions at the nozzle exit using FLUENT®'s post processing utilities and the effect of injection is always compared to the case without injection. Therefore a no-injection case is also simulated. Also $y^+ \approx 1$ criterion is checked with numerical simulations as shown in Fig.4-6 for the Mesh2.

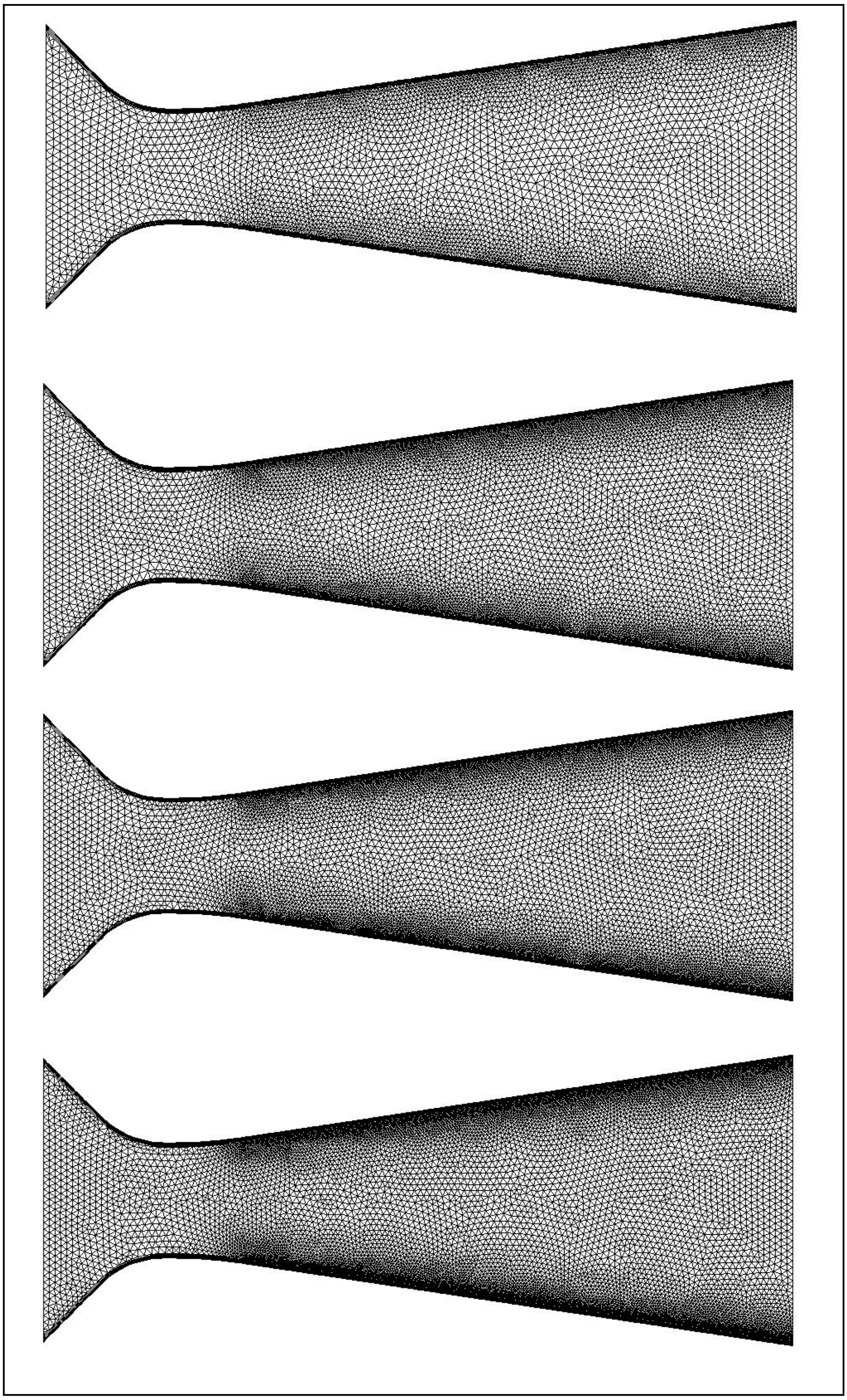

Figure 4-4 The grids on the symmetry planes corresponding to Mesh0, Mesh1, Mesh2 and Mesh3

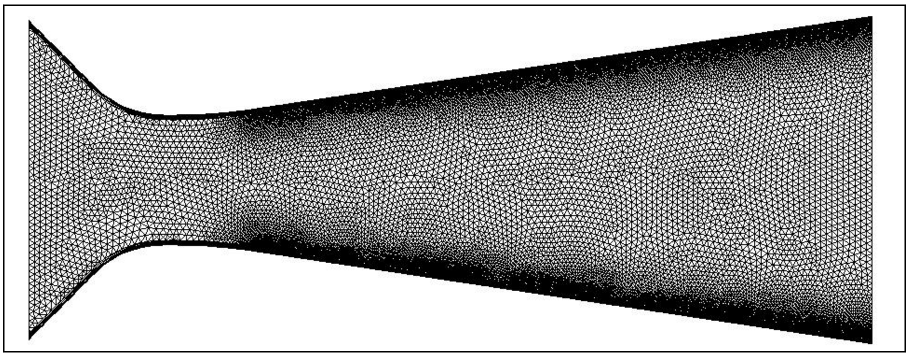

Figure 4-5 The grid on the symmetry plane corresponding to Mesh4

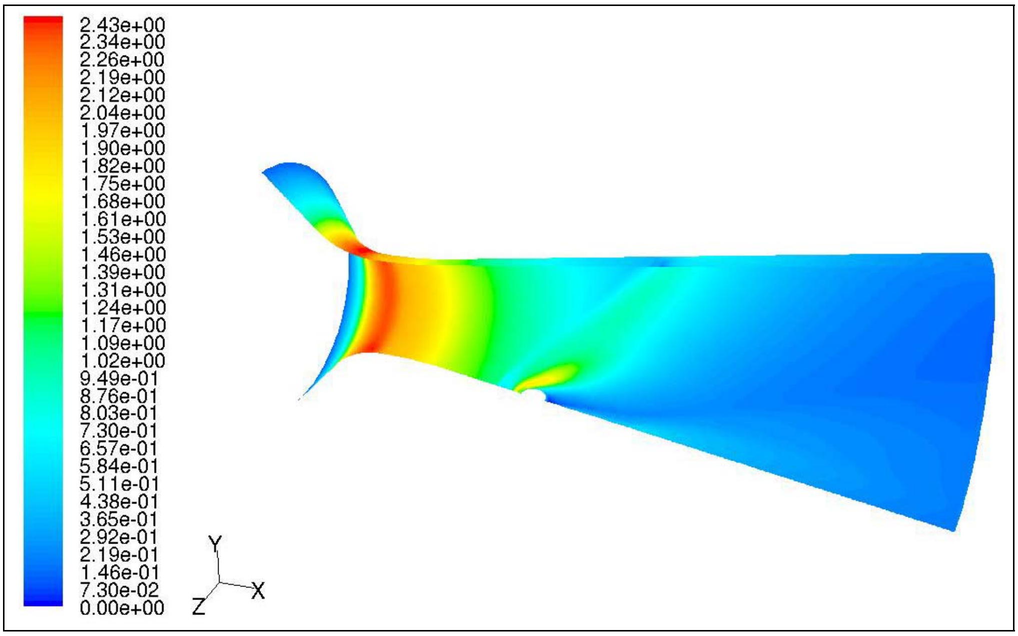

Figure 4-6 y^+ contours for Mesh2 (with rke turbulence model)

Fig.4-7 shows the contour plots of velocity magnitude (in m/s) on the symmetry plane corresponding to the grids tested, the black one is the finest grid whereas the cyan one is the coarsest one. The contour lines are all alike starting from the convergent section of the nozzle up to injection port. Downstream of the injection location velocity contours start to deviate, especially in the regions of recompression. As a consequence the global performance parameters are examined to draw a conclusion about the computational grid. Table 4-3 shows the grid dependency results based on SITVC performance. After the third grid the internal flowfield is essentially invariant and the global performance parameters do not experience considerable changes; thus Mesh2 has been selected for the parametric study.

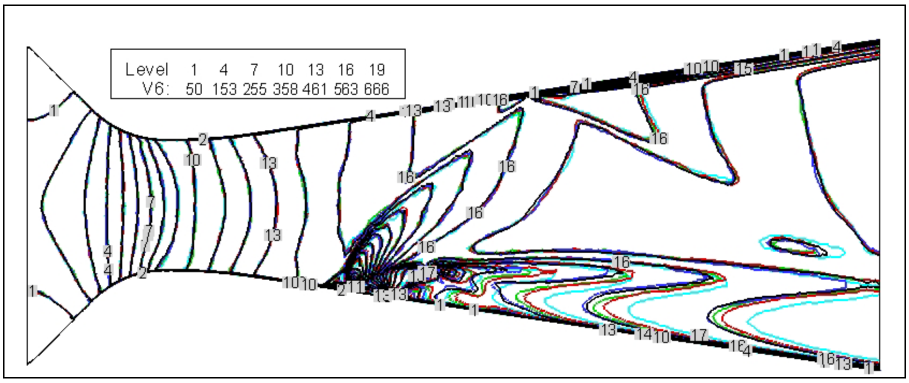

Figure 4-7 Magnitude of velocity contours at the symmetry plane for Meshes 0 to 4 (black-blue-red-green-cyan, in coarsening order)

Table 4-3 Grid dependency results

Parameter \ Mesh ID	Mass flow rate ratio	Thrust Ratio, TR	Amplification, K	Axial Thrust Augmentation, ATA %
Mesh0	0.05737	-0.16324	-2.84522	5.46461
Mesh1	0.05782	-0.16486	-2.85121	5.53550
Mesh2	0.05786	-0.16482	-2.84871	5.58747
Mesh3	0.05807	-0.16562	-2.85199	5.58919
Mesh4	0.05798	-0.16567	-2.85721	5.62309

4.3. Results and Discussion

Once Mesh2 is selected for the parametric study, several runs are accomplished to assess the effects of mass flow rate ratio and injection location on SITVC performance. Figures from 4-8 to 4-10 show the performance evaluation of this rocket nozzle. Batch A corresponds to a case with upstream injection at $x/D_t=1.5$, Batch B and E corresponds to $x/D_t=2.5$ and Batch C corresponds to $x/D_t=3.5$. As it can be observed from Fig.4-8 that both Batch A and B result negative thrust values over a range of mass flow rate ratios, the main reason for that is the impingement of the strong bow-shock on the opposite wall and then followed by the reflection from that surface afterwards directed to the nozzle axis. The main flow passing through the impinging and reflection shock waves is strongly dissipated, the pressure distribution on the nozzle has become relatively even or negative hence resulted negative side forces; whereas for Batch C the bow-shock is not impinged on the opposite wall, created pressure recovery region downstream of the injection port due to recompression and thus resulted a positive force on the nozzle wall consequently positive net side force on nozzle. Furthermore as the injection mass flow rate increases the side force (negative or positive) increases as expected. This is due to the fact that the more the amount of injectant penetrated into primary flow the stronger the bow-shock is due to the increased momentum of the secondary jet and thus the pressure downstream of the bow-shock reaches higher values.

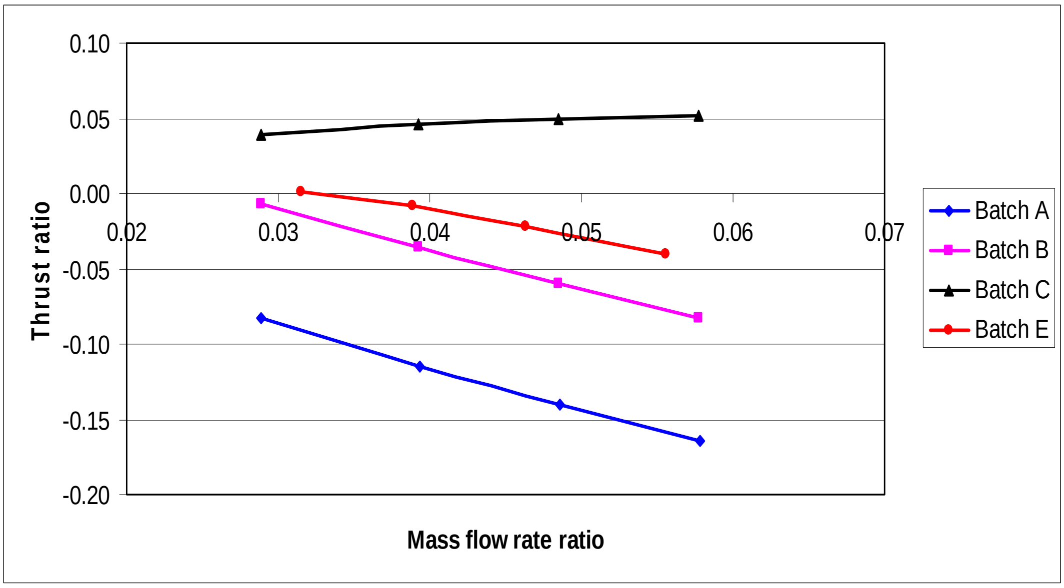

Figure 4-8 Thrust ratio vs. mass flow rate ratio

Another thing to note is the non-linear behavior of the side force with injectant mass flow rate for Batch C when going to higher mass flow rates. It is also observed by Ko[6] for a small divergence angle nozzle (half angle of 10 degrees). However for Batch A and B a linear trend of side force with injection mass flow rate is observed, which contradicts with his findings, but it makes sense in the way that once the specific amount of injectant is injected, and it makes the bow-shock impinge on opposite wall and reflect from it, increasing the mass flow rate of the injectant is going to amplify this effect and a stronger bow-shock is going to be created and then reflected from opposite wall enabling higher pressures acting on opposite wall and more fluid to be directed along the axis with high velocity.

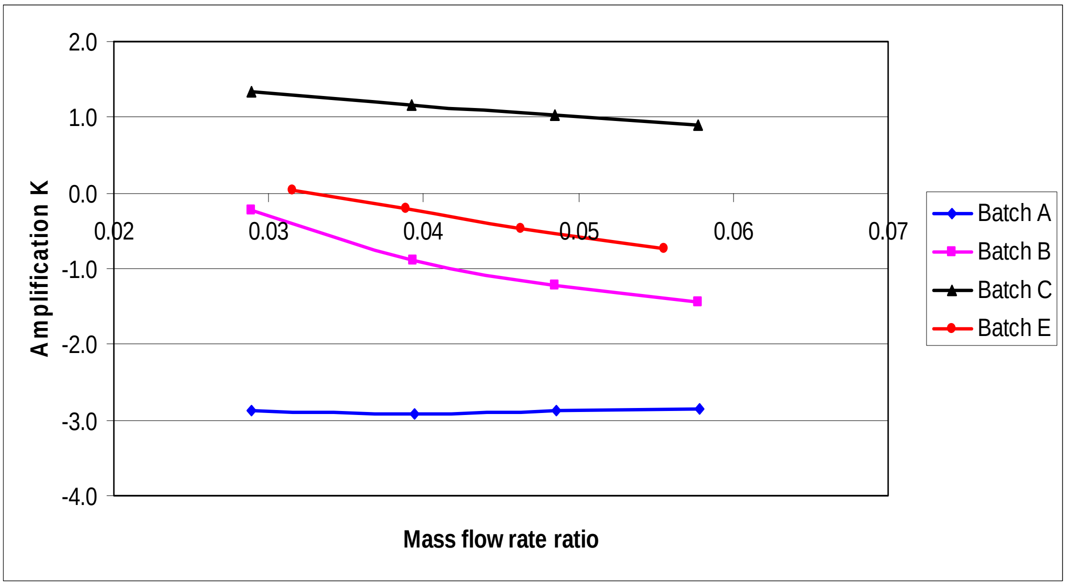

Figure 4-9 Amplification vs. mass flow rate ratio

In case of Amplification, increasing mass flow rate reduces the efficiency of the SITVC system as shown in Fig.4-9, especially for batches B and C. It is expected and noted by several authors (see Ref. [3-6]), it is because of the fact that amount of side force gained by injection is not linear with the amount of injectant, injecting more and more amount of fluid does not necessarily ensure higher and higher amount of side forces to be obtainable, since the governing equations of fluid flow are not linear in nature. And for the Batch A the curve is more or less invariant.

For Augmented Axial Thrust, increasing mass flow rate increases the amount of axial thrust gained for the loss of the side force as shown in Fig.4-10 as expected. However for batches A and B this effect is much more pronounced since in these batches the bow-shock is reflected from the opposite wall and main flow is directed much more to the nozzle axis compared to non-reflection case, Batch C. In this case a considerable amount of axial thrust is converted to side thrust thus the gain for the loss of axial force is less.

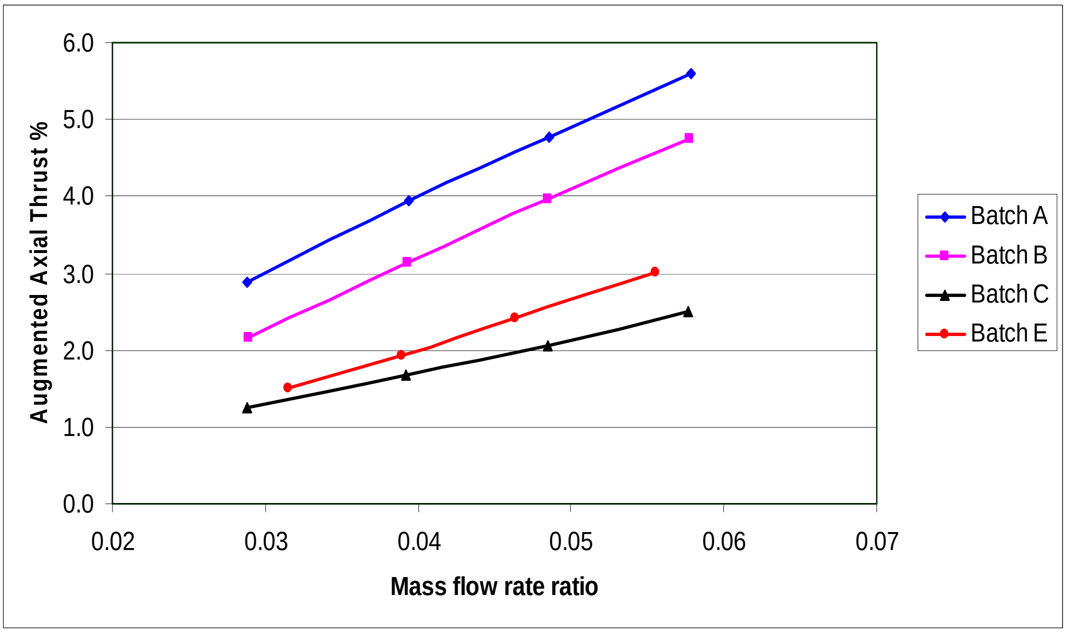

Figure 4-10 Augmented axial thrust vs. mass flow rate ratio

For the investigation on injection angle, Batch E results that only slight performance increases can be achieved by aligning the secondary jet more to the nozzle axis. Note that Batch E is same with Batch B except the injection is done with 45 degrees instead of normal to boundary. Thus its effect should be measured with respect to Batch B. In case of thrust ratio this batch shifted Batch B curve a bit up, however the impingement of bow shock on the opposite wall is not averted except for the lowest two mass flow rate ratios. Therefore the mechanism mentioned above takes over the flowfield and it results the negative side thrust values. As mentioned earlier increasing injection angle can make the strong bow-shock intersect nozzle exit plane, instead of reflecting from upper nozzle wall, which is desirable, but at the same time it weakens the bow shock by diminishing the effect of crossing of two streams. Thus the overall side force is quite dependent on the interaction of crossing flows.

In case of Amplification same behavior is observed with Batch E, non-linear decrease of performance with increasing injection mass flow rate. The increase in performance compared to Batch B is quite small again. Finally for Augmented Axial Thrust, lower thrust values are observed compared to Batch B. The reason for that might be the lower strength of the bow shock that is impinged on opposite nozzle wall and then reflected from that surface. This mechanism directs the main flow towards nozzle axis by reducing the effect of obstruction of the second jet, creating relatively even pressure distribution on nozzle wall. Therefore the stronger this mechanism the stronger subsequent reflected shock system and thus the more aligned the main flow to nozzle axis producing more additional axial thrust.

CHAPTER 5

CONCLUSION

A parametric study on (SITVC) has been accomplished numerically with the help of a commercial (CFD) code, FLUENT®; this study consists of two parts. The first part includes the simulation of three dimensional flowfield inside a test case nozzle for validating the solver and more importantly, for the selection of parameters associated with both computational grid and the CFD solver such as mesh size, turbulence model accompanied with two different wall treatment approaches, and solver type. This part revealed that:

- A computational mesh composed of hybrid cells, i.e. a boundary layer grid that goes down very close to wall ($y^+ \approx 1$) and an unstructured grid on top of it, is suitable and computationally feasible while being accurate for this problem.

- Enhanced wall treatment is essential to accurately capture this complex phenomena occurring both upstream and downstream of the injection port. Even though it is computationally demanding, the resolution of flow features very close to the wall results a better estimation of side force, which is the integral of pressure on the nozzle wall added to the momentum of the secondary injectant.

- Rke is the most suitable choice for turbulence closure since it is the one closest to experimental results. In addition it is advised for complex three dimensional turbulent flows with separation, recirculation, reattachment and boundary layer under strong pressure gradients, which is the case for this problem.

- Segregated solver outperforms coupled-explicit solver in aspects of convergence speed, computer memory and robustness at the expense of a negligible loss of accuracy.

In the second part the effects of injection mass flow rate, injection location with a fixed injection angle on SITVC performance is studied parametrically for a typical rocket nozzle with a conical diverging cone of 8.5 degrees. A test matrix is constructed, several numerical simulations are run to yield the assessment of performance of SITVC system, and the results stated that for a nozzle with small divergence angle:

- Downstream injections such as injection port with distances of 2.5-3.5 throat diameters from the nozzle throat lead to higher efficiencies over a certain range of total pressure ratios (i.e., mass flow rate ratios).

- The impingement and reflection of shock waves should definitely be prevented for better performance. A remedy might that the upstream injections should be aligned more to the nozzle axis (i.e. higher injection angles, α) with moderate injection mass flow rates and for the moderate injection locations such as 2-2.5 throat diameters from the nozzle throat, this angle can be adjusted to the neighborhood of 45 degrees. However one thing to keep in mind is that the momentum ratio of the secondary jet to the primary one is the essence of SITVC, increasing injection angle reduces the effect of the interaction of crossing streams.

- Injection locations too much downstream may result reversed flows on nozzle exit, which reduces the SITVC performance.

For future work;

- More accurate turbulence modeling should be utilized to capture better the physical phenomenon, for instance as a first step RSM can be tried to account for the anisotropy (directional dependence) of eddy viscosity afterwards Detached Eddy Simulation (DES) or Large Eddy Simulation (LES) can be made use of to accurately resolve the time evolution of secondary jet in the internal flowfield of the nozzle

- Multiple injection ports in both series and parallel can be tried and their effect on the global SITVC performance might be carried out.

- A case with real exhaust gas properties obtained from static firings can be simulated and the difference in flowfield and thus in the SITVC performance from air to air interaction may be addressed.

- The eventual goal can be accomplished with a lot of effort, that is the realization of cold flow tests to validate CFD and afterwards static firing tests with real conditions would be done.

- In fact this nozzle has quite a small divergence angle for SITVC applications; however it is picked according to ease of use and know-how. For a better SITVC performance nozzles with higher divergence angles like 15-20 degrees can be chosen; on the other hand increasing divergence angle of a nozzle increases divergence losses in axial thrust. What can be proposed is to use a contoured nozzle with injection to assure better SITVC performance and at the same time to keep divergence losses low.

REFERENCES

[1] Timnat, Y., "*Advanced Chemical Rocket Propulsion*", Academic Press, 1987.

[2] Sutton, G.W., "*Rocket Propulsion Elements*", 7th ed., John Wiley & Sons, 2001.

[3] Balu, R., "Analysis of Performance of a Hot Gas Injection Thrust Vector Control System", *Journal of Propulsion and Power*, Vol. 4, 1991, pp. 580-585.

[4] Newton, J.F., Spaid, F.M., "Interaction of Secondary Injectants and Rocket Exhausts for Thrust Vector Control", *Journal of the American Rocket Society*, August 1962, pp, 1203-1211.

[5] Broadwell, J.E., "Analysis of Fluid Mechanics of Secondary Injection for Thrust Vector Control", *AIAA Journal,* Vol. 1, No. 10, 1963, pp. 1067-1075.

[6] Ko, H., Yoon, W., "Performance Analysis of Secondary Gas Injection into a Conical Rocket Nozzle", *Journal of Propulsion and Power*, vol: 18, 2002, pp. 585-591.

[7] Huzel, D.K., Huang, D.H., "Modern Engineering for Design of Liquid Propellant Rocket Engines", AIAA, Washington, DC, Vol. 147, 1992, p. 209.

[8] Masuya, G., "Secondary Gas Injection into a Supersonic Conical Nozzle", AIAA Journal, Vol. 15, No.3, 1977, pp. 301-302.

[9] World wide web, [cited 20 October 2002]

[10]Zeierman, I., Timnat, Y. M., "Full Control of Solid Propellant Rockets by Secondary Injection", *Journal of Spacecraft and Rockets ,* Vol. 10, No. 3, 1973.

[11] Inouye, T., "Experiments on Rocket Thrust Vector Control by Hot Gas Injection", *Journal of Spacecraft and Rockets*, Vol. 3, No.4, 1966, pp. 737-739.

[12] Dhinagram, R., BOSE, T. K., "Comparison of Euler and Navier Stokes Solutions for Nozzle Flows with Secondary Injection", AIAA Paper 96-0453, Jan. 1996.

[13] Fluent Inc., URL: http://www.fluent.com [cited 27 October 2005].

[14] Erdem, E., *et al.*, “Experimental and Numerical Investigation of the Flowfield inside a Solid Propellant Booster in Presence of Slag Accumulation”, VKI Diploma Course Report, July 2005

[15] Anderson, J. D. Jr , *et al*., “Introduction to CFD”, VKI Lecture Series, 2004

[16] Middle East Technical University, “CFD on Unstructured Grids”, AE546 Lecture notes, 2003.

[17] Fluent Inc., “Modeling Turbulence”, Tutorial, 2002.

[18] Versteeg, H. K., Malalasekera, W., “*An Introduction to Computational Fluid Dynamics-The Finite Volume Method*”, Prentice Hall, 1995

[19] Hoffman, K. A., Chiang, S. T., “*Computational Fluid Dynamics*”, EES Books, 2000

[20] Wilcox, D. C., “*Turbulence Modeling for CFD*”, DCW Industries, 2000

[21] Schlichting, H., “*Boundary Layer Theory*”, McGraw-Hill, 1968.

[22] Erdem, E., *et al.*, “Parametric Study of Secondary Gas Injection into a Conical Rocket Nozzle for Thrust Vectoring”, AIAA Paper 2006-4942, July 2006

[23] Stanford University, “CFD using commercial CFD codes”, ME469B Lecture notes, 2003.

[24] Anderson, J. D. Jr.,“*Fundamental of Aerodynamics*”, McGraw-Hill, 1991

[25] Balar, R., *et al.*, “Comparison of Parallel and Normal Fuel Injection in a Supersonic Combustor”, AIAA Paper 2006-4442, July 2006

APPENDIX A

LITERATURE SURVEY ON SITVC APPLICATIONS

As noted in introduction chapter, HGITVC and LITVC systems have been used in various systems in Japan, India, United States and Russia since 60's. The following tables [9] include long range missile/launch vehicle systems around the globe, which are using HGITVC system as auxiliary control units in certain stages of the vehicles, together with their specifications.

Table A-1 Japanese systems using HGITVC system

Name	**Propulsion System Type**	**Guidance and Control Systems**	**Notes**
M-3C (JAPAN)	Solid propellant 3 stages	Inertial Navigation System and HGITVC at 2nd Stage	Long range missile/satellite launch vehicle
M-3H (JAPAN)	Solid propellant 4 stages	Inertial Navigation System and HGITVC at 2nd Stage	Long range missile/satellite launch vehicle
M-3H (JAPAN)	Solid propellant 3 stages	Inertial Navigation System and HGITVC at 2nd Stage	Long range missile/satellite launch vehicle

Table A-2 Japanese system specifications that are using HGITVC system

M-3C	1.stage	2.stage	3.stage
Total length (m)	20.241	8.395	2.326
Maximum diameter (m)	1.410	1.410	1.144
Total weight (kg)	37445	11144	1311
Propellant weight (kg)	20453	7174	1075
Freon (kg)		173	
H_2O_2 (kg)		55	

M-3H	1.stage	2.stage	3.stage	4.stage
Total length(m)	23.80	8.895	3.059	1.408
Maximum diameter(m)	1.410	1.410	1.136	0.932
Total weight(kg)	44714	11307	1436.4	187.25
Propellant weight(kg)	27098	7195	1083.7	45.55
Freon(kg)		56.0		
H_2O_2(kg)		84.7		

M-3S	1.stage	2.stage	3.stage
Total length(m)	5.794	8.895	2.501
Maximum diameter(m)	0.310	1.410	1.135
Total weight(kg)	4119.2	11043.0	1425.6
Propellant weight(kg)	2741.2	7201.0	1083.7
Freon(kg)		42.0	
H_2O_2(kg)		28.0	

Table A-3 Indian system specifications that are using HGITVC system

Name	Propulsion System Type	Guidance and Control Systems	Notes
PSLV-C4/ PSLV-C3 **(INDIA)**	Solid propellant in 1^{st} and 3^{rd} stages, Liquid propellant in 2^{nd} and 4^{th} stages • At 1^{st} stage 138 tons of HTPB solid propellant + 6 times 9tons of HTPB • At 2^{nd} stage 40 tons of UDMH liquid propellant • At 3^{rd} stage 7.6/7 tons of HTPB solid propellant • At 4^{th} stage 2.5/2 tons of MMH and Nitrogen Oxide(N_2O_4) liquid propellant	Inertial Navigation System At 1^{st} stage HGITVC for pitching and yawing, for rolling moment HGITVC strapped to side motors At 2^{nd} stage reaction motor for pitching and yawing and for rolling hot gas reaction motor At 3^{rd} stage moveable nozzle for pitching and yawing, and for rolling liquid propellant thrusters At 4^{th} stage reaction motor for pitching and yawing, for rolling liquid propellant thrusters	Long range missile/satellite launch vehicle Length: 44.4 m Motor Diameter: 2.80416 m Range: 2800km Weight: 295 ton Take-off Thrust: 5338kN

The propellant HTPB is “Hydorxl Terminated Poly Butadiene”, MMH is “Mono Metyl Hydrazine” and UDMH stands for “Unsymmetrical Di-Metyl Hydrazine”.

The following tables [9] include long range missile/launch vehicle systems around the globe, which are using LITVC system as auxiliary control units in certain stages of the vehicles, together with their specifications.

Table A-4 US and Russian system specifications that are using LITVC (cont. on next page)

Name	**Propulsion System Type**	**Guidance and Control Systems**	**Notes**
POLARIS A-3 (USA)	Solid propellant (2 stages) At 1st stage polyuretan propellant At 2nd stage double base propellant	Inertial Navigation System LITVC at 2nd stage (Freon 114)	Long range missile/satellite launch vehicle Length: 9.4488 m Motor Diameter: 1.3716 m Range: 4023.36km Weight: 35700 lb
TITAN 3C-3D (USA)	Solid and Liquid propellant (4 or 3 stages) At 1st stage solid propellant At 2nd , 3rd and	Inertial Navigation System LITVC tested on static firings	Long range missile/satellite launch vehicle Length: 42 m Motor Diameter: 3.1 m

	4^{th} stages N_2O_4/Aerozine		Range: 185km to orbit Weight: 626,190 ton
TITAN 3M (USA)	Solid and Liquid propellant (3 stages) At 1^{st} stage solid propellant At 2^{nd} and 3rd stages N_2O_4/Aerozine	Inertial Navigation System LITVC tested on static firings	Long range missile/satellite launch vehicle Length: 39 m Motor Diameter: 3.1m Range: 185km to orbit Weight: 836.6 ton
SINNER (RUSSIA)	Solid propellant (3 stages)	Inertial Navigation System LITVC tested on static firings	Long range missile/satellite launch vehicle Length: 18.5 m Motor Diameter: 1.79m Range: 9000km Weight: 41.2-44.5 ton

APPENDIX B

GOVERNING EQUATIONS OF FLUID FLOW

The governing equations of the fluid flow mean the conservation laws, which are conservation of mass (continuity equation), conservation of momentum (Newton's 2nd law of motion) and conservation of energy (the first law of thermodynamics). The unknowns are density, velocity (three components in three Cartesian directions as u, v and w) and total energy; they are solved for in the flow domain with appropriate BCs. Considering the fact that all the flow variables: velocity, temperature, density and total energy are functions of three coordinates and time respecting the Spatial (Eulerian) description, and they are expressed in the following differential conservative form within a control volume fixed in space surrounded by control surfaces in Equations B-3 [14, 15]:

$$\frac{\partial \rho}{\partial t} + \vec{\nabla} \cdot \left(\rho \vec{V} \right) = 0 \tag{B-1}$$

$$\frac{\partial \left(\rho \vec{V} \right)}{\partial t} + \vec{\nabla} \cdot \left(\rho \vec{V} \vec{V} + p \bar{\bar{I}} - \bar{\bar{\tau}} \right) = \rho \vec{F}_b \tag{B-2}$$

$$\frac{\partial \left(\rho E \right)}{\partial t} + \vec{\nabla} \cdot \left(\rho \vec{V} H - \bar{\bar{\tau}} \cdot \vec{V} + \vec{q} \right) = \rho \vec{F}_b \cdot \vec{V} \tag{B-3}$$

where ρ is fluid density, V is the velocity vector, p is the pressure, E is the total energy, H is the stagnation enthalpy, $\bar{\bar{\tau}}$ is the stress tensor, $\bar{\bar{I}}$ is the identity tensor and q is the heat flux vector. Lastly t is time and F_b is the contribution of body forces.

Eq. B-1 shows the accumulation of mass (per unit volume) within a control volume by the convection (or advection) through the control surfaces. In addition Eq. B-2 shows the acceleration of fluid particles in the control volume by external forces such as surface forces (pressure and shear stress) and body forces (gravity, magnetic field, etc.). And finally Eq. B-3 represents the change of energy in the control volume by the work done on the fluid by surface and body forces or any other external means (pump, compressor, etc.) plus the net heat transfer through the boundaries of the control volume.

These equations are coupled (requirement of a simultaneous solution) and they are in primitive forms. However the system formed by these equations is incomplete. The constitutive equations should accompany this system to make the system solvable and of practical use. These are literally the Newton's law of shear, Fourier's law of conduction and ideal gas law [14, 15]. The form of the equations of practical use is the so called Navier-Stokes equations based on the assumptions, which are:

- The fluid is continuous; the continuum assumption is valid (Knudsen number criterion)

- The fluid is isotropic (it has the same behavior in all three directions)

- Stokes Law of Friction applies and the fluid is Newtonian (Shear stresses are linearly proportional to deformation rates) as shown in Equations B-5 to 5-10.

$$\sigma_{xx} = \lambda \vec{\nabla} \cdot \vec{V} + 2\mu \frac{\partial u}{\partial x} \qquad \sigma_{yy} = \lambda \vec{\nabla} \cdot \vec{V} + 2\mu \frac{\partial v}{\partial y}$$

$$\sigma_{zz} = \lambda \vec{\nabla} \cdot \vec{V} + 2\mu \frac{\partial w}{\partial z} \qquad \tau_{xy} = \tau_{yx} = \mu\left(\frac{\partial v}{\partial x} + \frac{\partial u}{\partial y}\right)$$

$$\tau_{xz} = \tau_{zx} = \mu \cdot \left(\frac{\partial w}{\partial x} + \frac{\partial u}{\partial z} \right) \qquad \tau_{yz} = \tau_{zy} = \mu \cdot \left(\frac{\partial w}{\partial y} + \frac{\partial v}{\partial z} \right) \qquad \text{(B-4 to B-9)}$$

where μ is the molecular viscosity coefficient and λ is the bulk viscosity coefficient. The following assumption of Eq. B-10 made by Stokes is frequently used.

$$\lambda = -\frac{2}{3}\mu \qquad \text{(B-10)}$$

Using these assumptions, the conservation of momentum in 3 cartesian directions x, y and z respectively becomes in Equations B-11 to B-13 as:

$$\frac{\partial(\rho u)}{\partial t} + \frac{\partial(\rho u^2)}{\partial x} + \frac{\partial(\rho uv)}{\partial y} + \frac{\partial(\rho uw)}{\partial z} = -\frac{\partial p}{\partial x} + \frac{\partial}{\partial x}\left(\lambda \nabla \cdot \vec{V} + 2\mu \frac{\partial u}{\partial x} \right)$$
$$+ \frac{\partial}{\partial y}\left(\mu\left(\frac{\partial v}{\partial x} + \frac{\partial u}{\partial y} \right)\right) + \frac{\partial}{\partial z}\left(\mu\left(\frac{\partial u}{\partial z} + \frac{\partial w}{\partial x} \right)\right) + \rho g_x$$

$$\frac{\partial(\rho v)}{\partial t} + \frac{\partial(\rho uv)}{\partial x} + \frac{\partial(\rho v^2)}{\partial y} + \frac{\partial(\rho vw)}{\partial z} = -\frac{\partial p}{\partial y} + \frac{\partial}{\partial x}\left(\mu\left(\frac{\partial v}{\partial x} + \frac{\partial u}{\partial y} \right)\right)$$
$$+ \frac{\partial}{\partial y}\left(\lambda \nabla \cdot \vec{V} + 2\mu \frac{\partial v}{\partial y} \right) + \frac{\partial}{\partial z}\left(\mu\left(\frac{\partial v}{\partial z} + \frac{\partial w}{\partial y} \right)\right) + \rho g_y$$

$$\frac{\partial(\rho w)}{\partial t} + \frac{\partial(\rho uw)}{\partial x} + \frac{\partial(\rho vw)}{\partial y} + \frac{\partial(\rho w^2)}{\partial z} = -\frac{\partial p}{\partial z} + \frac{\partial}{\partial x}\left(\mu\left(\frac{\partial w}{\partial x} + \frac{\partial u}{\partial z} \right)\right)$$
$$+ \frac{\partial}{\partial y}\left(\mu\left(\frac{\partial w}{\partial y} + \frac{\partial v}{\partial z} \right)\right) + \frac{\partial}{\partial z}\left(\lambda \nabla \cdot \vec{V} + 2\mu \frac{\partial w}{\partial z} \right) + \rho g_z$$

(B-11-13)

Furthermore the energy equation can be expressed with Stokes' assumption as in [15].

APPENDIX C

CALCULATION OF BOUNDARY CONDITIONS FOR TEST CASE NOZZLE

The calculation of boundary conditions for inlet, injection and exit is as follows in Figures C-1 to C-5.

Inlet Conditions:

$P0 := 2 \times 10^6 Pa \quad T0 := 616K \qquad M0 := 0.2$

Material Properties:

AIR $\qquad \gamma := 1.4 \qquad R := 287 \frac{J}{kg \cdot K} \qquad c1 := 1.46 \cdot 10^{-6} \cdot Pa \cdot \frac{s}{K^{0.5}} \qquad c2 := 112K$

Inlet Geometrical Dimesions:

$r := 40mm$

$Area := \pi \cdot r^2 \quad Area = 5.027 \times 10^{-3} m^2 \qquad Perimeter := 2\pi r \quad Dh := 4.\frac{Area}{Perimeter} \qquad Dh = 0.08\, m$

Inlet Boundary Conditions:

$$P := \frac{P0}{\left[1 + \frac{(\gamma - 1)}{2} \cdot M0^2\right]^{\left(\frac{\gamma}{\gamma - 1}\right)}} \qquad P = 1.945 \times 10^6\, Pa$$

$$T := \frac{T0}{\left[1 + \frac{(\gamma - 1)}{2} \cdot M0^2\right]} \qquad T = 611.111\, K$$

$a := \sqrt{\gamma \cdot R \cdot T} \qquad a = 495.524 \frac{m}{s} \qquad \rho := \frac{P}{R \cdot T} \qquad \rho = 11.09 \frac{kg}{m^3}$

$U := M0 \cdot a \qquad U = 99.105 \frac{m}{s} \qquad \mu := c1 \cdot \left(1 + \frac{c2}{T}\right)^{-1} \cdot \sqrt{T} \qquad \mu = 3.05 \times 10^{-5} \frac{kg}{m\, s}$

$\nu := \frac{\mu}{\rho} \qquad \nu = 2.751 \times 10^{-6} \frac{m^2}{s}$

Figure C-1 Calculation of inlet boundary conditions

Inlet Turbulence Conditions:

$TI := 0.05 \qquad lengthscale := 0.07 \cdot Dh \qquad lengthscale = 5.6 \times 10^{-3}\,m \qquad C\mu := 0.09$

$k := \frac{3}{2} \cdot (TI \cdot U)^2 \qquad k = 36.832Sv$

$\varepsilon := C\mu^{\frac{3}{4}} \cdot \frac{k^{\frac{3}{2}}}{lengthscale} \qquad \varepsilon = 6.559 \times 10^3 \frac{m^2}{s^3} \qquad \omega := \frac{k^{\frac{1}{2}}}{C\mu^{\frac{1}{4}} \cdot lengthscale} \qquad \omega = 1.979 \times 10^3\,Hz$

$veddy := \sqrt{\frac{3}{2}} \cdot U \cdot TI \cdot lengthscale \qquad veddy = 0.034 \frac{m^2}{s}$

$Reh := \frac{U \cdot Dh}{\nu} \qquad Reh = 2.883 \times 10^6$

Figure C-2 Calculation of inlet turbulence boundary conditions

Inject Conditions:

$P0 := 2 \times 10^6 Pa \qquad T0 := 616K \qquad Mi := 1$

Material Properties:

AIR $\qquad \gamma := 1.4 \qquad R := 287 \frac{J}{kg \cdot K} \qquad c1 := 1.46 \cdot 10^{-6} \cdot Pa \cdot \frac{s}{K^{0.5}} \qquad c2 := 112K$

Inject Geometrical Dimesions:

$r := 2mm$

$Area := \pi \cdot r^2 \qquad Area = 1.257 \times 10^{-5}\,m^2 \qquad Perimeter := 2\pi r \qquad Dh := 4. \frac{Area}{Perimeter} \qquad Dh = 4 \times 10^{-3}\,m$

Inject Boundary Conditions:

$$P := \frac{P0}{\left[1 + \frac{(\gamma - 1)}{2} \cdot Mi^2\right]^{\left(\frac{\gamma}{\gamma - 1}\right)}} \qquad P = 1.057 \times 10^6\,Pa$$

$$T := \frac{T0}{\left[1 + \frac{(\gamma - 1)}{2} \cdot Mi^2\right]} \qquad T = 513.333\,K$$

$a := \sqrt{\gamma \cdot R \cdot T} \qquad a = 454.156 \frac{m}{s} \qquad \rho := \frac{P}{R \cdot T} \qquad \rho = 7.172 \frac{kg}{m^3}$

$U := Mi \cdot a \qquad U = 454.156 \frac{m}{s} \qquad \mu := c1 \cdot \left(1 + \frac{c2}{T}\right)^{-1} \cdot \sqrt{T} \qquad \mu = 2.715 \times 10^{-5} \frac{kg}{m\,s}$

Figure C-3 Calculation of injection boundary conditions

Inject Turbulence Conditions:

$TI := 0.05$ $\quad lengthscale := 0.07 \cdot Dh$ $\quad lengthscale = 2.8 \times 10^{-4}\,m$ $\quad C\mu := 0.09$

$k := \frac{3}{2} \cdot (TI \cdot U)^2$ $\quad k = 773.465Sv$

$\varepsilon := C\mu^{\frac{3}{4}} \cdot \frac{k^{\frac{3}{2}}}{lengthscale}$ $\quad \varepsilon = 1.262 \times 10^{7}\,\frac{m^2}{s^3}$ $\quad \omega := \frac{k^{\frac{1}{2}}}{C\mu^{\frac{1}{4}} \cdot lengthscale}$ $\quad \omega = 1.813 \times 10^{5}\,Hz$

$\nu eddy := \sqrt{\frac{3}{2}} \cdot U \cdot TI \cdot lengthscale$ $\quad \nu eddy = 7.787 \times 10^{-3}\,\frac{m^2}{s}$

$Reh := \frac{U \cdot Dh}{\nu}$ $\quad Reh = 4.798 \times 10^{5}$

Figure C-4 Calculation of injection boundary conditions

Outlet Geometrical Dimesions with Boundary Conditions

$rinlet := 40mm$ $\quad rthroat := 13mm$ $\quad Areathroat := \pi \cdot rthroat^2$

$Areaexit := Areathroat \cdot 4.64$ $\quad rexit := \sqrt{\frac{Areaexit}{\pi}}$ $\quad Perimeter := 2\pi rexit$ $\quad Dh := 4. \frac{Areaexit}{Perimeter}$

from isentropic flow tables

$Dh = 0.056m$

$P := \frac{P0}{42.65}$ $\quad T := \frac{T0}{2.922}$ $\quad Mexit := 3.1$

$P = 4.689 \times 10^{4}\,Pa$ $\quad T = 210.815K$

Figure C-5 Calculation of outlet boundary conditions

APPENDIX D

CALCULATION OF BOUNDARY CONDITIONS FOR ROCKET NOZZLE

The calculation of boundary conditions for inlet, injection and exit is as follows in Figures D-1 to D-4.

Inlet Conditions:

$P0 := 7 \times 10^5 Pa \qquad T0 := 314K$

Material Properties:

AIR $\qquad \gamma := 1.4 \qquad R := 287 \frac{J}{kg \cdot K} \qquad c1 := 1.46 \cdot 10^{-6} \cdot Pa \cdot \frac{s}{K^{0.5}} \qquad c2 := 112K$

Inlet Geometrical Dimensions:

$r := 51.4mm$

$Areainlet := \pi \cdot r^2 \qquad Areainlet = 8.3 \times 10^{-3}\, m^2 \qquad Perimeter := 2\pi r$

$Dh := 4.\frac{Areainlet}{Perimeter} \qquad Dh = 0.1028m$

Throat Geometrical Dimensions:

$r := 20.9mm$

$Areathroat := \pi \cdot r^2 \qquad Areathroat = 1.372 \times 10^{-3}\, m^2$

Exit Geometrical Dimensions:

$r := 52.725mm$

$Areaexit := \pi \cdot r^2 \qquad Areaexit = 8.733 \times 10^{-3}\, m^2$

Figure D-1 Specification of inlet and exit geometrical dimensions

Mass Flow Rate Calculation:

$Mthroat := 1$ $\quad Mexit := 3.43$ from Isentropic Flow tables using Area Ratio

$Minlet := 0.1$ from Isentropic Flow tables using Area Ratio

$$mdot := \frac{Areathroat \cdot P0}{\sqrt{T0}} \cdot \sqrt{\frac{\gamma}{R} \cdot \left(\frac{2}{\gamma + 1}\right)^{\frac{(\gamma+1)}{(\gamma-1)}}} \qquad mdot = 2.19106 \frac{kg}{s}$$

Exit Boundary Conditions:

$$Pexit := \frac{P0}{\left[1 + \frac{(\gamma - 1)}{2} \cdot Mexit^2\right]^{\left(\frac{\gamma}{\gamma-1}\right)}} \qquad Pexit = 1.014 \times 10^4 \, Pa$$

$$Texit := \frac{T0}{\left[1 + \frac{(\gamma - 1)}{2} \cdot Mexit^2\right]} \qquad Texit = 93.648 \, K$$

$$\rho exit := \frac{Pexit}{R \cdot Texit} \qquad \rho exit = 0.377 \frac{kg}{m^3} \qquad aexit := \sqrt{\gamma \cdot R \cdot Texit} \qquad aexit = 193.979 \frac{m}{s}$$

$$Uexit := Mexit \cdot aexit \qquad Uexit = 665.347 \frac{m}{s}$$

$$\mu exit := c1 \cdot \left(1 + \frac{c2}{Texit}\right)^{-1} \cdot \sqrt{Texit} \qquad \mu exit = 6.434 \times 10^{-6} \frac{kg}{m\,s}$$

$$\nu exit := \frac{\mu exit}{\rho exit} \qquad \nu exit = 1.705 \times 10^{-5} \frac{m^2}{s}$$

$$mdotexit := \rho exit \cdot Areaexit \cdot Uexit \qquad mdotexit = 2.193 \frac{kg}{s}$$

check point

Figure D-2 Calculation of exit boundary conditions

Inlet Boundary Conditions:

$$Pinlet := \frac{P0}{\left[1 + \frac{(\gamma - 1)}{2}\cdot Minlet^2\right]^{\left(\frac{\gamma}{\gamma-1}\right)}} \qquad Pinlet = 6.951 \times 10^5\,Pa$$

$$Tinlet := \frac{T0}{\left[1 + \frac{(\gamma - 1)}{2}\cdot Minlet^2\right]} \qquad Tinlet = 313.373\,K$$

$$ainlet := \sqrt{\gamma\cdot R\cdot Tinlet} \qquad ainlet = 354.843\,\frac{m}{s} \qquad Uinlet := Minlet\cdot ainlet$$

$$Uinlet = 35.484\,\frac{m}{s}$$

$$\rho inlet := \frac{Pinlet}{R\cdot Tinlet} \qquad \rho inlet = 7.729\,\frac{kg}{m^3}$$

$$\mu inlet := c1\cdot\left(1 + \frac{c2}{Tinlet}\right)^{-1}\cdot\sqrt{Tinlet} \qquad \mu inlet = 1.904 \times 10^{-5}\,\frac{kg}{m\,s}$$

$$\nu inlet := \frac{\mu inlet}{\rho inlet} \qquad \nu inlet = 2.464 \times 10^{-6}\,\frac{m^2}{s}$$

$$mdotinlet := \rho inlet\cdot Areainlet\cdot Uinlet \qquad mdotinlet = 2.276\,\frac{kg}{s}$$

check point

System Capacity:

$$qsystem := \frac{1}{3}\,\frac{m^3}{s} \qquad Uinletsystem := \frac{qsystem}{Areainlet} \qquad Uinletsystem = 40.161\frac{m}{s}$$

$$mdotsystem := \rho inlet\cdot qsystem \qquad mdotsystem = 2.576\frac{kg}{s}$$

The system can supply necessary conditions for this nozzle to be choked

Figure D-3 Calculation of inlet boundary conditions with validation of choking condition checked with the capacity of air supply

Inlet Turbulence Conditions:

$TI := 0.05 \qquad lengthscale := 0.07 \cdot Dh \qquad lengthscale = 7.196\times 10^{-3}\,m \qquad C\mu := 0.09$

$k := \frac{3}{2}\cdot(0.05\cdot Uinlet)^2 \qquad k = 4.722Sv$

$\varepsilon := C\mu^{\frac{3}{4}}\cdot\frac{k^{\frac{3}{2}}}{lengthscale} \qquad \varepsilon = 234.286\frac{m^2}{s^3} \qquad \omega := \frac{k^{\frac{1}{2}}}{C\mu^{\frac{1}{4}}\cdot lengthscale} \qquad \omega = 551.315Hz$

$\nu eddy := \sqrt{\frac{3}{2}}\cdot Uinlet\cdot TI\cdot lengthscale \qquad \nu eddy = 0.016\frac{m^2}{s}$

$Reh := \frac{Uinlet\cdot Dh}{\nu inlet} \qquad Reh = 1.481\times 10^6$

Figure D-4 Calculation of inlet turbulence boundary conditions

In terms of injection; it is sonic but now with different reservoir conditions from the inlet as in chapter three, compatible to bleed type SITVC configuration (total pressure of the injectant is smaller or at maximum equal to the total pressure of the reservoir) and again it is normal to the nozzle wall through a single orifice located at various locations from the nozzle throat (1.5, 2.5 and 3.5 throat diameters from nozzle throat). Both fluids are air and the orifice size has been estimated as 5mm using one dimensional isentropic flow equations to supply injection mass flow rate 2.8% to 5.7% of the main mass flow rate as shown in Fig. D-5.

Injection Boundary Conditions:

$P0 := 7\times 10^{5}\,Pa \qquad T0 := 314K \qquad \gamma := 1.4 \qquad R := 287\frac{J}{kg\cdot K}$

$Minject := 1 \qquad P0inject := (0.5\ \ 0.68\ \ 0.84\ \ 1)\cdot P0 \qquad mdot := 2.19106\frac{kg}{s}$

$$Pinject := \frac{P0inject}{\left[1+\frac{(\gamma-1)}{2}\cdot Minject^{2}\right]^{\left(\frac{\gamma}{\gamma-1}\right)}} \qquad P0inject = \left(3.5\times 10^{5}\ \ 4.76\times 10^{5}\ \ 5.88\times 10^{5}\ \ 7\times 10^{5}\right)Pa$$

$$Pinject = \left(1.849\times 10^{5}\ \ 2.515\times 10^{5}\ \ 3.106\times 10^{5}\ \ 3.698\times 10^{5}\right)Pa$$

$$Tinject := \frac{T0}{\left[1+\frac{(\gamma-1)}{2}\cdot Minject^{2}\right]} \qquad Tinject = 261.667K$$

$r := 5.mm \qquad Areainject := \pi\cdot r^{2} \qquad Areainject = 7.854\times 10^{-5}\,m^{2}$

$$mdotinject := \frac{Areainject\cdot P0inject}{\sqrt{T0}}\cdot\sqrt{\frac{\gamma}{R}\cdot\left(\frac{2}{\gamma+1}\right)^{\frac{(\gamma+1)}{(\gamma-1)}}}$$

$$mdotinject = (0.0627\ \ 0.08527\ \ 0.10534\ \ 0.1254)\frac{kg}{s}$$

$$\frac{mdotinject}{mdot}\cdot 100 = (2.862\ \ 3.892\ \ 4.808\ \ 5.723)$$

Figure D-5 Calculation of injection boundary conditions together with orifice size estimation

After the injection conditions with injection orifice diameter are found out, the choking condition of the converging nozzle at the injection port is checked by comparing the lowest total pressure (hence the lowest static pressure case) at the injection port with the local pressures at different injection locations calculated again using one dimensional isentropic flow equations (see Fig. D-6). The most upstream injection location is the most critical one, since the expansion of the gases is less and at this location the injection pressure is about 2.29 times the local pressure. Thus the injection converging nozzle is choked.

Choking Validation

$\text{Areathroat} := \pi\cdot(20.9\text{mm})^2$ $\quad$ $\text{Pinject} = \left(1.849\times 10^5 \;\; 2.515\times 10^5 \;\; 3.106\times 10^5 \;\; 3.698\times 10^5\right)\text{Pa}$

Station x/Dt=1.5 Geometrical Dimensions:

$r := 28.271\text{mm}$

$\text{Areaexit} := \pi\cdot r^2$ $\quad$ $\text{Areaexit} = 2.511\times 10^{-3}\,\text{m}^2$

$AR := \dfrac{\text{Areaexit}}{\text{Areathroat}}$ $\quad$ $AR = 1.83$ $\quad$ $\text{Mach} := 2.1$ $\quad$ $\text{pratio} := \dfrac{1}{9.145}$

$\text{backp} := \text{P0}\cdot\text{pratio}$ $\quad$ $\text{backp} = 7.654\times 10^4\,\text{Pa}$

Station x/Dt=2.5 Geometrical Dimensions:

$r := 34.519\text{mm}$

$\text{Areaexit} := \pi\cdot r^2$ $\quad$ $\text{Areaexit} = 3.743\times 10^{-3}\,\text{m}^2$

$AR := \dfrac{\text{Areaexit}}{\text{Areathroat}}$ $\quad$ $AR = 2.728$ $\quad$ $\text{Mach} := 2.55$ $\quad$ $\text{pratio} := \dfrac{1}{18.47}$

$\text{backp} := \text{P0}\cdot\text{pratio}$ $\quad$ $\text{backp} = 3.79\times 10^4\,\text{Pa}$

Station x/Dt=3.5 Geometrical Dimensions:

$r := 40.766\text{mm}$

$\text{Areaexit} := \pi\cdot r^2$ $\quad$ $\text{Areaexit} = 5.221\times 10^{-3}\,\text{m}^2$

$AR := \dfrac{\text{Areaexit}}{\text{Areathroat}}$ $\quad$ $AR = 3.805$ $\quad$ $\text{Mach} := 2.9$ $\quad$ $\text{pratio} := \dfrac{1}{31.59}$

$\text{backp} := \text{P0}\cdot\text{pratio}$

$\text{backp} = 2.216\times 10^4\,\text{Pa}$

Figure D-6 Choking validation of the injection nozzle

APPENDIX E

EXPERIMENTAL (COLD FLOW) STUDY OF SITVC

The experimental setup for cold flow tests that are planned to realize is as follows in Fig. E-1. The detailed description of each piece of equipment is mentioned below then designated in Table E-1 showing the quantity of each equipment needed, properties of them and accompanied by sources of provision together with estimated prices. Lastly the preliminary results of this cold flow study are plotted in a graph.

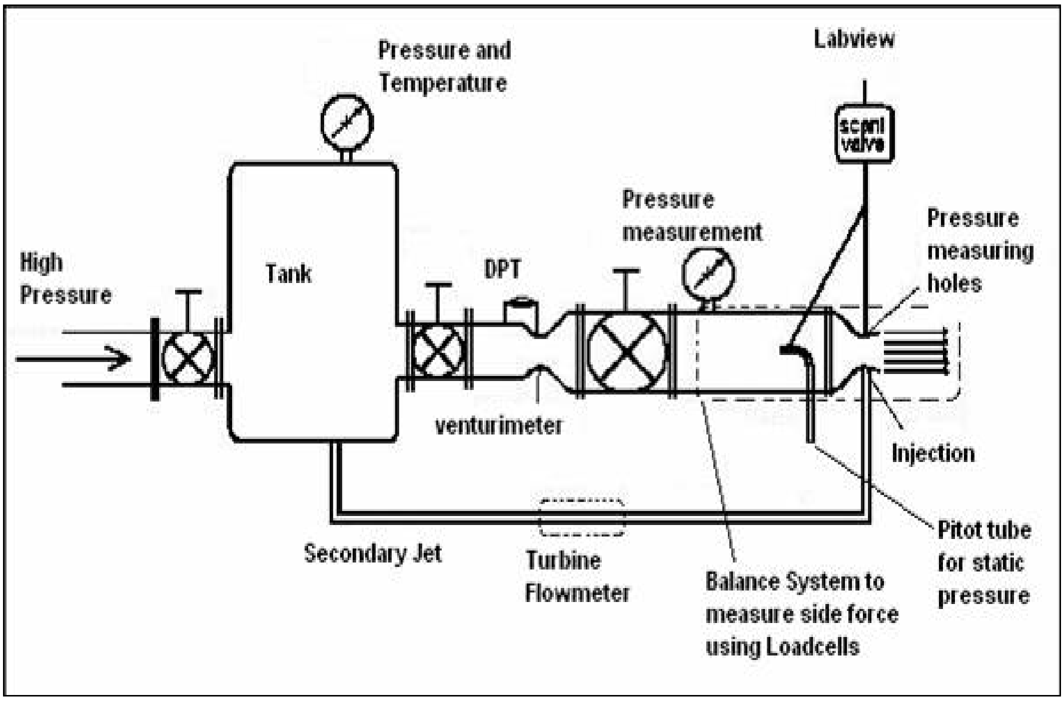

Figure E-1 Experimental setup

Necessary Equipments:

- Compressor

The in-house compressor system is going to be used to test the SITVC system embedded in the nozzle test setup. The nozzle would be operating in overexpansion regime within the capacity of the compressor. Steady pressure values should be obtained downstream of the compressor for the meaningful testing, which will be checked by Bourdon gages.

- Pressure Tank

Stores and supplies necessary air flow for the operation of the SITVC test setup, for the minimum pressure loss the tank should be as close to the compressor as possible.

- Connecting Pipes and System

The high pressure line between the compressor and the test setup should be equipped with pipes of diameters of 6 inches. Appropriate elbows and valves should be utilized for minimum pressure loss. However, the eventual length and diameter of the piping together the final positions and number of the valves would be determined according to the location of test setup.

- Scanivalve System

Its patent belongs to Scanivalve Corporation Company, and with the help of this system, real time pressure measurements along the nozzle divergent cone through the holes that are drilled on the surface, can be accomplished with only a single pressure transducer. Obviously there exists a need for data acquisition system for the acquiring the Scanivalve data. Selenoid valves enable to read pressure data from each hole at a time at steady state.

- Venturimeter

Main mass flow rate would be measured with venturimeter, the design and the production of the venturimeter would be done by in accordance with BS 1042 standard.

- Differential Pressure Transmitter (DPT)

Main mass flow rate would be measured with DPT.

- Turbine Flowmeter

Secondary mass flow rate would be measured with turbine flowmeter.

- Balance System

The design and the production of the balance system would be achieved by in house capabilities. Side forces together with axial thrust forces would be measured with the help of transducers or load cells that located accordingly on the main axis of this system. The figure below, Fig. E-2, shows a generic balance system for the basis.

- Thermocouples

It will be utilized for temperature measurements both inside and outside contours of the nozzle.

- Manometer

It is going to measure the tank pressure.

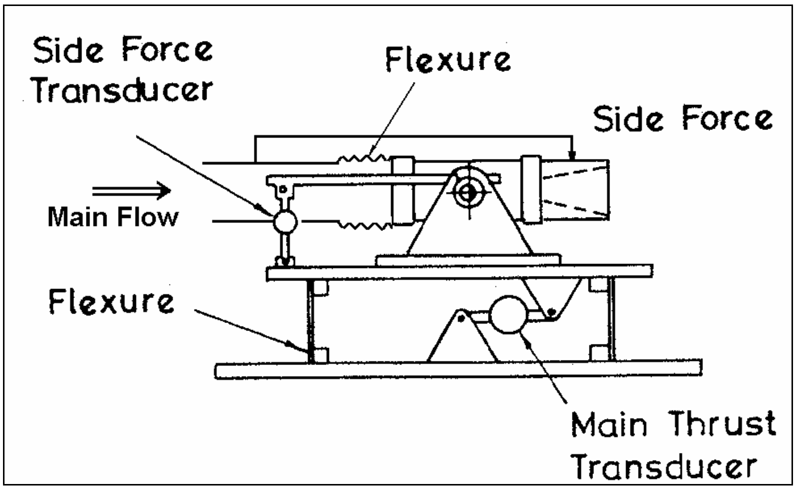

Figure E-2 Side force balance system

- Test Building

For the safety of the measurements and the evaluation of the results there is a need for a small “condo” type building. For the safety it should be away from the compressor on the other hand for the minimization of the pressure losses it should be closer to test setup and the data acquisition system. Scanivalve and the data acquisition system will stay inside the test building.

- Data Acquisition System

For real time pressure and temperature measurements the in-house Labview system is going to be used.

And Pitot probes are going to supply static pressure data.

Table E-1 Equipment list (cont. on next page)

Name	Quantity	Property	Sources	Estimated Price
Connection and piping	In need		National	1,000 $
Venturimetre	1	BS 1042 standard compatible	National	500 $
Differential Pressure Transmitter	1	0-17"/0-100" H_2O PX771-100WDI	Abroad	790 $
Pressure Measurement System (materials and piping)	1	Pressure transducers, Pitot probe	National	500 $
Nozzle model	In need	Various geometries	National	1,000 $
Pressure Transducer	1	1-10 bar	National	1,500 $
Selenoid valves	16	1-10 bar	National	1,000 $
Turbine Flowmeter and Signal Conditioner	1	FTB-931, FLSC-61	Abroad	1,000 $
Bourdon Gage	3	10 bar	National	300 $
Manifold	2	10 channels	National	150 $

Flexible pipe (reinforced PVC tubing)	100ft	10 bar, ¼″	National	50 $
Pressure Regulator with a dial	2	10 bar, ¼″	National	100 $

For the preliminary results, a measurement is taken with ½ scale of rocket nozzle, specified in Chapter 4 for no-injection case, connected directly to compressor, and static pressure data has been acquired using Scanivalve coupled with a single pressure transducer enabling to read one pressure value at a time from four holes drilled on nozzle surface. Once the tube from a specific line is opened, the other lines are closed and then the system reaches to steady state, afterwards a pressure value is taken from that line. Then the procedure is repeated for other holes, which are positioned 4, 6, 8, 10 mm away from the exit plane respectively. The measurement conditions are depicted on Table E-2. Since there is a pressure transducer used in measurements, all pressure values are relative (Gage).

Table E-2 Measurement conditions and results

Static Inlet Prsssure (bar-Gage)	Ambient Pressure (mbar)	1st station (10mm from exit) bar	2nd station (10mm from exit) bar	3rd station (10mm from exit) bar	4th station (10mm from exit) bar
5.886	**895.970**	**1.237**	**1.133**	**1.032**	**0.876**

In terms of numerical simulations a two–dimensional axissymmetric case corresponding to this geometry is solved using FLUENT® without injection. The results are compared to measured values. The results show discrepancies in pressure values, the main sources of discrepancies are the experimental uncertainties and bias. Obviously there are uncertainties involved in measurements at each unit of equipments. However the overall uncertainty assessment is not accomplished. In addition there are also errors involved in numerical simulations, mentioned in Chapter 3 results.

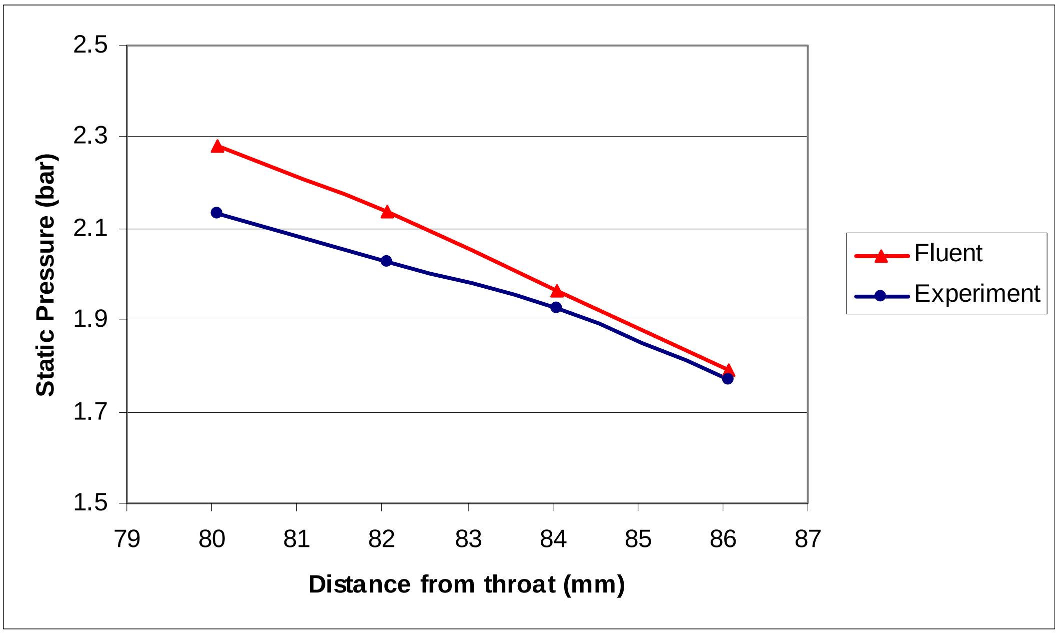

Figure E-3 Comparison of measured pressure data with FLUENT®